Dark Energy Survey: A 2.1% measurement of the angular baryonic acoustic oscillation scale at redshift $z_{\text{eff}} = 0.85$ from the final dataset

T. M. C. Abbott,[1] M. Adamow,[2] M. Aguena,[3] S. Allam,[4] O. Alves,[5] A. Amon,[6,7,8] F. Andrade-Oliveira,[5] J. Asorey,[9] S. Avila,[10] D. Bacon,[11] K. Bechtol,[12] G. M. Bernstein,[13] E. Bertin,[14,15] J. Blazek,[16] S. Bocquet,[17] D. Brooks,[18] D. L. Burke,[19,20] H. Camacho,[21,3,22] A. Carnero Rosell,[23,3,24] D. Carollo,[25] A. Carr,[24] J. Carretero,[10] F. J. Castander,[26,27] R. Cawthon,[28] K. C. Chan,[29,30] C. Chang,[31,32] C. Conselice,[33,34] M. Costanzi,[35,25,36] M. Crocce,[26,27] L. N. da Costa,[3] M. E. S. Pereira,[37] T. M. Davis,[38] J. De Vicente,[39] N. Deiosso,[39] S. Desai,[40] H. T. Diehl,[4] S. Dodelson,[41,42] C. Doux,[13,43] A. Drlica-Wagner,[31,4,32] J. Elvin-Poole,[44] S. Everett,[45] I. Ferrero,[46] A. Ferté,[20] B. Flaugher,[4] P. Fosalba,[26,27] J. Frieman,[4,32] J. García-Bellido,[47] E. Gaztanaga,[26,11,27] G. Giannini,[10,32] K. Glazebrook,[45] R. A. Gruendl,[2,48] G. Gutierrez,[4] W. G. Hartley,[49] S. R. Hinton,[38] D. L. Hollowood,[50] K. Honscheid,[51,52] D. Huterer,[5] D. J. James,[53] S. Kent,[4,32] K. Kuehn,[54,55] O. Lahav,[18] S. Lee,[45] G. F. Lewis,[54] C. Lidman,[56,57] M. Lima,[57,3] H. Lin,[4] U. Malik,[58] C. Maraston,[9] J. L. Marshall,[58] P. Martini,[51,59] J. Mena-Fernández,[39,60] F. Menanteau,[2,48] R. Miquel,[61,10] J. J. Mohr,[62,17] J. Myles,[8] A. Möller,[45] R. C. Nichol,[63] R. L. C. Ogando,[64] A. Palmese,[41] W. J. Percival,[44,65] A. Pieres,[3,64] A. A. Plazas Malagón,[19,20] A. Porredon,[66] J. Prat,[31,67] M. Rodríguez-Monroy,[68,47] A. K. Romer,[69] A. Roodman,[19,20] R. Rosenfeld,[70,3] A. J. Ross,[51] E. S. Rykoff,[19,20] M. Sako,[13] S. Samuroff,[16] C. Sánchez,[13] E. Sanchez,[39] D. Sanchez Cid,[39] B. Santiago,[71,3] M. Schubnell,[5] I. Sevilla-Noarbe,[39] E. Sheldon,[22] M. Smith,[72] E. Suchyta,[73] M. E. C. Swanson,[2] G. Tarle,[5] D. Thomas,[11] C. To,[51] L. Toribio San Cipriano,[39] M. A. Troxel,[74] B. E. Tucker,[57] D. L. Tucker,[4] A. R. Walker,[1] N. Weaverdyck,[5,75] J. Weller,[62,76] P. Wiseman,[72] and B. Yanny[4]

(DES Collaboration)[*]

[1]*Cerro Tololo Inter-American Observatory, NSF's National Optical-Infrared Astronomy Research Laboratory, Casilla 603, La Serena, Chile*
[2]*Center for Astrophysical Surveys, National Center for Supercomputing Applications, 1205 West Clark Street, Urbana, Illinois 61801, USA*
[3]*Laboratório Interinstitucional de e-Astronomia—LIneA, Rua Gal. José Cristino 77, Rio de Janeiro, Rio de Janeiro-20921-400, Brazil*
[4]*Fermi National Accelerator Laboratory, P. O. Box 500, Batavia, Illinois 60510, USA*
[5]*Department of Physics, University of Michigan, Ann Arbor, Michigan 48109, USA*
[6]*Institute of Astronomy, University of Cambridge, Madingley Road, Cambridge CB3 0HA, United Kingdom*
[7]*Kavli Institute for Cosmology, University of Cambridge, Madingley Road, Cambridge CB3 0HA, United Kingdom*
[8]*Department of Astrophysical Sciences, Princeton University, Peyton Hall, Princeton, New Jersey 08544, USA*
[9]*Departamento de Física Teórica and Instituto de Física de Partículas y del Cosmos (IPARCOS-UCM), Universidad Complutense de Madrid, 28040 Madrid, Spain*
[10]*Institut de Física d'Altes Energies (IFAE), The Barcelona Institute of Science and Technology, Campus UAB, 08193 Bellaterra (Barcelona), Spain*
[11]*Institute of Cosmology and Gravitation, University of Portsmouth, Portsmouth, PO1 3FX, United Kingdom*
[12]*Physics Department, 2320 Chamberlin Hall, University of Wisconsin-Madison, 1150 University Avenue, Madison, Wisconsin 53706-1390, USA*
[13]*Department of Physics and Astronomy, University of Pennsylvania, Philadelphia, Pennsylvania 19104, USA*
[14]*CNRS, UMR 7095, Institut d'Astrophysique de Paris, F-75014, Paris, France*
[15]*Sorbonne Universités, UPMC Univ Paris 06, UMR 7095, Institut d'Astrophysique de Paris, F-75014, Paris, France*
[16]*Department of Physics, Northeastern University, Boston, Massachusetts 02115, USA*
[17]*University Observatory, Faculty of Physics, Ludwig-Maximilians-Universität, Scheinerstraße 1, 81679 Munich, Germany*
[18]*Department of Physics and Astronomy, University College London, Gower Street, London, WC1E 6BT, United Kingdom*
[19]*Kavli Institute for Particle Astrophysics and Cosmology, Stanford University, P. O. Box 2450, Stanford, California 94305, USA*

[20]*SLAC National Accelerator Laboratory, Menlo Park, California 94025, USA*

[21]*Instituto de Física Teórica, Universidade Estadual Paulista, São Paulo, Brazil*

[22]*Brookhaven National Laboratory, Building 510, Upton, New York 11973, USA*

[23]*Instituto de Astrofisica de Canarias, E-38205 La Laguna, Tenerife, Spain*

[24]*Universidad de La Laguna, Departamento de Astrofísica, E-38206 La Laguna, Tenerife, Spain*

[25]*INAF-Osservatorio Astronomico di Trieste, via G. B. Tiepolo 11, I-34143 Trieste, Italy*

[26]*Institut d'Estudis Espacials de Catalunya (IEEC), 08034 Barcelona, Spain*

[27]*Institute of Space Sciences (ICE, CSIC),
Campus UAB, Carrer de Can Magrans, s/n, 08193 Barcelona, Spain*

[28]*Physics Department, William Jewell College, Liberty, Missouri, 64068, USA*

[29]*School of Physics and Astronomy, Sun Yat-sen University,
2 Daxue Road, Tangjia, Zhuhai 519082, China*

[30]*CSST Science Center for the Guangdong-Hongkong-Macau Greater Bay Area,
SYSU, Zhuhai 519082, China*

[31]*Department of Astronomy and Astrophysics, University of Chicago, Chicago, Illinois 60637, USA*

[32]*Kavli Institute for Cosmological Physics, University of Chicago, Chicago, Illinois 60637, USA*

[33]*Jodrell Bank Center for Astrophysics, School of Physics and Astronomy,
University of Manchester, Oxford Road, Manchester, M13 9PL, United Kingdom*

[34]*University of Nottingham, School of Physics and Astronomy, Nottingham NG7 2RD, United Kingdom*

[35]*Astronomy Unit, Department of Physics, University of Trieste, via Tiepolo 11, I-34131 Trieste, Italy*

[36]*Institute for Fundamental Physics of the Universe, Via Beirut 2, 34014 Trieste, Italy*

[37]*Hamburger Sternwarte, Universität Hamburg, Gojenbergsweg 112, 21029 Hamburg, Germany*

[38]*School of Mathematics and Physics, University of Queensland, Brisbane, QLD 4072, Australia*

[39]*Centro de Investigaciones Energéticas, Medioambientales y Tecnológicas (CIEMAT), Madrid, Spain*

[40]*Department of Physics, IIT Hyderabad, Kandi, Telangana 502285, India*

[41]*Department of Physics, Carnegie Mellon University, Pittsburgh, Pennsylvania 15312, USA*

[42]*NSF AI Planning Institute for Physics of the Future, Carnegie Mellon University,
Pittsburgh, Pennsylvania 15213, USA*

[43]*Université Grenoble Alpes, CNRS, LPSC-IN2P3, 38000 Grenoble, France*

[44]*Department of Physics and Astronomy, University of Waterloo,
200 University Avenue West, Waterloo, Ontario N2L 3G1, Canada*

[45]*Jet Propulsion Laboratory, California Institute of Technology,
4800 Oak Grove Dr., Pasadena, California 91109, USA*

[46]*Institute of Theoretical Astrophysics, University of Oslo,
P.O. Box 1029 Blindern, NO-0315 Oslo, Norway*

[47]*Instituto de Fisica Teorica UAM/CSIC, Universidad Autonoma de Madrid, 28049 Madrid, Spain*

[48]*Department of Astronomy, University of Illinois at Urbana-Champaign,
1002 West Green Street, Urbana, Illinois 61801, USA*

[49]*Department of Astronomy, University of Geneva, ch. d'Écogia 16, CH-1290 Versoix, Switzerland*

[50]*Santa Cruz Institute for Particle Physics, Santa Cruz, California 95064, USA*

[51]*Center for Cosmology and Astro-Particle Physics, The Ohio State University,
Columbus, Ohio 43210, USA*

[52]*Department of Physics, The Ohio State University, Columbus, Ohio 43210, USA*

[53]*Center for Astrophysics | Harvard & Smithsonian,
60 Garden Street, Cambridge, Massachusetts 02138, USA*

[54]*Australian Astronomical Optics, Macquarie University, North Ryde, NSW 2113, Australia*

[55]*Lowell Observatory, 1400 Mars Hill Road, Flagstaff, Arizona 86001, USA*

[56]*Centre for Gravitational Astrophysics, College of Science,
The Australian National University, Acton, ACT 2601, Australia*

[57]*The Research School of Astronomy and Astrophysics, Australian National University,
Acton, ACT 2601, Australia*

[58]*George P. and Cynthia Woods Mitchell Institute for Fundamental Physics and Astronomy,
and Department of Physics and Astronomy, Texas A&M University,
College Station, Texas 77843, USA*

[59]*Department of Astronomy, The Ohio State University, Columbus, Ohio 43210, USA*

[60]*LPSC Grenoble—53, Avenue des Martyrs 38026, Grenoble, France*

[61]*Institució Catalana de Recerca i Estudis Avançats, E-08010 Barcelona, Spain*

[62]*Max Planck Institute for Extraterrestrial Physics, Giessenbachstrasse, 85748 Garching, Germany*

[63]*School of Maths and Physics, University of Surrey, Guildford, United Kingdom*

[64]*Observatório Nacional, Rua Gal. José Cristino 77, Rio de Janeiro, RJ-20921-400, Brazil*

[65]*Perimeter Institute for Theoretical Physics,
31 Caroline Street North, Waterloo, Ontario N2L 2Y5, Canada*
[66]*Ruhr University Bochum, Faculty of Physics and Astronomy, Astronomical Institute,
German Centre for Cosmological Lensing, 44780 Bochum, Germany*
[67]*Nordita, KTH Royal Institute of Technology and Stockholm University,
Hannes Alfvéns väg 12, SE-10691 Stockholm, Sweden*
[68]*Laboratoire de physique des 2 infinis Irène Joliot-Curie, CNRS Université Paris-Saclay,
Bât. 100, F-91405 Orsay Cedex, France*
[69]*Department of Physics and Astronomy, Pevensey Building, University of Sussex,
Brighton, BN1 9QH, United Kingdom*
[70]*ICTP South American Institute for Fundamental Research Instituto de Física Teórica,
Universidade Estadual Paulista, São Paulo, Brazil*
[71]*Instituto de Física, UFRGS, Caixa Postal 15051, Porto Alegre, Rio Grande do Sul—91501-970, Brazil*
[72]*School of Physics and Astronomy, University of Southampton, Southampton, SO17 1BJ, United Kingdom*
[73]*Computer Science and Mathematics Division, Oak Ridge National Laboratory,
Oak Ridge, Tennessee 37831, USA*
[74]*Department of Physics, Duke University, Durham, North Carolina 27708, USA*
[75]*Lawrence Berkeley National Laboratory, 1 Cyclotron Road, Berkeley, California 94720, USA*
[76]*Universitäts-Sternwarte, Fakultät für Physik, Ludwig-Maximilians Universität München,
Scheinerstraße 1, 81679 München, Germany*

We present the angular diameter distance measurement obtained with the baryonic acoustic oscillation (BAO) feature from galaxy clustering in the completed Dark Energy Survey, consisting of six years (Y6) of observations. We use the Y6 BAO galaxy sample, optimized for BAO science in the redshift range $0.6 < z < 1.2$, with an effective redshift at $z_{eff} = 0.85$ and split into six tomographic bins. The sample has nearly 16 million galaxies over 4,273 square degrees. Our consensus measurement constrains the ratio of the angular distance to sound horizon scale to $D_M(z_{eff})/r_d = 19.51 \pm 0.41$ (at 68.3% confidence interval), resulting from comparing the BAO position in our data to that predicted by PLANCK ΛCDM via the BAO shift parameter $\alpha = (D_M/r_d)/(D_M/r_d)_{PLANCK}$. To achieve this, the BAO shift is measured with three different methods, angular correlation function (ACF), angular power spectrum (APS), and projected correlation function (PCF), obtaining $\alpha = 0.952 \pm 0.023$, 0.962 ± 0.022, and 0.955 ± 0.020, respectively, which we combine to $\alpha = 0.957 \pm 0.020$, including systematic errors. When compared with the ΛCDM model that best fits PLANCK data, this measurement is found to be 4.3% and 2.1σ below the angular BAO scale predicted. To date, it represents the most precise angular BAO measurement at $z > 0.75$ from any survey and the most precise measurement at any redshift from photometric surveys. The analysis was performed blinded to the BAO position, and it is shown to be robust against analysis choices, data removal, redshift calibrations, and observational systematics.

I. INTRODUCTION

The Dark Energy Survey[1] (DES) is a stage-III photometric galaxy survey designed to constrain the properties of dark energy and other cosmological parameters from multiple probes [1–4]. DES has performed state-of-the-art analyses of weak gravitational lensing (WL) by measuring and correlating the shape of more than 100 million galaxies [5–7]. DES has also excelled in using galaxy clustering (GC) as a cosmological probe, either on its own or in combination with WL and other probes [8–11]. These probes (WL, GC) have also been combined with galaxy cluster counts detected on DES [12,13] and with external CMB data [14,15]. The DES Supernova program has also broken new grounds in constraining cosmology from ∼1500 type Ia supernovae [16,17]. In addition to that, the large dataset and catalogs produced by the Dark Energy Survey represent a unique source for other cosmological and astronomical analyses [18–22].

The measurement of galaxy clustering within DES has traditionally been split into two main probes. On the one hand, we have the GC of the so-called *lens* samples that have been used mainly in combination with WL and other probes to constrain the amplitude of mass fluctuations σ_8, the matter density Ω_m, and other ΛCDM parameters as well

---

[*]des-publication-queries@fnal.gov
[1]https://www.darkenergysurvey.org/.

as extensions of ΛCDM, such as the equation of state of dark energy, w. On the other hand, we have the measurement of the position of the baryonic acoustic oscillation (BAO) peak in the clustering of galaxies from a different sample of galaxies, optimized for this science case. The BAO peak position can be used as a standard ruler to constrain the angular diameter distance to redshift relation and, in turn, constrain the expansion history of the Universe. In this work, we present the measurement of the BAO peak position from the final DES dataset, which includes six years (2013–2019) of observations. For the remainder, this dataset will be referred to as Year 6 or Y6.

The baryonic acoustic oscillation (BAO) feature originated in early times when the Universe was in the form of a plasma in which photons and the baryonic matter were in continuous interaction. Thanks to this interaction, sound waves propagate in this plasma up to the drag epoch, when photons and the baryonic matter cease to interact. This leaves a preferred scale in the distribution of matter in the Universe, corresponding approximately to the sound horizon at decoupling, denoted by r_d. This scale can be measured as an excess of signal (a *peak*) in the two-point correlation function in different tracers of the matter distribution. The scale of this peak, r_d, remains fixed in comoving coordinates after recombination and, thus, can be used as a standard ruler to constrain the relation between redshift and the comoving angular diameter distance $[D_M(z)]$ [23–26].[2] This relation can be used to constrain the expansion history of the Universe and, hence, the nature of dark energy. Remarkably, the redshift range explored here corresponds to an epoch when the Universe expansion was about to transition from deceleration to acceleration, according to the standard model, hence being an excellent test for dark energy near this transition.

This acoustic peak was first seen in the CMB anisotropies with BOOMERanG and MAXIMA experiments at the turn of the century [27,28]. Half a decade later, the BAO peak was first measured in the distribution of galaxies by both the Sloan Digital Sky Survey (SDSS) [29] and the two-degree Field Galaxy Redshift Survey (2dFGRS) [30,31]. Since then, a series of galaxy spectroscopic surveys have been designed to measure BAO at different redshifts. In particular, it is worth highlighting the six-degree Field Galaxy Survey (6dFGS) [32], the WiggleZ dark energy survey [33–36], and the [extended] Baryonic Oscillations Spectroscopic Survey ([e]BOSS), part of the SDSS series [37–46]. The last release by eBOSS/SDSS [46], represents the state-of-the-art in spectroscopic measurements of BAO and the closure of stage-III spectroscopic surveys. A new generation

of spectroscopic surveys (stage-IV), with the Dark Energy Spectroscopic Instrument [47] and the European Space Agency mission Euclid [48] as the prime examples, recently started collecting data and have among their main design goals to measure the BAO peak with higher precision and at higher redshifts.

In this context, the Dark Energy Survey, as a photometric survey designed simultaneously for multiple cosmological probes, cannot measure the redshift of galaxies with high precision. Instead, we use the photometric redshift, z_{ph}, based on the fluxes measured in five bands. This makes the measurement of distances between galaxies more challenging, losing part of the information and degrading the signal-to-noise ratio of the BAO signal. On the other hand, DES is able to detect a large number of galaxies and have a photometric redshift estimate for all of them (of the order of 100s of millions vs 2 million spectra measured by SDSS in 20 years). Among those galaxies, we can select a subsample for which the redshift can be estimated at a ∼3% precision, giving us the opportunity to detect the angular component of the BAO with a precision competitive with stage-III spectroscopic surveys.

In order to achieve competitive BAO measurements, the Dark Energy Survey collaboration has dedicated remarkable efforts in all the successive data batches (Year 1 or Y1, Year 3 or Y3, and now Y6) to this key analysis in parallel to other galaxy clustering projects. On the galaxy sample selection side, this work builds on the selection optimized in [49] that we now reoptimized in our companion paper [50]. This selection is remarkably different from the ones applied to spectroscopic surveys [51,52], resulting in a much larger number of galaxies (16 million in Y6 DES BAO vs < 1 million in BOSS/eBOSS individual samples). The validation of these galaxy samples and the techniques for the correction of systematics build on [8,53–55], which, in turn, build on previous works [56–59]. In parallel, a large part of the tests performed to validate our analysis relies on having the order of 2000 simulations, with the techniques developed in [60–63], similar to what it is standard in spectroscopic surveys [64,65], but with the challenges of having a much larger number of galaxies and including the modeling of redshift errors. The techniques to obtain robust BAO measurements from the angular correlation function (ACF) and angular power spectrum (APS) were developed in [66,67], respectively. Combining/comparing analyses from configuration and Fourier space is also a common practice in spectroscopic BAO analyses [e.g., [68–71]]. Here, we add a third way to analyze the data based on the projected correlation function (PCF), which builds upon the techniques developed in [72–74].

All of the previous work led to a 4% measurement of the angular diameter distance of the BAO peak in DES Y1 [75] (at $z_{eff} \sim 0.81$) and a 2.7% in DES Y3 (at $z_{eff} \sim 0.83$) [76]. The latter measurement already represented the tightest constraint from a photometric survey and the tightest

---

[2]Technically, angular BAO constraints are only sensitive to the ratio $D_M(z)/r_d$, but since we can determine r_d with great accuracy from CMB constraints and well-understood physics, in practice, the information we recover from late time BAO can be interpreted in terms of constraining the angular diameter distance, $D_M(z)$.

constraint from any survey at an effective redshift $0.8 < z_{eff} < 1.4$. Another photometric BAO measurement at similar redshift is given by [77], with a 6.5% precision at $z_{eff} = 0.85$, and other BAO photometric measurements include [78–84]. When comparing to spectroscopic angular BAO measurement, at a similar redshift, we find the eBOSS ELG with a ~5% precision at $z_{eff} = 0.85$, weaker constraints that the DES Y3 BAO results. However, more precise angular BAO measurements are reported at higher and lower redshifts by BOSS (1.5% at $z_{eff} = 0.38$, 1.3% at $z_{eff} = 0.51$) and eBOSS (1.9% at $z_{eff} = 0.70$, 2.6% at $z_{eff} = 1.48$ and 2.9% at $z_{eff} = 2.33$) [38,71,85–90]. The 2.1% measurement we report in this paper is currently the tightest angular BAO measurement at an effective redshift larger than $z_{eff} = 0.75$.

In this work, we use the complete DES dataset, Y6, to constrain the angular BAO. We follow a similar methodology to the Year 3 analysis, with three main changes. First, we reoptimize the sample in our companion paper [50] and extend it from $0.6 < z_{ph} < 1.1$ to $0.6 < z_{ph} < 1.2$, giving us an effective redshift of $z_{eff} = 0.851$. Second, we reinforce the redshift validation, considering several independent calibrations and quantifying its possible impact on the BAO measurement. Third, we provide BAO measurements from three types of two-point clustering statistics: angular correlation function, angular power spectrum, and projected correlation function. Our reported consensus result stems from the statistical combination of those three measurements.

Finally, in the scientific community of cosmology, there is a growing awareness of the danger of confirmation biases affecting results in science. In order to mitigate this, many collaborations have built a series of protocols to *blind* the results of the analyses until these are *finalized*, with different criteria imposed on how to blind the data and when they are considered finalized. DES has built a strong policy in this direction, and it is one pillar of the way we perform and present our analysis in this paper. The BAO analysis presented here and in previous DES data batches are likely the ones with the strongest blinding policies to this date.

This paper is organized as follows. In Sec. II, we describe the Y6 DES data and the BAO subsample, together with its mask, observational systematic treatment, and redshift characterisation. In Sec. III, we describe the mock catalogs that are used to validate and optimize our analysis. In Sec. IV, we describe the methodology used to extract the BAO information. In Sec. V, we validate our analysis in three aspects: robustness against redshift distributions (Sec. V A), robustness of the modeling of individual estimators (ACF, APS, and PCF) against the mock catalogs (Sec. V B), and robustness of our combined measurement (Sec. V C). In Sec. VI, we present a battery of tests performed on the data, while blinded, prior to deciding whether it was ready to unblind

and publish. In Sec. VII, we present the unblinded results on the BAO measurement and a series of robustness tests. Finally, we conclude in Sec. VIII.

II. THE DARK ENERGY SURVEY DATA

A. DES Y6 GOLD catalog

The Dark Energy Survey data used in this analysis is obtained from a subset of the wide-area imaging performed by the survey in its five photometric bands, spanning a period of approximately six years from 2013 to 2019, encompassing the entire run of the project (DES Y6). In particular, we use the detections in the coadd catalogs, the details of which are described in [20]. This dataset spans the full 5,000 square degrees of the survey, reaching a depth in the $[grizY]$ bands of $[24.7, 24.4, 23.8, 23.1, 21.7]$ for point sources, at a signal-to-noise ratio of 10.

The coadd catalogs are further enhanced into the Y6 GOLD catalog [22] to include improvements in object photometry, star-galaxy separation, quality flags, additional masking, and the creation of *ad hoc* survey property maps to be used to mitigate clustering systematic effects. This catalog is the basis for the BAO sample, described in the following section. Note that the core Y6 GOLD catalog has the same number of detections as the public DR2 data, but with additional columns and a flag identifying the object as part of the official footprint to be used in the cosmology analyses.

B. The BAO-optimized sample

The Y6 BAO sample is a subsample of the Y6 GOLD catalog described above and is fully described in the companion paper Mena-Fernández and DES [50]. The procedure to build and characterize this sample builds up from those used in the Y1 and Y3 BAO samples, described in [49,55], respectively. The first criterion is to select galaxies above redshift $z \sim 0.6$, where DES BAO measurements can be competitive. For that, in [49], we argued that a red selection as follows would already be a good starting point:

$$1.7 < (i - z) + 2(r - i). \tag{1}$$

Additionally, red galaxies are expected to have better redshift estimates and higher galaxy bias, both improving the expected BAO signal. The Y6 data has an increased depth, resulting in better photometry and redshift estimations than the Y3 and Y1 catalogs. For this reason, we extended our redshift range of study to

$$0.6 < z_{ph} < 1.2, \tag{2}$$

whereas we studied $0.6 < z_{ph} < 1.0$ in Y1 and $0.6 < z_{ph} < 1.1$ in Y3. z_{ph} is the photometric redshift estimate and is

given by the variable DNF_Z of the directional neighboring fitting photo-z code (DNF, [91], more details in Sec. II E). For most of the analysis, we will be splitting this sample into six tomographic bins given by $\Delta z_{\rm ph} = 0.1$ that we will label as bins 1 to 6 in increasing order with redshift.

One of the main challenges in galaxy clustering with photometric samples is the estimation and validation of the redshift distribution $n(z)$. In Y3, an important step of the redshift validation was based on direct calibration with the VIMOS public extragalactic redshift survey (VIPERS) sample [92], which is complete up to

$$i < 22.5. \tag{3}$$

In order to ensure high quality in our validation pipeline, we include this selection in our sample definition. This selection did not need to be imposed in Y3, where the criterion was naturally met by the selection. By selecting bright galaxies, we additionally expect this sample to be less affected by imaging systematics and also to have better estimates of the redshifts and their uncertainties.

This leads us to our fourth main selection criterion: a redshift-dependent magnitude limit in the band i: $i < a + b\, z_{\rm ph}$. We have to choose a balance in our sample selection between having more galaxies or having lower redshift uncertainties. This idea was already implemented in Y1 [49], where a and b were optimized for the BAO distance measurement using a Fisher forecast based on sample properties such as number density and redshift distributions. The same selection was used in Y3 [55], with the a and b values optimized from Y1. In Y6, however, having much deeper photometry, we expected the optimal sample to change. For that reason, in [50], we have reoptimized the sample selection for a and b [after imposing Eqs. (1)–(3)], finding our best BAO forecast for

$$i < 19.64 + 2.894 z_{\rm ph}. \tag{4}$$

All the details of this optimization can be found in [50].

Our Y6 BAO sample definition is given by the selections imposed by Eqs. (1)–(4). Additionally, as part of our quality cuts, we also apply a bright magnitude cut at $17.5 < i$ to remove bright contaminant objects such as binary stars, as done in Y3. Stellar contamination is mitigated with the galaxy and star classifier EXTENDED_CLASS_MASH_SOF from the Y6 GOLD catalog.

The resulting catalog, over the area described below (Sec. II C), comprises a total of 15,937,556 objects, more than twice the Y3 BAO sample. In Y6, we additionally used unWISE infrared photometry [93] to estimate the residual stellar contamination in our sample, finding a stellar fraction of $f_{\rm star} = 0.023$, 0.027, 0.033, 0.023, 0.008, 0.007 for the redshift bins 1 to 6, respectively. The method to estimate this is briefly described in [50] and will be presented in detail in [94].
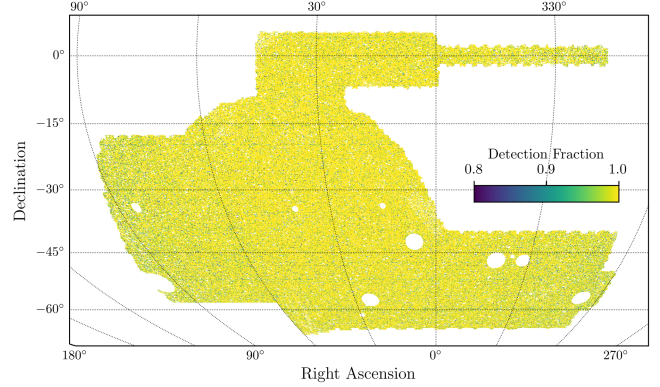

FIG. 1. Angular mask for the DES Y6 BAO analysis. The value plotted for each pixel represents its detection fraction. The total area of the mask, computed weighting by the detection fraction, is $4,273.42$ deg^2.

C. Angular mask

The Y6 BAO sample is distributed over a footprint of 4273.42 deg^2, as shown in Fig. 1, defined at HEALPix resolution of $N_{\rm side} = 4096$ with a pixel area of ~ 0.74 arcmin^2. The final area results from applying several quality cuts: We impose pixels to have been observed at least twice in bands *griz* and to have a detection fraction higher than 0.8. The detection fraction quantifies the fraction of the area of a pixel at resolution 4096 that is not masked by foregrounds, which is studied originally at higher resolution (details in [95]). We also exclude pixels that do not reach the depth of our sample: $i_{\rm lim} = 22.5$ at 10σ. We also veto pixels affected by astrophysical foregrounds such us bright stars, globular clusters or large nearby galaxies (including the large magellanic cloud); see [22]. More details on the masking construction are given in [50].

Finally, we also mask outliers on the maps that trace galactic cirrus and image artifacts, amounting to $\sim 1.85\%$ of the area. Further details are given in the companion paper [50], and a full study of the effect of masking outliers of survey property maps is deferred to [95].

D. LSS systematics weights

Observing conditions as well as (galactic) foregrounds affect the fraction of galaxies that we are be able to detect in our sample. This will result in a detection fraction with a pattern in the observed sky that can lead to spurious galaxy clustering, if unaccounted for. In order to characterize this pattern, we use a series of survey property maps summarizing both the observing conditions and foregrounds.

We mitigate the impact of observational systematics by applying correcting weights to the galaxy sample with the *iterative systematics decontamination* (ISD) method, used in other DES galaxy clustering analyses [8,53–55,94]. This method assumes a linear dependence between the observed galaxy number density and the survey property

contamination template maps. A linear regression between the survey property and the number of galaxies is performed and its χ^2 compared to that of a null correlation. The resulting $\Delta\chi^2$ is compared against 1000 lognormal mock catalogs, taking as reference the percentile 68 of their $\Delta\chi^2$ distribution, $\Delta\chi^2_{68}$. Then, we consider a correlation of a given survey property map significant if $\Delta\chi^2 > T_{1D}\Delta\chi^2_{68}$, where T_{1D} represents a threshold that is a free parameter of the ISD method. In Y3 BAO, we chose $T_{1D} = 4$ (equivalent to a 2σ significance), a milder requirement than that used in the GC + WL analyses: $T_{1D} = 2$. In Y6 BAO, we lie on the more stringent side with a threshold $T_{1D} = 2$. Details on the decontamination methodology, the survey property maps used as contamination templates, and the weight validation can be found in [50].

At the moment of construction of the ICE-COLA mocks described in Sec. III, the ISD weights were not finalized. In order to have a first estimate of the amplitude of clustering to fit the mocks, we used a preliminary version of the weights, based on the modified elastic net approach (ENET), described in [96].

Finally, we remark that the effect of these systematic weights has a relatively more important effect on large scales, requiring a thorough validation for studies such as the combination of GC with WL (the so-called 3 × 2pt analysis), primordial non-Gaussianties, etc. However, this contamination typically has a very smooth pattern in clustering, not affecting the location of the BAO peak. Indeed, at early stages, we checked with lognormal mocks that (an early version of) the weights described here were not having any effect on the recovered BAO (last two entries of Table II). Once the main pre-unblinding tests were passed (Sec. VI), but prior to unblinding, we checked that when the systematic weights are ignored, the BAO position in Y6 moved only by 0.21%, 0.04%, and 0.32% for ACF, APS, and PCF, respectively. This is below 0.2σ for all three estimators. We consider this error as a very upper limit of the possible residual effects from observational systematic and conclude that any remaining uncertainty on the weights should have a negligible impact on the BAO measured position.

E. Photometric redshifts

As explained in Sec. II B, we split our sample in tomographic redshift bins using the redshift estimation DNF_Z from DNF, which we describe below. However, this estimation of redshift has a nontrivial uncertainty associated with it. This implies that the distribution of redshifts estimated from DNF_Z, $n(z_{ph})$, will not correspond to the true underlying distribution, $n(z)$, that will be more spread. In this section, we study different ways to characterize that underlying distribution.

We consider the following methods:
(1) Directional neighborhood fitting (DNF, [91]). This method computes the photometric redshift of each

galaxy by comparing its colors and magnitudes to those of the training sample. For that, DNF uses a nearest neighbor algorithm with a directional metric that accounts simultaneously for magnitude and color. It provides several outputs:
(a) DNF_Z,[3] hereafter z_{ph}, is computed from a regression on magnitude space. The regression is fitted from a set of neighbors from a reference sample of galaxies whose spectroscopic redshifts are known. That is the main estimate provided by the algorithm.
(b) DNF_ZN,[4] hereafter z_{nn}, is the redshift of the nearest neighbor. The z_{nn} stacking provides a good estimation for the redshift distribution $n(z)$ whenever the training sample is complete.
(c) PDF provides the photometric redshift distribution for each galaxy computed from the residuals of the fit.
For the galaxies whose spectrum is in the redshift calibration sample, we do exclude this information in order to compute the summary statistics above (z_{ph}, z_{nn}).
(2) VIPERS spectroscopic direct calibration. The VIPERS spectroscopic sample is complete for $i < 22.5$ and $z > 0.6$ [92]. Since the DES footprint contains all of the area of VIPERS, we can construct a matched catalog in the overlapping area (16.3 deg²) and measure directly the $n(z)$ from a histogram of the spectroscopic redshifts. The limitation from this method comes from the effect of the sampling variance in this limited area when trying to extrapolate to the entire >4,000 deg² footprint.
(3) Clustering redshift (WZ). Clustering redshift is a measurement where a sample of galaxies with unknown redshifts (in our case, the photometrically measured BAO galaxies) is angularly correlated with a sample of galaxies where the redshifts are known (a spectroscopic sample). Due to the clustering of galaxies, galaxies that are at the same redshift will tend to have a strong angular correlation compared to chance. Thus, computing the angular correlations of the BAO sample and spectroscopic samples at many thin redshift bins can give us a measure of the redshift distribution of the BAO sample.
For our clustering redshift measurements, we utilize the final Baryon Oscillation Spectroscopic Survey (BOSS) LOWZ and CMASS galaxy samples [97] and the final eBOSS, ELG [70], LRG,

---

[3]In previous papers and databases, this was named Z_MEAN inherited from other methods in which the main estimate of the redshift was the mean of a PDF.

[4]In previous papers and databases, this was named Z_MC inherited from other methods in which a secondary estimate of the redshift was Monte-Carlo sampled from the PDF.
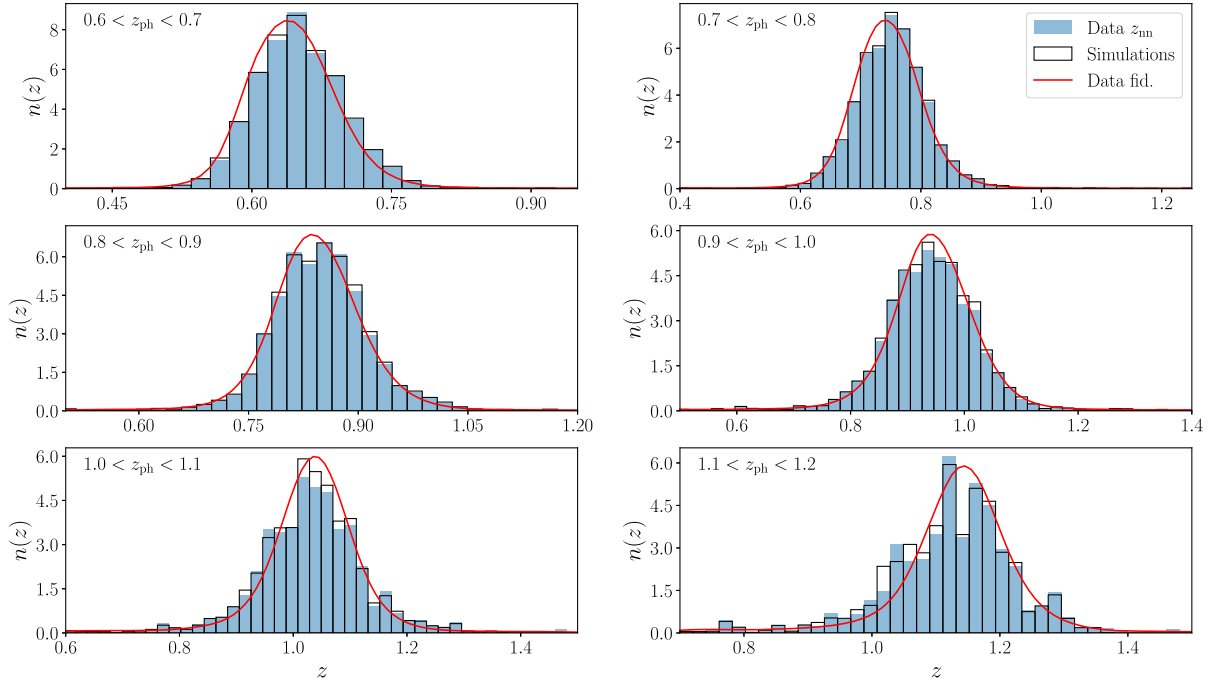
FIG. 2. Redshift distributions of the six tomographic bins, split by z_{ph}. In red, we show the fiducial $n(z)$ assumed for the Y6 BAO sample; see how these are constructed in Sec. II E. The blue histograms show the $n(z_{nn})$ obtained from the DNF nearest neighbor estimation. z_{nn} is the assumed input distribution for constructing the ICE-COLA simulations, whose final $n(z)$ distribution is shown as an empty histogram (black outline).

and QSO samples [98]. This is the same set of spectroscopic galaxies used for clustering redshifts in [99]. These samples overlap approximately 15% of the DES Y6 footprint. The methodology for the clustering redshifts measurements used here is nearly identical to that of [99], including choices of scales used, methods of uncertainty estimation, and galaxy bias correction.

We remark that the three different methods are largely independent of one another. A thorough description and comparison of these calibrations and combinations is performed in [50], together with the description of the method used as the final choice for fiducial $n(z)$.

1. Fiducial redshift distribution

Our fiducial choice of $n(z)$ calibration combines the DNF information coming from the PDF with either WZ or VIPERS. We take the DNF PDF as the shape of our $n(z)$ to profit from its smoothness, although we know that this curve tends to overestimate the spread. On the other hand, we consider that for redshift bins 1–4 ($z_{ph} < 1$), WZ provides the most robust estimation of the mean and width of the distribution. Hence, we use the shift-and-stretch technique (see [50,99,100]): We displace the PDF $n(z)$ distribution and widen/narrow it until it best fits a target $n(z)$ distribution, which in this case, is the WZ. For $z_{ph} > 1$, there are not enough spectroscopic galaxies for precise enough WZ measurements, and we trust better VIPERS

direct calibration to estimate the mean and width of the distribution. Hence, for bins 5–6 we use the PDF DNF *shifted* and *stretched* with VIPERS as the target.

The fiducial $n(z)$ is shown in red in Fig. 2, compared to the data DNF z_{nn} distribution (blue histogram) and to the simulations $n(z)$ (empty histogram), which is constructed to match the data z_{nn} distribution. More details about the simulations are found in Sec. III. The other $n(z)$ distributions mentioned in this section are shown in the companion paper [50].

2. Calibration for PCF

Whereas for two of our analyses (ACF, APS), we only use angular information, for the PCF method, we make use of the radial position of galaxies. In the methodology developed in [73], we model the 3D clustering as a weighted sum of the angular clustering in thin redshift bins. As part of this modeling, we require that we have the $n(z)$ distribution in thin z_{ph} bins.

While redshift bins of equal width were considered in [73], here, we increase the bin width with redshift because the photo-z quality deteriorates substantially at high z, especially at $z \gtrsim 1$. The bin widths are set in geometric sequence with a ratio of 1.078 so that there are 22 bins in the range $0.6 < z_{ph} < 1.2$. We follow exactly the same methodology as above. The first 17 bins (up to $z_{ph} = 1.02$) are calibrated with WZ and the remaining ones

by VIPERS. We refer the readers to an appendix of [50] for more details.

III. SIMULATIONS

In order to create the galaxy mock catalogs (from now, *mocks*) for the validation of the BAO analysis, we follow a practically identical approach as in Y3, but now calibrated on the Y6 sample. Hence, we describe the methodology briefly here and refer the reader to [63] for more information. Part of the methodology to construct these mocks builds upon the methodology developed for Y1 [61].

We created a set of 1952 mock catalogs, closely reproducing several crucial data attributes, including the observational volume, galaxy abundance, true and photometric redshift distribution, and clustering as a function of redshift.

To achieve this, we employed the ICE-COLA code [62], conducting 488 fast quasi-N-body simulations. These simulations utilize second-order Lagrangian perturbation theory (2LPT) in conjunction with a particle-mesh (PM) gravity solver. Our ICE-COLA algorithm extends the capabilities of the COLA method [101], enabling on-the-fly generation of light-cone halo catalogs and weak lensing maps.

Each simulation involves 2048^3 particles enclosed within a box of $1536 \, h^{-1} \mathrm{Mpc}$ on a side. In order to enhance our statistical power while keeping computational resources manageable, we replicated this volume 64 times using the periodic boundary conditions, effectively creating a full-sky light cone extending up to redshift $z = 1.43$. In these simulations, the ICE-COLA universe has the same cosmology as the benchmark MICE *Grand Challenge* simulation [102,103] (used for validation): $\Omega_m = 0.25$, $\Omega_\Lambda = 0.75$, $\Omega_b = 0.044$, $n_s = 0.95$, $\sigma_8 = 0.8$, and $h = 0.7$.

Generating the galaxy mocks entailed populating halos based on a hybrid halo occupation distribution and halo abundance matching model, using two free parameters per tomographic bin. We calibrated these parameters through automatic likelihood minimization to match the clustering of the data. For that, we use three points of the angular correlation at $0.5 < \theta < 1.0$ deg, while the rest of the correlation function was kept blinded. Additionally, we derived photometric redshifts for the mock galaxies by applying a mapping between the true redshift and the observed redshift z_{ph}. This mapping is constructed from the 2D histogram $N(z_{ph}, z_{nn})$ of the data with DNF and assuming that it is a good representation of the $N(z_{ph}, z_{true})$. This choice is different to Y3, where we used $N(z_{ph}, z_{vipers})$ to characterize the redshift distribution. However, in Y6, we found that this characterisation is noise dominated in the higher redshift bins.

Finally, we applied four non-overlapping Y6 footprint masks on each full-sky halo catalog to multiply the number of galaxy mocks by four, allowing us to validate our analysis down to increased accuracy.

As we already showed in Fig. 2, the agreement between the $n(z)$ distribution of the mocks and the data z_{nn} is excellent up to some noise. This is expected by the way we constructed the redshift errors on the mocks from the $N(z_{ph}, z_{nn})$ distributions. On the other hand, in Fig. 3, we show the galaxy clustering comparison of data versus mocks, finding a good level of visual agreement. When comparing the galaxy biases [shown in Sec. IV A and mathematically introduced in Eq. (10)], some bins show some level of disagreement, partially due to the limitation in the number of scales and partially because of using a limited number of mocks for the calibration for the sake of reducing computing resources (see [63] for details). Part of this disagreement may also come from using slightly different scales for the bias measurements and because the cosmology of the mocks will likely not correspond to the underlying one in the data. Additionally, when comparing the ACF of mocks and data, we find $\chi^2/\mathrm{d.o.f.} = 125/107$ for $\theta \in [0.5, 5]$ deg and $\chi^2/\mathrm{d.o.f.} = 89/95$ for $\theta \in [1, 5]$ deg, which indicates a good agreement, especially at large scales. Given this good agreement at the scales used for fitting the BAO, we do not expect that having a different best fit bias will affect the usage of the mocks for the purposes described below.

These simulations will have a crucial role in making different analysis choices and validating the analysis pipeline. Generally, they will not be used for the covariance estimation, because we showed in [63] that the replication of boxes explained above leads to significant spurious correlations between parts of the data vector. Our baseline covariance will be computed from theory using CosmoLike; see Sec. IV D.

IV. ANALYSIS METHODOLOGY

The methodology for the analysis we follow is very similar to that in Y3 [76], with the main exception that we now include the projected correlation function, $\xi_p(s_\perp)$.

A. Analysis setups

We consider three different main analysis setups for our analysis and validation, varying the cosmology, $n(z)$ and galaxy bias, depending on the particular needs of a particular analysis. We have one setup more oriented to test our methodology on the mocks (mocklike), our fiducial setup for the data assuming PLANCK cosmology (datalike) and a variation of it with the cosmology of the mocks (datalike-mice), all described below.

(i) *Mocklike.* The mocks are based on MICE Cosmology, and we will be assuming it in this setup: $\Omega_m = 0.25$, $\Omega_\Lambda = 0.75$, $\Omega_b = 0.044$, $n_s = 0.95$, $\sigma_8 = 0.8$, $h = 0.7$, and $M_\nu = 0$ eV. The redshift distribution assumed is that of the mocks (empty histograms in Fig. 2), which is based on z_{nn}. Finally, we use the galaxy bias measured on the mock catalogs using
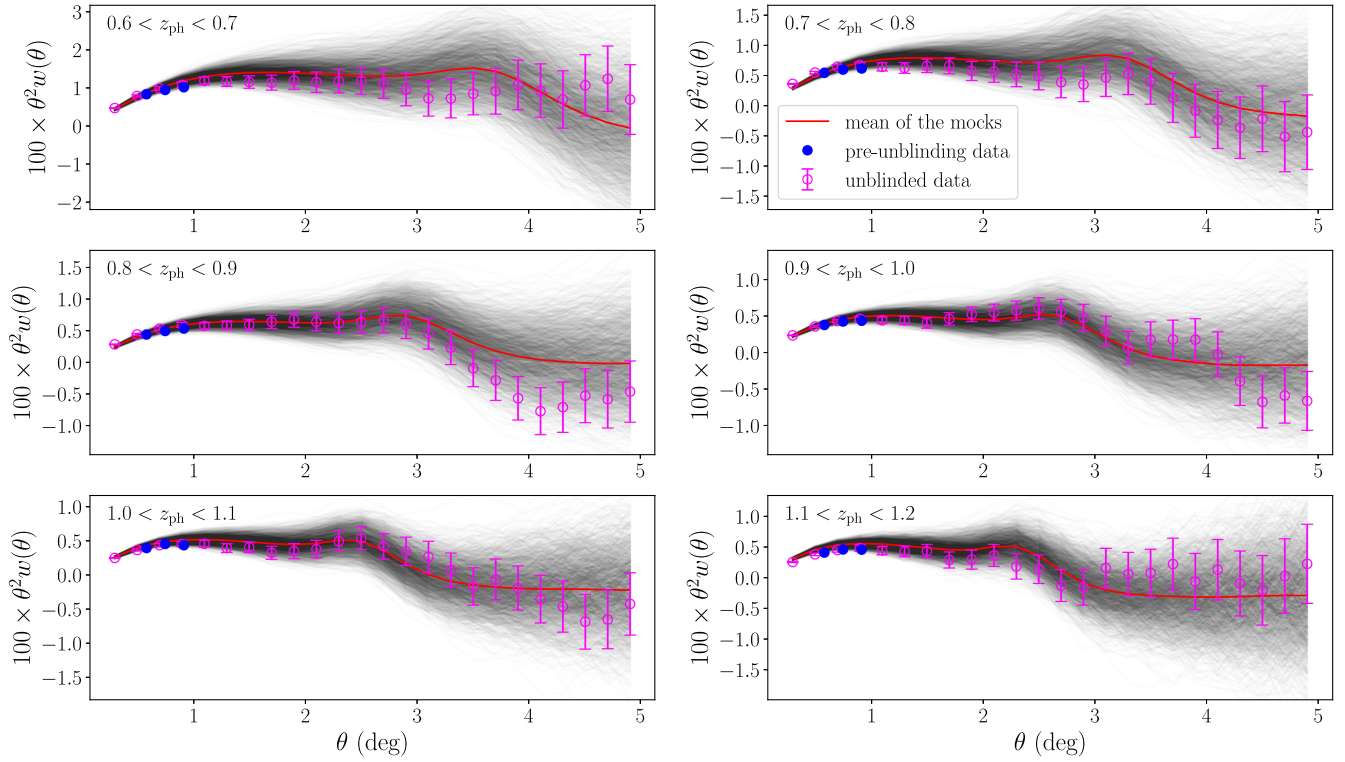
FIG. 3.   Angular correlation function of the mocks compared to the data. In red, we show the mean of the ACF of all the mocks, whereas in black, we show all the individual ACF of the 1952 ICE-COLA mocks. On filled circles, we mark the three data points used for calibration prior to unblinding, whereas on empty circles, we can see full unblinded ACF, with the fiducial error bars by CosmoLike (see Sec. IV D).

the ACF in $1.5 < \theta < 5$ deg: $b = [1.663, 1.547, 1.633, 1.793, 2.038, 2.446]$ for the six bins, respectively.

(ii) *Datalike*. This is the default setup for the data analyses. We assume PLANCK cosmology ($\Omega_m = 0.31$, $\Omega_\Lambda = 0.69$, $\Omega_b = 0.0481$, $n_s = 0.97$, $\sigma_8 = 0.8$, $h = 0.676$, and $M_\nu = 0.06 eV$ [104]), the fiducial $n(z)$ (combination of DNF PDF with either WZ or VIPERS; see Sec. II E) and the galaxy bias measured on the data at angles $0.5 < \theta < 2$ deg: $b = [1.801, 1.805, 1.813, 1.957, 2.113, 2.413]$.

This measurement of the bias was produced just before we started running the pre-unblinding tests, once the data validation was considered finalized, a much later stage than when the mocks were constructed.

(iii) *Data-like-mice*. This auxiliary setup is used to check how results change when assuming MICE cosmology. For that, we still assume the fiducial $n(z)$, and we refit the bias on the data, obtaining $b = [1.650, 1.640, 1.640, 1.752, 1.873, 2.108]$. For comparison to the bias obtained in the mocks (mocklike), the error on these biases (which will be larger than for mocklike, since here we are only using the scales $0.5 < \theta < 2$ deg) are $\sigma_b = [0.042, 0.044, 0.046, 0.050, 0.067, 0.102]$.

Some particular tests will require hybrid auxiliary setups that we will specify, but the majority of the analyses are run using one of the three above, especially the first two.

B. Clustering measurements

1. Random catalog

The starting point to measure all clustering statistics is the creation of a random catalog with 20 times as many objects as our sample. This was found to be more than sufficient to avoid any additional noise coming from the randoms. The random catalog is created by sampling the mask described in Sec. II C with a HEALPix NSIDE of 4096. We down-sample the pixels according to their fraction of coverage, which we remind the reader is always larger than 80%.

In Sec. IV B 5, we explain how we correct the clustering measurements from additive stellar contamination, quantified by f_{star}. The method proposed there is equivalent to assigning all the objects in the random catalog a weight of $1/(1 - f_{star})$.

2. Angular correlation function: $w(\theta)$

Once we have the random sample, the two-point angular correlation function is estimated using the Landy-Szalay estimator [105]

$$w(\theta) = \frac{DD(\theta) - 2DR(\theta) + RR(\theta)}{RR(\theta)}, \qquad (5)$$

where DD, DR, and RR are the normalized counts of data-data, data-random, and random-random pairs, respectively, separated by $\theta \pm \Delta\theta/2$, with $\Delta\theta$ being the bin size. We start by computing the ACF with a bin size of $\Delta\theta = 0.05$ degress, which is the minimum bin that we consider, but the pair counts can be later combined in broader bins. Eventually, after testing different bin sizes in Sec. V B, our default binning is set to $\Delta\theta = 0.20$ deg. We can see in Fig. 3 that the BAO feature is located at ∼3 deg and has a width of around 1 deg. Hence, any of these configurations is able to resolve it. We will be considering a maximum separation of 5 deg.

Before unblinding, we compared the ACF measurements with two different codes: TreeCorr [106] and CUTE [107]. The χ^2 between the two measurements (with the full covariance) is found to be 0.05, and its root mean square relative error is $\sqrt{\frac{1}{N}\sum(\Delta w/\sigma)^2} = 0.006$. With this excellent agreement and with the more detailed comparison performed in Y3, we consider the data vector to be validated.

3. Angular power spectrum: C_ℓ

To estimate the clustering signal of galaxies in harmonic space, we use the pseudo-C_ℓ (PCL) estimator [108]. In particular, we use NaMaster[5] implementation [109]. We commence by constructing tomographic galaxy overdensity maps using the HEALPix pixelization scheme at a resolution parameter of NSIDE = 1024. This corresponds to a mean pixel size of ∼0.06 degrees, at least 1 order of magnitude below the expected angular separation of the BAO signal. The equal-area pixelization facilitates the computation of galaxy overdensity maps as follows:

$$\delta_p = \frac{N_p \sum_{p'} w_{p'}}{w_p \sum_{p'} N_{p'}} - 1, \qquad (6)$$

where $N_p = \sum_{i \in p} v_i$ gives the weighted number of galaxies at a given pixel p, with v_i representing the weight associated with the ith galaxy as given by the systematics weights, Sec. II D. On the other hand, w_p gives the effective fraction of the area covered by the survey at pixel p, as given by our mask, Sec. II C.

The inherent discreteness of galaxy number counts introduces a shot-noise contribution to the autocorrelation galaxy clustering spectra, also known as noise bias. We assume this noise to be Poissonian and estimate it analytically following [109–111]. Subsequently, we subtract this estimated noise bias from our power spectrum estimates. Any deviations from the Poissonian approximation are expected in the form of an additive constant and are anticipated to be captured by broadband terms in our template, having minimal impact on the BAO feature detection.

We bin the angular power spectrum estimates into bandpowers, assuming uniform weighting for all modes within each band. Employing a piecewise-linear binning scheme, we construct contiguous bandpowers with varying bin widths of $\Delta\ell = 10, 20,$ and 30, ranging from $\ell_{\min} = 10$ up to $\ell = 2048$. This binning strategy ensures adequate signal-to-noise ratios across the bandpowers while maintaining flexibility for scale cuts; see Table III for different analysis choices on the mocks.

After testing on the mocks, we adopted as fiducial choices $\ell_{\min} = 10$, $\Delta\ell = 20$, and an $\ell_{\max}$ scale cut approximately corresponding to a $k_{\max} = 0.211$ Mpc^{-1}h under the Limber relation, $k_{\max} = \ell_{\max}/r(\bar{z})$, evaluated at the mean redshift of each tomographic bin and the fiducial cosmology of the mocks. We have verified that changing the cosmology to the PLANCK one does not introduce significant changes on our scale cuts. This ℓ binning allows us to resolve approximately five BAO cycles on each redshift bin (Fig. 9). The resulting $\ell_{\max}$ values for each redshift bin are 510, 570, 630, 710, 730, and 770. Finally, when constructing the likelihood, we consistently bin the theory predictions into the same bandpowers of the measurements following [109].

4. Projected correlation function: $\xi_p(s_\perp)$

The projected correlation function (PCF) method starts by computing the full 3D correlation function in terms of the *observed* (in $z_{\rm ph}$ space) comoving distance between any pair of galaxies (or randoms or galaxy random) along and across the line of sight: $s_\parallel$, $s_\perp$. For that, we transform $z_{\rm ph}$ to comoving distances using a fiducial cosmology (see Sec. IV A for the two cosmologies considered). Once we have that, we compute the anisotropic 3D correlation function in a similar way to the ACF, with the Landy-Szalay estimator:

$$\xi(s_\perp, s_\parallel) = \frac{DD(s_\perp, s_\parallel) - 2 \cdot DR(s_\perp, s_\parallel) + RR(s_\perp, s_\parallel)}{RR(s_\perp, s_\parallel)}. \quad (7)$$

We use a binning of $\Delta s_\perp = 1 \; h^{-1}$Mpc and $\Delta s_\parallel = 1 \; h^{-1}$Mpc (again, we recombine the pair counts at a later step to obtain broader bins in $s_\perp$: $\Delta s_\perp = 5h^{-1}$ Mpc). We compute these correlations both with CUTE and with PYCORR,[6] finding good agreement between the two but the latter to be considerably faster and adopting it for our analysis.

---

[5]https://github.com/LSSTDESC/NaMaster.

[6]https://github.com/cosmodesi/pycorr.

Once we have the 3D clustering, we integrate over the line of sight to obtain the PCF:

$$\xi_p(s_\perp) = \frac{\int_0^1 W(\mu)\xi(s_\perp(s,\mu), s_\parallel(s,\mu))d\mu}{\int_0^1 W(\mu)d\mu}, \quad (8)$$

where μ is the orientation with respect to the line of sight ($\mu = \cos\theta$, with $\tan\theta = s_\parallel/s_\perp$) and $W(\mu)$ a weighting function that can be optimized. Here, we follow an approach that is different to that of Y1 [75] and Y3 [76] key papers, which were based on the methodology proposed in [72], with a method to obtain the $W(\mu)$ from Fisher information. On follow-up analyses of Y3, we developed and applied a new version of the method that was able to account for non-Gaussian distribution of the redshift errors [73,74], unlike previous analyses. To increase the signal-to-noise and stability of the analyses, we apply a cutoff Gaussian weighting [74]:

$$W(\mu) = W_{\rm G}(\mu; \sigma_\mu, \mu_{\rm max}) = \begin{cases} \exp\left(-\frac{\mu^2}{2\sigma_\mu^2}\right) & \text{if } \mu < \mu_{\rm max}, \\ 0 & \text{otherwise}, \end{cases}$$

$$(9)$$

with $\mu_{\rm max} = 0.8$ and $\sigma_\mu = 0.3$.

One of the advantages of PCF is that the BAO is always seen at the same position in $s_\perp$ for different redshifts, if the assumed cosmology is roughly correct, contrary to ACF or APS. This allows us to consider all the tomographic bins together without losing too much information; i.e., the data compression is close to optimal; this was the approach taken in [74–76]. Here, we will keep this approach for visualisation purposes (in order to see one line with all the BAO SNR on it: left panel of Fig. 10), but not for the default BAO analysis. During the validation of the method with Y6 mocks, we found slightly tighter constraints on the BAO when considering the $N_z = 6$ tomographic bins for the clustering measurements. This is expected given for $N_z = 6$, we essentially combine data at the level of likelihood rather than data vector [74]. This also eases the comparison with the ACF and APS when we study isolating/removing one specific bin or similar tests.

5. Correcting for additive stellar contamination

As mentioned in Sec. II B, we have quantified that between $f_{\rm star} = 0.7\%$ and 3.3%, depending on the tomographic bin, of our objects are actually stars. This has a multiplicative effect that is corrected with the systematic weights described in Sec. II D as other foregrounds or observational condition maps. However, stars have also an additive contribution to the observed number density of galaxies due to contamination. To first order, these stars can be considered unclustered objects that contribute both to

RR and DD equally, diluting all two-point functions by a factor $(1 - f_{\rm star})^2$. For this reason, we correct our measurements of $w(\theta)$, C_ℓ, and $\xi_p(r_\perp)$ with a factor $(1 - f_{\rm star})^{-2}$; more details in our companion paper [50] and in [112,113].

This correction reaches up to a 6.5% level on the clustering amplitude, although we do not expect this correction to affect the measurement of the BAO that has a parameter B absorbing the amplitude of the clustering [see Eq. (14) below]. Nevertheless, we include this correction in all our measurements from the data.

C. BAO template

Our approach to measuring the BAO distance is based on a template fitting method. In order to generate the BAO template for our observables, we first need to generate a reliable model for the 3D power spectrum [$P(k)$], from which the projected/angular clustering can be computed. For that, we follow the same methodology as in Y3, summarized below.

We start from the linear power spectrum $P_{\rm lin}(k)$ generated by CAMB [114]. The main modification to this model comes from the inclusion of the BAO peak broadening due to nonlinearities [115,116]. We model this by splitting the power spectrum into a *nonwiggle* ($P_{\rm nw}$) and a *wiggle* ($P_{\rm lin} - P_{\rm nw}$) component and smoothing the *wiggle* component anisotropically via Σ:

$$P(k,\mu) = (b + \mu^2 f)^2[(P_{\rm lin} - P_{\rm nw})e^{-k^2\Sigma^2} + P_{\rm nw}], \quad (10)$$

where we have also included the effect coming from galaxy bias (b) and redshift space distortions ($\mu^2 f$) [117], with the latter one proportional to the growth rate f.

We model the nonwiggle component using a 1D Gaussian smoothing in log space following Appendix A of [118]. We also follow the infrared resummation model [119,120] to compute the damping scale $\Sigma(\mu)$ [121,122], with respect to the line of sight (see details in [76]).

Once we have a $P(k,\mu)$, we can decompose it into multipoles, $P_\ell(k)$, perform a Hankel transform to obtain the configuration space multipoles, $\xi_\ell(s)$, and then reconstruct the anisotropic redshift-space correlation function $\xi(s,\mu)$. From there, the angular correlation function is obtained by projecting 3D clustering into the angle subtended by two galaxies in the celestial sphere θ. For that, we weight $\xi(s,\mu)$ by the redshift distribution $n(z)$ (normalized to integrate to 1) of each tomographic redshift bin in a double integral:

$$w(\theta) = \int dz_1 \int dz_2 n(z_1)n(z_2)\xi(s(z_1, z_2, \theta), \mu(z_1, z_2, \theta)).$$

$$(11)$$

We then compute the C_ℓ template by evaluating $w(\theta)$ in 300 logarithmic spaced points from 0.001 to 179.5 deg and transforming it to the harmonic space:

$$C_\ell = 2\pi \int_{-1}^{1} d(\cos\theta) w(\theta) L_\ell(\cos\theta), \qquad (12)$$

where L_ℓ is the Legrendre polynomial of order ℓ.

Our modeling of the PCF starts by computing the general auto and cross-correlations ACF w_{ij} using Eq. (11) in thin photo-z bins, whose calibration has been described in Sec. II E 2. Then, we map the general ACF to PCF by

$$\xi_p(s,\mu) = \frac{\sum_{ijk} f_{ijk} w_{ij}(\theta_k; z_i, z_j)}{\sum_{ijk} f_{ijk}}, \qquad (13)$$

where f_{ijk} denotes the weight accounting for the number of the cross bin pairs in $w_{ij}(\theta_k)$ falling into the s and μ bins. As for the data measurements, we project $\xi_p(s,\mu)$ to the transverse direction using weight Eq. (9) to get $\xi_p(s_\perp)$. We refer the reader to [73] for more details.

The procedure described above results in the three templates corresponding to ACF, APS, and PCF are all derived consistently.

Finally, our model (M) will contain the BAO template component (T) described above for $w(\theta)$, C_ℓ, or $\xi_p(s_\perp)$, an amplitude rescaling factor B and a smooth component $A(x)$:

$$M(x) = B T_{\mathrm{BAO},\alpha}(x') + A(x). \qquad (14)$$

The term $A(x)$ is introduced to absorb smooth (not a sharp feature) components that may come from remaining theoretical or observational systematic errors in the clustering. We will model it as a sum of power laws, and we will study in Sec. V B what option gives the best behavior when fitting the BAO on the mock catalogs.

In the case of the ACF, we have $x = \theta$ and T corresponding to w as given by Eq. (11). The rescaled coordinate x' is $\alpha\theta$, where α is the BAO shift parameter containing the cosmological information from the fit, and the function A are modeled as

$$A(\theta) = \sum_i \frac{a_i}{\theta^i}. \qquad (15)$$

For the APS, T is the C_ℓ obtained from Eq. (12), $x = \ell$, $x' = \ell/\alpha$, and A is

$$A(\ell) = \sum_i a_i \ell^i. \qquad (16)$$

Finally, for the PCF, $T(x)$ denotes $\xi_p(s_\perp)$ from Eq. (13), $x' = \alpha s_\perp$ and A is

$$A(s_\perp) = \sum_i \frac{a_i}{s_\perp^i}. \qquad (17)$$

D. Covariance matrix

1. Covariance for ACF and APS

Following our approach for the BAO analysis from Y3 data [76], our fiducial covariance matrices are estimated analytically, using the CosmoLike code for ACF and APS [123–125]. The covariance of the angular correlation function $w(\theta)$ at angles θ and θ' is related to the covariance of the angular power spectrum by

$$\mathrm{Cov}(w(\theta), w(\theta'))$$
$$= \sum_{\ell,\ell'} \frac{(2\ell+1)(2\ell'+1)}{(4\pi)^2} \overline{P_\ell}(\theta) \overline{P_{\ell'}}(\theta') \mathrm{Cov}(C_\ell, C_{\ell'}), \tag{18}$$

where $\overline{L_\ell}(\theta)$ are the Legendre polynomials averaged over each angular bin $[\theta_{\min}, \theta_{\max}]$ and are defined by

$$\overline{P_\ell} = \frac{\int_{x_{\min}}^{x_{\max}} dx P_\ell(x)}{x_{\max} - x_{\min}} = \frac{[P_{\ell+1}(x) - P_{\ell-1}(x)]_{x_{\min}}^{x_{\max}}}{(2\ell+1)(x_{\max} - x_{\min})}, \tag{19}$$

with $x = \cos\theta$ and $x_{\{\min,\max\}} = \cos\theta_{\{\min,\max\}}$ (see, e.g., [126] for more details).

We have tested that including non-Gaussian contributions to the covariance estimation, such as the trispectrum and the supersample covariance terms, does not impact our results. Given that, the Gaussian covariance of the angular power spectrum in a given tomographic bin is given by [123,126]

$$\mathrm{Cov}(C_\ell, C_{\ell'}) = \frac{2\delta_{\ell\ell'}}{f_{\mathrm{sky}}(2\ell+1)} \left(C_{\ell'} + \frac{1}{n_g} \right)^2, \quad (20)$$

where δ is the Kronecker delta function, n_g is the number density of galaxies per steradian, and f_{sky} is the observed sky fraction, which is used to account for partial-sky surveys. However, we go beyond the f_{sky} approximation by taking into account how the exact survey geometry suppresses the number of pairs of positions in each angular bin $\Delta\theta$ (see [127] and Appendix C of [128] for more details). Redshift space distortions are included through the C_ℓ's in Eq. (20).

In the context of harmonic space analysis, we commence by employing the CosmoLike predictions for the angular power spectra. Subsequently, we calculate analytical Gaussian covariance matrices that account for broadband binning and partial sky coverage within the context of the PCL estimator, as outlined in [129,130]. The coupling terms are computed using the NaMaster implementation [109,130].

Similarly to Y3, we have validated the CosmoLike covariance with estimates from the ICE-COLA, FLASK mocks [131], and also with the covariance developed in [66], finding consistent results (see Tables II–IV).

2. Covariance for PCF

For the projected correlation function, we also rely on a theoretical covariance. In this case, the method follows [73], which builds up on the covariance for ACF developed in [66]. That latter ACF covariance follows a similar approach as the CosmoLike one explained above and has been validated against that code during this study. Furthermore, in line with the CosmoLike covariance, we have included the mask correction as well [127].

Following from Eq. (13) and using the same f_{ijk} coefficients described there, we can simply construct the 3D clustering covariance, C^{ξ_p} as a sum over the angular covariance, C^w:

$$C^{\xi_p}_{\{s,\mu\}\{s',\mu'\}} = \frac{\sum_{ijk}\sum_{lmn} f_{ijk} f_{lmn} C^w_{\{z_i,z_j,\theta_k\}\{z'_l,z'_m,\theta_n\}}}{\sum_{ijk} f_{ijk} \sum_{lmn} f_{lmn}}. \quad (21)$$

We then get the covariance for $\xi_p(s_\perp)$ by projecting the covariance to the transverse direction using the weight W_G in Eq. (9). We do not apply the covariance corrections introduced in [73] as it has little effect on the final results.

A visual representation of the Y3 covariance for ACF and APS is shown in [76], whereas the PCF covariance is shown in [132]. The Y6 covariances are not shown here but follow a similar structure to those from Y3.

E. Parameter inference

Given our data vector d from the clustering measurements (ACF, APS or PCF in Sec. IV B), the model M for a given set of parameters p [Eq. (14) in Sec. IV C] and the covariance C, (Sec. IV D), the χ^2 describes the goodness of fit between the data and the model, and it is given by

$$\chi^2(p|d) = \sum_{ij}[d - M(p)]_i C^{-1}_{ij}[d - M(p)]_j. \quad (22)$$

Then, assuming a Gaussian likelihood $\mathcal{L}$, we have

$$\mathcal{L}(p|d) \propto e^{-\frac{\chi^2}{2}}. \quad (23)$$

We then consider our best fit as the model with the highest likelihood or, equivalently, lowest χ^2. We follow a similar procedure to [66] to minimize the χ^2. This implies, first, to analytically fit the broadband parameters A_i [Eqs. (15)–(17)], profiting from their linear contribution to the model. After that, the χ^2 is numerically minimized with respect to the amplitude B. Finally, we end up with a χ^2 as a function of α, which is our reported likelihood for each of the three methods (ACF, APS, PCF).

From this point, we consider our error σ_α as the half-width of the α region with $\Delta\chi^2 = 1$ around the minimum.

If the 1-σ region defined this way falls outside the $\alpha \in [0.8, 1.2]$ region, then we consider this as a nondetection. We will see in Sec. V B that the individual errors obtained from this method agree reasonably well with the scatter of the best fit α. At the stage of the combination of ACF, APS, and PCF (Sec. V C), we estimate the covariance of the three best fits from the mocks and implicitly assume that they are Gaussianly distributed. As we will see in Table V, the resulting combined measurement (AVG) has an estimated error that captures very well the scatter of the best fit estimate.

We also tested different ways to report the 1-σ error as a summary of the likelihood. We could define $\sigma_{\tilde{\sigma}^2}$ as the standard deviation of the likelihood from the second moment or σ_{L68} as the half-width of the region that contains 68% of the integral of the likelihood. These different definitions had some small impact on the error (somewhat larger for APS) but were found not to affect the conclusions drawn in the tests on the mocks or on the data.

At this stage, we remind the reader that α measures a shift of the BAO position with respect to the BAO position in the template, computed at our fiducial cosmology (defined in Sec. IV A). This relates to cosmology, through the comoving size of the sound horizon r_d and angular distance D_M:

$$\alpha = \frac{D_M(z)}{r_d} \frac{r_d^{\text{fid}}}{D_M^{\text{fid}}(z)}. \quad (24)$$

This equation needs to be evaluated at an effective redshift that we define as

$$z_{\text{eff}} = \frac{\sum_i w_{i,\text{sys}} \cdot w_{i,\text{FKP}} \cdot z_{\text{ph}}}{\sum_i w_{i,\text{sys}} \cdot w_{i,\text{FKP}}} = 0.851, \quad (25)$$

where the w_{FKP} weights are inverse-variance weights that we compute following Eq. (16) of [72], and $w_{i,\text{sys}}$ are the systematic weights described in Sec. II D.

We note that the definition of z_{eff} is somewhat arbitrary. Different definitions we have tried lead to differences of up to $\Delta z_{\text{eff}} = 0.035$. However, since α contains a ratio $D_M(z)$ to $D_M^{\text{fid}}(z)$, as long as both functions evolve slowly with redshift, the uncertainty on z_{eff} does not have much effect on cosmology. For example, comparing $D_M(z)$ from MICE cosmology to $D_M(z)$ from PLANCK cosmology (already a big change), only leads to a difference of $\Delta\alpha = 0.001$ for $\Delta z_{\text{eff}} = 0.035$; this is at the level of $1/20\sigma_\alpha$. Hence, we choose the definition above for consistency with Y1 and Y3 analyses. Finally, if we consider the different redshift calibrations discussed in Sec. II E and [50], there is an uncertainty on the mean redshift of the sample of about $\Delta z = 0.004$; this is 1 order of magnitude below the uncertainty associated to the z_{eff} definition.

F. Combination of BAO from ACF, APS, and PCF

We follow the methodology described in [133,134] to combine our three correlated statistics. We express the covariance matrix between ACF, APS, and PCF as

$$\text{COV}_{ij} = \langle \delta\alpha_i \delta\alpha_j \rangle, \quad (26)$$

where $i, j \in \{\text{ACF}, \text{APS}, \text{PCF}\}$, and $\delta\alpha_i = \alpha_i - \langle\alpha_i\rangle$, with $\langle\alpha_i\rangle$ the plain average of the three measurements. We define the optimally weighted average of α as

$$\alpha_{\text{AVG}} = \sum_i w_i \alpha_i, \quad (27)$$

where the optimal weights w_i are to be found. Writing $\delta\alpha_{\text{AVG}} = \sum_i w_i \delta\alpha_i$ and using the definition of covariance matrix, Eq. (26), we find

$$\sigma_{\text{AVG}}^2 \equiv \text{COV}_{\text{AVG,AVG}} = \sum_{ij} w_i w_j \text{COV}_{ij}. \quad (28)$$

To minimize σ_{AVG}^2 subject to the condition $\sum_i w_i = 1$, we use the Lagrange multiplier technique. Writing

$$\sigma_{\text{AVG}}^2 = \sum_{ij} w_i w_j \text{COV}_{ij} + \lambda\left(\sum_i w_i - 1\right) \quad (29)$$

and setting the derivative of σ_{AVG}^2 with respect to the w_i and λ to 0, we find

$$w_i = \frac{\sum_k \text{COV}_{ik}^{-1}}{\sum_{jk} \text{COV}_{jk}^{-1}}. \quad (30)$$

We then calculate the error associated to α_{AVG} via Eq. (28), but using the errors (σ_{α_i}) measured on the α for the different estimators instead of the variance from the covariance matrix. Explicitly,

$$\begin{aligned}
\sigma_{\alpha_{\text{AVG}}}^2 = (&w_{\text{ACF}}^2 \sigma_{\alpha_{\text{ACF}}}^2 + w_{\text{APS}}^2 \sigma_{\alpha_{\text{APS}}}^2 + w_{\text{PCF}}^2 \sigma_{\alpha_{\text{PCF}}}^2 \\
&+ 2w_{\text{ACF}} w_{\text{APS}} \sigma_{\alpha_{\text{ACF}}} \sigma_{\alpha_{\text{APS}}} \rho_{\text{ACF,APS}} \\
&+ 2w_{\text{APS}} w_{\text{PCF}} \sigma_{\alpha_{\text{APS}}} \sigma_{\alpha_{\text{PCF}}} \rho_{\text{APS,PCF}} \\
&+ 2w_{\text{ACF}} w_{\text{PCF}} \sigma_{\alpha_{\text{ACF}}} \sigma_{\alpha_{\text{PCF}}} \rho_{\text{ACF,PCF}}), \quad (31)
\end{aligned}$$

where $\rho_{i,j}$ is the cross-correlation coefficient measured from the mocks and will be detailed in Sec. V C.

V. ANALYSIS VALIDATION

Once we have set up the methodology, we validate it in this section. First, we will study the robustness of our method to the choice of redshift calibration in Sec. V A. Then, in Sec. V B, we will use the simulations presented in Sec. III to validate the accuracy of our methodology for our three estimators: angular correlation function, angular

power spectrum, and projected correlation function. Finally, in Sec. V C, we validate the method to combine the statistics. From these tests, we can derive a systematic error associated with each of the estimators.

A. Robustness against redshift calibration

As discussed in Sec. II E, characterizing the redshift distribution of galaxy samples is one of the most important and challenging tasks in photometric surveys. A detailed comparison of different methods to characterize the redshift distribution, $n(z)$, of the six tomographic bins is presented in [50] and summarized in Sec. II E. This results in a series of estimations of $n(z)$ for our tomographic bins, having three estimations largely independent (DNF, VIPERS, and WZ). From a combination of those estimates, we obtain our fiducial $n(z)$.

In this section, we estimate the offset we may obtain in the measured BAO if we assumed one $n(z)$ but the *true* $n(z)$ were a different one. For that, we generate a data vector assuming the fiducial $n(z)$ and fit it with the methodology explained in Sec. IV using a template generated with another $n(z)$. While we test the $n(z)$ assumption, the rest of the choices (cosmology and bias) follow the datalike setup (Sec. IV A).

The results are presented in Table I. The first column (fid.) represents the case in which the assumed and true redshift distributions are identical, naturally, giving unbiased results ($\langle\alpha\rangle = 1.000$). The second column corresponds to the case where we use DNF z_{nn} estimation, which corresponds to the redshift used to construct the mock catalogs described in Sec. III. A different estimation from DNF, the PDF, is used in the fifth column. We also consider independent measurement from direct calibration with the spectroscopic survey VIPERS (third column) and clustering redshifts (WZ, fourth column). Given the great variety and independence of those methods, it is remarkable how small the observed shifts are in the BAO parameter α. Up to bin 5, the largest deviation is $\Delta\alpha = 0.011$ (VIPERS, bin 4, ACF), corresponding to $< 0.3\sigma$ (considering the error on each individual bin reported along with the measurement), but offsets are typically smaller. It is reassuring that these offsets contribute in different directions for different bins and $n(z)$ calibrations, and no coherent offset is found (see also the discussion below when considering *All* the bins together). Remarkably, up to bin 5, the PCF method, which uses radial information, does not seem to be more sensitive to the $n(z)$ calibration than ACF or APS.

For bin 6, the bias on the recovered α goes up to $\Delta\alpha = 0.013$ (z_{nn}) and 0.023 (VIPERS) for the PCF method. However, given the large error bars on this last bin, this only represents 0.14σ and 0.30σ, respectively. Since this bias is at a similar level of relative error as other redshift bins, its possible contribution to biasing the final result is expected to be similar to other bins. Additionally, this relatively large bias only affects one of the three estimators.

TABLE I.   Impact of redshift calibration on the BAO estimation in each redshift bin (1–6) and the combination of the six (All). We generate a mock data vector assuming our fiducial $n(z)$ distribution (and the datalike setup, Sec. IV A) and fit for the BAO shift α assuming a different $n(z)$, as marked in the first row. The entries at the body of the table show the best fit and error obtained in each case, following the methodology described in Sec. IV. We compute this for each of the six tomographic bins (labeled in the first column), presented in six tiers, each of them with the results from the three estimators: angular correlation function (ACF), angular power spectrum (APS) and projected correlation function (PCF). A seventh tier contains the results for the combination of all the bins together (All), and a last entry considers the combination of ACF, APS, and PCF into AVG. The different redshift calibrations are described in Sec. II E.

Bin	Method	Fiducial	DNF z_{nn}	VIPERS	WZ	DNF PDF
1	ACF	1.0001 ± 0.0548	0.9899 ± 0.0550	0.9931 ± 0.0530	1.0014 ± 0.0548	0.9849 ± 0.0556
1	APS	1.0000 ± 0.0617	0.9899 ± 0.0612	0.9927 ± 0.0610	1.0009 ± 0.0623	0.9852 ± 0.0610
1	PCF	0.9998 ± 0.0446	0.9922 ± 0.0458	0.9930 ± 0.0426	0.9994 ± 0.0440	0.9882 ± 0.0460
2	ACF	1.0001 ± 0.0483	0.9921 ± 0.0481	0.9950 ± 0.0463	0.9987 ± 0.0486	0.9924 ± 0.0482
2	APS	1.0000 ± 0.0518	0.9920 ± 0.0514	0.9945 ± 0.0512	0.9987 ± 0.0518	0.9924 ± 0.0514
2	PCF	0.9998 ± 0.0426	0.9938 ± 0.0432	0.9954 ± 0.0408	1.0002 ± 0.0426	0.9930 ± 0.0436
3	ACF	1.0001 ± 0.0420	0.9957 ± 0.0422	0.9918 ± 0.0410	0.9993 ± 0.0417	0.9953 ± 0.0431
3	APS	1.0000 ± 0.0438	0.9957 ± 0.0438	0.9914 ± 0.0435	0.9991 ± 0.0440	0.9954 ± 0.0439
3	PCF	0.9998 ± 0.0412	0.9982 ± 0.0418	0.9942 ± 0.0392	0.9994 ± 0.0406	0.9970 ± 0.0426
4	ACF	1.0001 ± 0.0410	1.0019 ± 0.0419	1.0112 ± 0.0398	0.9983 ± 0.0398	1.0026 ± 0.0427
4	APS	1.0000 ± 0.0402	1.0017 ± 0.0408	1.0106 ± 0.0405	0.9981 ± 0.0403	1.0025 ± 0.0408
4	PCF	0.9998 ± 0.0404	1.0026 ± 0.0422	1.0082 ± 0.0390	1.0010 ± 0.0388	1.0026 ± 0.0428
5	ACF	1.0001 ± 0.0472	1.0030 ± 0.0494	0.9985 ± 0.0452	$\cdots$	0.9991 ± 0.0518
5	APS	1.0000 ± 0.0401	1.0030 ± 0.0409	0.9971 ± 0.0402	$\cdots$	0.9995 ± 0.0410
5	PCF	0.9994 ± 0.0446	1.0018 ± 0.0509	1.0026 ± 0.0434	$\cdots$	0.9978 ± 0.0507
6	ACF	1.0001 ± 0.0683	1.0062 ± 0.0741	1.0048 ± 0.0699	$\cdots$	1.0012 ± 0.0767
6	APS	1.0000 ± 0.0458	1.0067 ± 0.0475	1.0047 ± 0.0466	$\cdots$	1.0022 ± 0.0469
6	PCF	0.9998 ± 0.0831	1.0130 ± 0.0941	1.0234 ± 0.0773	$\cdots$	1.0078 ± 0.0985
All	ACF	1.0001 ± 0.0201	0.9972 ± 0.0206	0.9985 ± 0.0195	$\cdots$	0.9955 ± 0.0210
All	APS	1.0000 ± 0.0190	0.9988 ± 0.0194	0.9989 ± 0.0192	$\cdots$	0.9971 ± 0.0193
All	PCF	0.9998 ± 0.0202	0.9982 ± 0.0214	1.0002 ± 0.0196	$\cdots$	0.9962 ± 0.0216
All	**AVG**	0.9998 ± 0.0193	0.9984 ± 0.0204	1.0001 ± 0.0189	$\cdots$	0.9965 ± 0.0205

Hence, we do not expect this to be a relevant source of systematic error for the α derived from the six bins together and, especially, for the consensus measurement combining the three statistics.

Finally, in the last part of Table I, we show what we consider the main results of this subsection, where we show the results when considering all the redshift bins together (All), as done in our analysis. For this case, we do not only report these results on the individual methods ACF, APS, and PCF, but we also propagate our inferred values to the consensus measurement (AVG) using the method described in Sec. IV F. Then, the largest bias found for AVG is taken to be the systematic error due to the redshift calibration:

$$\sigma_{z,\text{sys}}^{\text{AVG}} = 0.0035. \qquad (32)$$

In all four cases (ACF, PCF, PCF, AVG), the maximum deviation from $\alpha = 1$ comes from the DNF PDF, which is expected to have an overestimation of the dispersion of the photo z. Hence, this estimation can be considered as an upper limit on the systematic budget. The systematic errors

found here are all below $0.22\sigma_{\text{stat}}$, which if added in quadrature to the statistical error would only increase the total error by 2%.

B. Validation against simulations

One important part of the validation of LSS analyses is to verify in cosmological simulations that we are able to recover the known input cosmology. Here, we use the ICE-COLA mocks described in Sec. III to validate the methodology explained in Sec. IV and to guide different analysis choices.

The tests are summarized in Tables II, III, and IV for ACF, APS, and PCF, respectively.

In the first part of the tables, we vary the number of broadband terms A_i from Eqs. (15)–(17), and we show in **bold** the fiducial results. We find that for ACF results (namely, $\langle\alpha\rangle$ and $\langle\sigma_\alpha\rangle$) stabilize (see below) when using three broadband terms ($i = 0, 1, 2$) to $\langle\alpha\rangle \approx 1.0057$. For APS, we find the result only stabilizes when using as many as five parameters and that we need to include negative broadband terms. This implies that both negative and

TABLE II. BAO fits for the angular correlation function [ACF, $w(\theta)$] on the 1952 ICE-COLA mocks using by default the mocklike setup (see Sec. IV A) with different variations of the analysis in the different rows; see discussion in Sec. V B. The default analysis choice is shown in **bold**. The last two rows also show results in log-normal mocks. We show the mean ($\langle\alpha\rangle$) and standard deviation (σ_{std}) of all best fits, the semiwidth of the intercorrelation region containing 68% of the best fits, σ_{68}, the mean of all the individual error estimations ($\langle\sigma_\alpha\rangle$, from $\Delta\chi^2 = 1$, see Sec. IV E) and, finally, the best fit and its associated error bar σ_α for the fit over the mean of the mocks. Note that for the MICE (default for this table) cosmology, we expect $\bar{\alpha} = 1$, while when using PLANCK cosmology templates, we expect $\bar{\alpha} = 0.9616$.

Case	$\langle\alpha\rangle$	σ_{std}	σ_{68}	$\langle\sigma_\alpha\rangle$	Mean of mocks
$i = 0$	1.0039	0.0187	0.0183	0.0180	1.0043 ± 0.0178
$i = 0, 1$	1.0051	0.0202	0.0200	0.0190	1.0052 ± 0.0188
$i = 0, 1, 2$	**1.0057**	**0.0201**	**0.0202**	**0.0187**	**1.0059 ± 0.0185**
$i = -1, 0, 1, 2$	1.0058	0.0202	0.0200	0.0188	1.0059 ± 0.0185
PLANCK template $i = 0, 1$	0.9675	0.0197	0.0197	0.0205	0.9687 ± 0.0202
PLANCK template **$i = 0, 1, 2$**	0.9680	0.0193	0.0191	0.0182	0.9682 ± 0.0180
PLANCK template $i = -1, 0, 1, 2$	0.9680	0.0195	0.0193	0.0182	0.9680 ± 0.0180
$\Delta\theta = 0.05$ deg	1.0058	0.0202	0.0200	0.0188	1.0061 ± 0.0186
$\Delta\theta = 0.15$ deg	1.0057	0.0202	0.0199	0.0188	1.0061 ± 0.0186
$\theta_{min} = 1$ deg	1.0061	0.0203	0.0200	0.0189	1.0060 ± 0.0186
PLANCK covariance + template	0.9686	0.0194	0.0191	0.0209	0.9689 ± 0.0206
COLA covariance	1.0063	0.0193	0.0187	0.0184	1.0066 ± 0.0181
Lognormal uncontaminated	1.0117	0.0252	0.0230	0.0203	1.0116 ± 0.0201
Lognormal contaminated	1.0119	0.0252	0.0235	0.0205	1.0117 ± 0.0203

TABLE III. BAO fits for the angular power spectrum (APS, C_ℓ) on the 1952 ICE-COLA mocks using by default the mocklike setup with different variations of the analysis in different rows; see discussion in Sec. V B. Similar structure to Table II. The default analysis choices, shown in bold use scale cuts of $\ell_{min} = 10$ and $k_{max} = 0.211$ Mpc^{-1}, corresponding to ℓ_{max} values for each redshift bin of 510, 570, 630, 710, 730, and 770.

Case	$\langle\alpha\rangle$	σ_{std}	σ_{68}	$\langle\sigma_\alpha\rangle$	Mean of mocks
$i = 0$	1.0146	0.0165	0.0158	0.0146	1.0146 ± 0.0145
$i = -2, -1, 0$	1.0068	0.0197	0.0192	0.0180	1.0071 ± 0.0177
$i = 0, 1, 2$	1.0049	0.0191	0.0187	0.0170	1.0052 ± 0.0169
$i = -2, -1, 0, 1$	1.0049	0.0207	0.0197	0.0171	1.0051 ± 0.0167
$i = -1, 0, 1, 2$	1.0064	0.0200	0.0194	0.0178	1.0066 ± 0.0176
$i = -2, -1, 0, 1, 2$	**1.0063**	**0.0216**	**0.0203**	**0.0178**	**1.0061 ± 0.0174**
PLANCK template, $i = 0$	0.9166	0.0230	0.0214	0.0175	0.9183 ± 0.0170
PLANCK template, $i = -2, -1, 0$	0.9555	0.0196	0.0187	0.0167	0.9564 ± 0.0164
PLANCK template, $i = 0, 1, 2$	0.9576	0.0194	0.0188	0.0168	0.9583 ± 0.0165
PLANCK template, $i = -2, -1, 0, 1$	0.9577	0.0223	0.0204	0.0182	0.9580 ± 0.0177
PLANCK temp, $i = -1, 0, 1, 2$	0.9688	0.0197	0.0191	0.0184	0.9690 ± 0.0182
PLANCK template, **$i = -2, -1, 0, 1, 2$**	0.9685	0.0225	0.0201	0.0187	0.9678 ± 0.0182
$\Delta\ell = 10$	1.0062	0.0209	0.0198	0.0175	1.0060 ± 0.0171
$\Delta\ell = 30$	1.0062	0.0239	0.0219	0.0186	1.0059 ± 0.0182
$\ell_{max} = 500$	1.0068	0.0226	0.0218	0.0182	1.0064 ± 0.0178
$\ell_{max} = 550$	1.0069	0.0224	0.0210	0.0181	1.0063 ± 0.0176
$\ell_{max} = 600$	1.0066	0.0218	0.0204	0.0179	1.0062 ± 0.0174
$k_{max} = 0.167$	1.0066	0.0225	0.0206	0.0181	1.0062 ± 0.0176
$k_{max} = 0.255$	1.0058	0.0215	0.0199	0.0178	1.0054 ± 0.0172
COLA covariance	1.0057	0.0215	0.0196	0.0195	1.0061 ± 0.0190
PLANCK covariance + template	0.9689	0.0222	0.0207	0.0215	0.9687 ± 0.0209

TABLE IV.   BAO fits for the projected correlation function (PCF, $\xi_p(s_\perp)$) on the 1952 ICE-COLA mocks using by default the mocklike setup with different variations of the analysis in different rows; see discussion in Sec. V B. Similar structure to Table II.

Case	$\langle\alpha\rangle$	σ_{std}	σ_{68}	$\langle\sigma_\alpha\rangle$	Mean of mocks
$i = 0$	1.0006	0.0176	0.0170	0.0185	1.0010 ± 0.0184
$i = 0, 1$	1.0007	0.0191	0.0182	0.0189	1.0014 ± 0.0188
$i = 0, 1, 2$	**1.0012**	**0.0187**	**0.0180**	**0.0189**	1.0014 ± 0.0192
$i = -1, 0, 1, 2$	1.0014	0.0191	0.0184	0.0193	1.0014 ± 0.0192
PLANCK template $i = 0$	0.9597	0.0163	0.0158	0.0173	0.9610 ± 0.0176
PLANCK template $i = 0, 1$	0.9636	0.0180	0.0176	0.0189	0.9638 ± 0.0188
PLANCK template **$i = 0, 1, 2$**	0.9631	0.0180	0.0176	0.0182	0.9622 ± 0.0184
PLANCK template $i = -1, 0, 1, 2$	0.9632	0.0185	0.0180	0.0186	0.9626 ± 0.0184
$\Delta s_\perp = 10$	1.0011	0.0191	0.0182	0.0189	1.0010 ± 0.0188
$\Delta s_\perp = 8$	1.0014	0.0191	0.0184	0.0190	1.0014 ± 0.0190
$\Delta s_\perp = 3$	1.0015	0.0187	0.0186	0.0189	1.0014 ± 0.0190
$\Delta s_\perp = 2$	1.0016	0.0185	0.0182	0.0189	1.0018 ± 0.0190
Fit range [70,130]	0.9998	0.0204	0.0198	0.0232	1.0014 ± 0.0228
$N_z = 1$	1.0031	0.0214	0.0208	0.0206	1.0026 ± 0.0202
$N_z = 3$	1.0016	0.1929	0.0186	0.0190	1.0018 ± 0.0190
`Planck` Cov + Template	0.9631	0.0177	0.0170	0.0208	0.9622 ± 0.0208
COLA cov	1.0005	0.0192	0.0183	0.0175	1.0010 ± 0.0176

positive powers of ℓ are needed. Then, the results stabilize to $\langle\alpha\rangle \approx 1.0063$. Finally, the results from the PCF do not change much with the number of broadband terms ($\langle\alpha\rangle \approx 1.0012$). In order to judge *stabilization*, we run a larger number of A_i configurations (not all of them shown here) and find that as we keep adding terms, the mean results converge to a given $\langle\alpha\rangle$, with some remaining small variations ($\lesssim 0.1\sigma$). We choose the A_i that has already approximately converged to that value, with the minimal number of terms. We also check that the recovered $\langle\sigma\rangle$ for the selected configuration is similar to other configurations of A_i with similar or equal number of broadband terms.

To help guiding the decision on the number of broadband terms, in the second tier of the tables, we show these variations but now assuming PLANCK cosmology for the template. The importance of the broadband terms is expected to be larger for this case where the template cosmology does not agree with the cosmology of the mocks (MICE) and these terms can absorb part of the differences, making the measurement of the BAO position more robust. For these tests here, we use a hybrid setup with the mocklike covariance and $n(z)$ but with the bias from datalike and PLANCK cosmology. Given the differences in the cosmology of the mocks, at $z_{\text{eff}} = 0.85$, we expect to measure $\alpha = 0.9616$. We see that for the three estimators, the results are already stable (at the level of $\Delta\langle\alpha\rangle < 0.0010$) for the number of broadband terms used as default.

At this point, we note that we find a bias of α that we quantify with $\bar{\Delta}\langle\alpha\rangle \equiv (\langle\alpha\rangle - \bar{\alpha})/\bar{\alpha}$,[7] where we define $\bar{\alpha}$ as

the theoretical expected value: 1 for MICE (default) and 0.9616 for PLANCK. In Tables II, III, and IV (bold values), which is later summarized in Table V, we find $\bar{\Delta}\langle\alpha\rangle = +0.57\%$, $\bar{\Delta}\langle\alpha\rangle = +0.63\%$, and $\bar{\Delta}\langle\alpha\rangle = +0.12\%$ for ACF, APS, and PCF, respectively, in the mocks cosmology (MICE). These biases slightly rise to $\bar{\Delta}\langle\alpha\rangle = 0.67\%, 0.75\% \& 0.16\%$ when assuming PLANCK cosmology. These biases stay at the level of $\Delta\langle\alpha\rangle/\sigma_{\text{std}} \approx 0.3$ for both ACF and APS in MICE cosmology, rising up to $\Delta\langle\alpha\rangle/\sigma_{\text{std}} \approx 0.36$ for PLANCK APS. The latter will be reported as the systematic error coming from the modeling. We now discuss the possible physical origin of these biases and the fact that they are partially mitigated in our fiducial analysis that combines the three measurements.

Nonlinear evolution of the LSS predicts a shift in the BAO position of the order of $\bar{\Delta}\langle\alpha\rangle \sim +0.5\%$ (with respect to the linear case), with the exact value depending on the redshift range, linear bias, and halo occupation distribution of the sample [115,116]. Hence, most of the observed bias in ACF and APS is expected to have a physical origin. Additionally, although not shown in the table, we also try for the ACF to use the alternative COSMOPRIMO[8] template with a different modeling of the BAO damping. COSMOPRIMO has several different ways to compute the no-wiggle power spectrum, but we use the one based on the method developed in [135]. We recover similar results for MICE ($\langle\alpha\rangle = 1.0059$) and PLANCK cases ($\langle\alpha\rangle = 0.9675$). We will also see below (Sec. V C) that when combining ACF, APS, and PCF, the biases in $\langle\alpha\rangle$ get significantly mitigated. Taking into account all of this, we consider our

---

[7]We will use the alternative $\Delta\langle\alpha\rangle$ symbol for differences in $\langle\alpha\rangle$ without renormalizing by $\bar{\alpha}$.

[8]https://github.com/cosmodesi/cosmoprimo.

default analysis to be robust, given the statistical uncertainty of our measurements (see discussion in Sec. V C).

In the third tier of the Tables II, III, and IV, we test variations with respect to our fiducial scale choices, which are given by $\theta_{\min} = 0.5$ deg, $\Delta\theta = 0.20$ deg, and $\theta_{\max} = 0.5$ deg for ACF; $\ell_{\min} = 10$, $k_{\max} = 0.211$ Mpc^{-1}h, and $\Delta\ell = 20$ for APS, and $s_{\perp,\min} = 40$ Mpch^{-1}, $s_{\perp,\max} = 140$ Mpch^{-1}, and $\Delta s_{\perp} = 5$ Mpch^{-1} for PCF. We find all the changes of scale choices to have a negligible impact on the recovered statistics, with the largest deviation ($\Delta\langle\alpha\rangle \sim 0.10\% \sim 0.05\sigma$) found when changing the APS maximum scales. For PCF, we also have the option to have N_z tomographic bins, with $N_z = 6$ being our fiducial option. We find that when using $N_z = 1$ and $N_z = 3$, the $\langle\alpha\rangle$ moves only by $+0.19\% \approx 0.1\sigma$ and $0.04\% \approx 0.02\sigma$, respectively. The driving decision to choose $N_z = 6$ was based on a better agreement between $\langle\sigma_\alpha\rangle$ and σ_{68} an easier comparison to ACF and APS when removing redshift bins, and having a lower expected error (for all their estimations), even when considering the full combination with ACF and APS (AVG in Sec. IV F).

On the fourth tier, we test the change of choice for the covariance. First, we include the *Planck cosmology* entry, which implies using datalike (PLANCK) covariance and datalike bias, together with the PLANCK template, but the $n(z)$ of the mocks. This introduces a negligible shift in the $\langle\alpha\rangle$ ($\sim 0.06\%$). As further validation on the covariance, for the ACF (but not shown in Table II in order to avoid overcrowding the table), we also tested removing the non-Gaussian component of the CosmoLike covariance or switching to the covariance developed in [66], in both cases resulting in negligible changes on the results.

Finally, in this covariance discussion, we also tested the usage of the covariance estimated by the ICE-COLA mocks themselves, having a very small impact on α ($\Delta\langle\alpha\rangle < 0.07\% < 0.05\sigma$). We note again that due to replications in the construction of the mocks (Sec. III), this covariance is not realistic for data, as it introduces spurious correlations on parts of the data vector. However, it will represent the true covariance of the mocks themselves. For this reason, although not shown here, the χ^2/d.o.f. of fits on the mocks gets close to unity for this covariance but differs from our default CosmoLike covariance. As expressed in our previous paragraph and in Sec. IV D, we remark that this covariance has been validated against other model covariances and mock estimates from FLASK lognormal simulations. Unfortunately, these differences between the ICE-COLA mocks inherent covariance and our fiducial covariance, and their impact on the χ^2 tell us that we cannot consider the calibration of the absolute χ^2 given by our pipeline as validated. Hence, we will not use absolute χ^2 as a driving criteria on the data, although we may consider variations of χ^2 when changing analysis choices. Regarding our

usage of $\Delta\chi^2 = 1$ as our 1-σ definition, we validate it below against the dispersion in the measurements of α.

Up to this point, we have not commented much on the results for the different estimations of the error σ, which are somewhat heterogeneous. Nevertheless, all the estimators of σ, for the three BAO measurements (ACF, APS, PCF) give us errors of the order $\sigma \sim (2.0 \pm 0.2)\%$. For the fiducial choice of ACF, we find that the estimated error σ_α (from $\Delta\chi^2 = 1$) is 7% below the scatter observed in the distribution of best fit α, when estimated with the standard deviation (σ_{std}) or the interpercentile region (σ_{68}). For the APS, this difference rises to 18% or 12%, respectively, whereas for the PCF, the differences in error estimation stay below $\sim 4\%$ (and switch sign). Those percentages stay similar when moving to the PLANCK template. For the ACF (the most validated method), these differences reduce to below 5% when using the COLA covariance. Finally, for the datalike covariance ("PLANCK Cov + Templ") σ_α switches to an overestimation of the scatter of 7–9%.

As we will see in the next subsection, once we combine the three statistics, not only the biases in the mean are mitigated, but also the difference among different σ.

Finally, only for ACF, we also did some tests on the lognormal mock catalogs used to study observational systematics. The main feature here is that we can include the imprint of the observational systematics on them (an earlier version of the weights summarized in Sec. II D, see also [50]). We show the results on these mocks in the last tier of Table II, and by comparing the results on the uncontaminated mocks to the contaminated ones, we find that the results are unchanged for the BAO when we add these observational systematics. This shows the exceptional robustness of BAO to these effects.

C. Validation of combination

In this section, we study how the method described in Sec. IV F to combine three correlated statistics performs when combining our three analyses on the ICE-COLA mocks. For that, we start by measuring covariance of the best fits of ACF, APS, and ACF from the mocks. For that, we first eliminate the 11 mocks in which at least one of the three methods finds a nondetection. Then, this covariance is decomposed into the variance of the three measurements and the correlation coefficient across measurements. The variance is simply the square of the σ_{std}, which we now summarize in Table V for PLANCK and MICE cosmologies (there are some slight differences in the last digit with respect to Tables II–IV due to removing the correlation between ACF and APS is $\rho_3 = 0.863$; between ACF and PCF, $\rho_2 = 0.905$; and between APS and PCF, $\rho_1 = 0.789$). These correlations are slightly lower than those found in spectroscopic surveys. For example, we have $\rho_{\text{ACF,APS}} = 0.863$, whereas the eBOSS LRG in BAO measurements in configuration [68] and Fourier space [69] have a correlation of 90% [136]. We note that, although we

are using the same data, we expect part of the noise to be decorrelated. We believe that the decorrelation can increase when projecting r/k onto $\theta/\ell/s_\perp$ and also when making different analysis choices such us the different number of broadband terms.

One curiosity is that in previous analyses (Y1, Y3) APS and APS were found more correlated among themselves than to the PCF. In Y6, this pairing is broken, and the ACF is found more correlated to the PCF than to the APS. The main driver for the increase of the correlation is the fact that in Y6 we are analyzing the PCF in $N_z = 6$, $\Delta z_{ph} = 0.1$ tomographic bins like the ACF, whereas in previous analyses the PCF was considering the entire redshift range altogether ($N_z = 1$), making PCF and ACF less correlated. One of the reasons why we used $N_z = 6$ is that the error in the PCF was smaller than using $N_z = 1$. One could wonder if the information gained by using $N_z = 6$ is somehow lost by the fact that it is more correlated with ACF. Following the same methodology presented here, we checked that the combined ACF + PCF error on α is still smaller for $N_z = 6$ than for $N_z = 1$.

Once we have the covariance between ACF, APS & PCF, we combine them using Eq. (27) to (31). In Eq. (31), the error that we propagate is the individual error σ_α estimated from $\Delta\chi^2 = 1$, as we plan to use the same method on the data, where we cannot use ensemble estimates. As a result, we obtain a new combined best fit α_{AVG} and a new estimated error $\sigma_{\alpha_{AVG}}$ for each mock. With this, we can again estimate the mean ($\langle\alpha\rangle$) and standard deviation (σ_{std}) of the best fits α_{AVG}, the 68 interpercentile region (σ_{68}) and the mean estimated error ($\langle\sigma_{\alpha_{AVG}}\rangle$).

All these summary statistics are shown in the fourth row (AVG) of each section of Table V. We find that the AVG statistics have a small bias in $\langle\alpha\rangle$: $\bar\Delta\langle\alpha\rangle = 0.19\%$ for MICE cosmology and $\bar\Delta\langle\alpha\rangle = 0.23\%$ for the PLANCK cosmology.

The larger one will be considered our systematic error from the modeling side in Sec. VII (Table VIII):

$$\sigma_{th,sys}^{AVG} = 0.0023. \tag{33}$$

This is at the level of $0.15\sigma_{stat}$ (considering the error expected from the mocks) and, if added in quadrature, would only increase the total error budget by 1%.

Concerning error bars, we find them to be very well behaved: Our mean estimated uncertainty gives us $\langle\sigma_{\alpha_{AVG}}\rangle = 0.0181$ (1.81%), which agrees to better than 3% with the scatter measured on the best fit α's on MICE cosmology. For PLANCK cosmology, we obtain an estimated uncertainty of $\langle\sigma_{\alpha_{AVG}}\rangle = 0.0175$ (1.83%), which agrees with the measured scatter to better than 2%. When using the cosmology of the mocks (MICE), the pull distribution (see definition in Table V) also shows excellent agreement with Gaussianity to the 1% level ($\langle d_n\rangle = 0.01$), and the fraction of mocks enclosed in $[\langle\alpha\rangle - \langle\sigma_\alpha\rangle, \langle\alpha\rangle + \langle\sigma_\alpha\rangle]$ matches the Gaussian case exactly to the third significant figure (68.6%). When assuming PLANCK cosmology, the degradation of these two measures of Gaussianity is still very small. Indeed, by combining different signals, we do expect that the resulting estimates become more Gaussian. Additionally, we also expect that different methods can be affected by small different theoretical errors and that the combination of them would give more robust results.

VI. PRE-UNBLINDING TESTS ON DATA

Before we start looking at the clustering results on the data, we have performed a thorough validation based on theory [with different $n(z)$ calibrations, Sec. V A] and on mock catalogs (Secs. V B and V C). Once we decide to move on to tests on the data, in order to avoid confirmation bias, the analysis is performed blinded to the cosmological

TABLE V. Summary of fiducial analyses for individual estimators (ACF, APS, PCF) and their combination (AVG) for 1941 out of 1952 mocks that show a detection in the three estimators. We show the results for the MICE cosmology (where $\alpha = 1$ is expected as this is the cosmology of the mocks) and for the PLANCK template [where $\alpha = 0.9616$ is expected from the theoretical perspective, Eq. (24)]. We show the mean ($\langle\alpha\rangle$) and standard deviation (σ_{std}) of all best fits, the semiwidth of the interpercentile region containing 68% of the best fits (σ_{68}), the mean of all the individual error estimations ($\langle\sigma_\alpha\rangle$, from $\Delta\chi^2 = 1$, see Sec. IV E), and we also include the fraction of mocks with the best fit α enclosed in $\langle\alpha\rangle \pm \langle\sigma_\alpha\rangle$ and the mean ($\langle d_n\rangle$) and standard deviation (σ_{d_n}) of the pull statistics ($d_n = (\alpha - \langle\alpha\rangle)/\sigma_\alpha$).

Case	Method	$\langle\alpha\rangle$	σ_{std}	σ_{68}	$\langle\sigma_\alpha\rangle$	Mocks $\in \langle\alpha\rangle \pm \langle\sigma_\alpha\rangle$ (%)	$\langle d_n\rangle$	σ_{d_n}
MICE	ACF	1.0057	0.0202	0.0202	0.0187	65.2	-0.0086	1.0730
	APS	1.0063	0.0216	0.0204	0.0178	62.3	-0.0168	1.2208
	PCF	1.0012	0.0187	0.0182	0.0189	69.6	-0.0084	0.9819
	AVG	1.0019	0.0185	0.0180	0.0181	68.6	-0.0100	1.0189
PLANCK	ACF	0.9680	0.0193	0.0191	0.0181	65.3	-0.0106	1.0665
	APS	0.9685	0.0225	0.0203	0.0187	64.5	-0.0364	1.1805
	PCF	0.9631	0.0180	0.0176	0.0182	69.5	-0.0095	0.9827
	AVG	0.9638	0.0180	0.0177	0.0175	67.6	-0.0137	1.0215

information. In this case, this means that we are not allowed to see the value of the BAO shift α measured in the data. For that reason, most of the tests proposed here are carried out with scripts that only look at the differences in α between two analyses and not at α itself. When this is not possible, we blind α by shifting each best fit by the same unknown amount ($\Delta\alpha \in [-0.2, 0.2]$) with a common script and the same random seed for the three analyses. The error values σ_α are also blinded such that the only information accessible are relative changes in σ_α between two analysis setups (typically, the fiducial analysis and a variation of it). This is achieved by having the errors of each estimator (ACF, APS, PCF) rescaled by a factor such that they are equal to the mean error seen in the mocks for the fiducial case.

We also blind all the clustering measurements, except for the $0.5 < \theta < 1$ deg scales of the ACF that were used to calibrate the mocks. At a later stage, when the sample, weights, and redshift validation were finalized, we also allowed the fit to the galaxy bias to take a slightly larger range, $0.5 < \theta < 2$ deg. These bias values were then used to build the final version of the datalike covariance matrices.

A. Pre-unblinding tests on ACF, APS, and PCF

Before finalizing our analysis pipeline, we perform a series of blinded tests, detailed below. The general guiding criterion is that if something that happens on the data also occurs in 90–95% or more of the mocks, we consider the test fully passed. Some mild revision is envisioned if some particularity on the data is found to happen in less than 5–10% of the mocks. If it happens in less than 1% of the mocks, we will regard the test as failed and consider a major revision of the methodology before continuing with our analysis and the unblinding of the results.

Unless otherwise stated, we will be using the datalike setup for the data and the mocklike setup for the mocks (see Sec. IV A).

(1) *Is the BAO detected?* This test is summarized in Table VI.

In the ICE-COLA mocks, we have detections (i.e., $\alpha \pm \sigma_\alpha \in [0.8, 1.2]$; see Sec. IV E) in $>99\%$ of the cases for the full dataset with any of the three estimators: ACF, PCF, APS. Therefore, we should strongly expect a detection in the data.

Additionally, for most cases, we expect to have detections in most individual redshift tomographic bins. Based on Table VI, for ACF and PCF we impose as a pre-unblinding criterion that we would envision a major revision if there are three bins or more nondetections ($\lesssim 0.5\%$), a mild revision for two nondetections ($\sim 4\%$), and we would consider the test passed for zero or one nondetections ($\sim 95\%$). For APS, we would consider a major revision for four or more nondetections ($\lesssim 1\%$),

TABLE VI. Pre-unblinding test 1: Detection rate of BAO. We show the BAO detection rate in the ICE-COLA mocks for the angular correlation function (ACF), angular power spectrum (APS), and the projected correlation function (PCF). The first row represents the results for all the tomographic bins combined, whereas the following six rows show results for individual bins. In brackets, we show whether [Y] or not [N] there is a detection on the data. On the second part of the table, we show the percentage of mocks that have zero, one, two, three or four tomographic bins with non-detections. Here, we mark in **bold** where the data fall.

Bin	ACF	APS	PCF
All	99.95% [Y]	99.49% [Y]	100% [Y]
1	90.32% [N]	74.49% [N]	95.39% [N]
2	94.98% [Y]	82.12% [Y]	97.34% [Y]
3	97.39% [Y]	86.73% [Y]	97.69% [Y]
4	97.59% [Y]	91.55% [Y]	97.84% [Y]
5	96.67% [Y]	90.73% [Y]	95.39% [Y]
6	91.19% [Y]	87.76% [Y]	86.22% [Y]
Nondetections			
0	72.90%	41.80%	73.77%
1	**22.85%**	**36.42%**	**22.69%**
2	3.84%	16.03%	3.23%
3	0.31%	4.82%	0.26%
4	0.10%	0.92%	0.05%

mild for three ($\sim 5\%$), and a pass for zero to two nondetections.

Results:

(a) We find a detection in ACF, PCF, and APS when we use the full dataset (All), thus passing the first part of the test.

(b) When looking at individual tomographic bins for ACF, APS & PCF, we find one nondetection (in the first bin in all cases), hence passing this test. We notice that the nondetection in the first bin has been consistent across all DES BAO analyses, and it is considered a statistical fluke due to cosmic variance.

A natural question that arises here is whether it is worth removing the first bin from the dataset once we know we do not find a detection (under our definition). We investigate this further in Appendix D, without drawing strong conclusions in either direction. Since our method has been validated in Sec. V based on the full dataset (six bins), and for consistency with the adoption in Y1 and Y3 analyses, we proceed with the entire dataset.

(2) *Is the measurement robust?* These sets of tests are summarized in Figs. 4 and 5 (now shown unblinded) and tabulated in Appendix E. We test how much the best fit α changes when we modify some choice in the analysis and quantify it with $\Delta\alpha$. Similarly to the rest of the pre-unblinding tests, we assess the
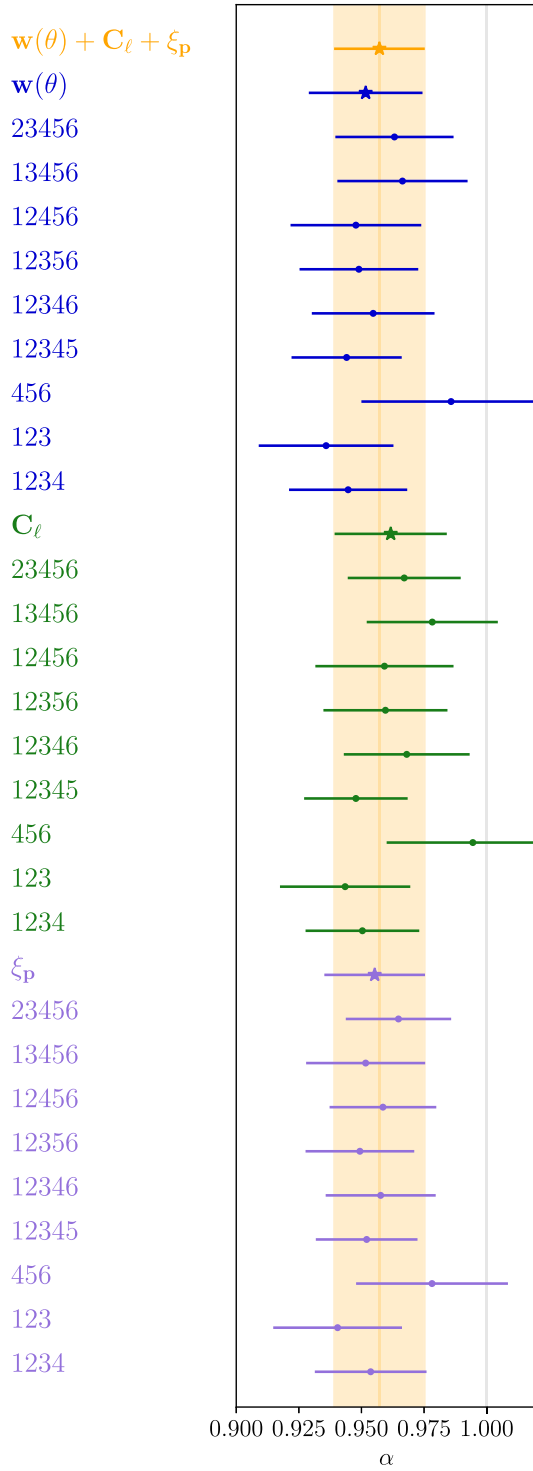
FIG. 4. Unblinded representation of the pre-unblinding tests regarding partial data removal. We show the fiducial AVG BAO measurement from Sec. VII with an orange star and a shaded area. For each of the individual estimators, ACF [$w(\theta)$], APS (C_ℓ), and PCF (ξ_p), we show the fiducial result and how much it changes when we only keep some z bins (indicated by the numbers). More details in Sec. VI.
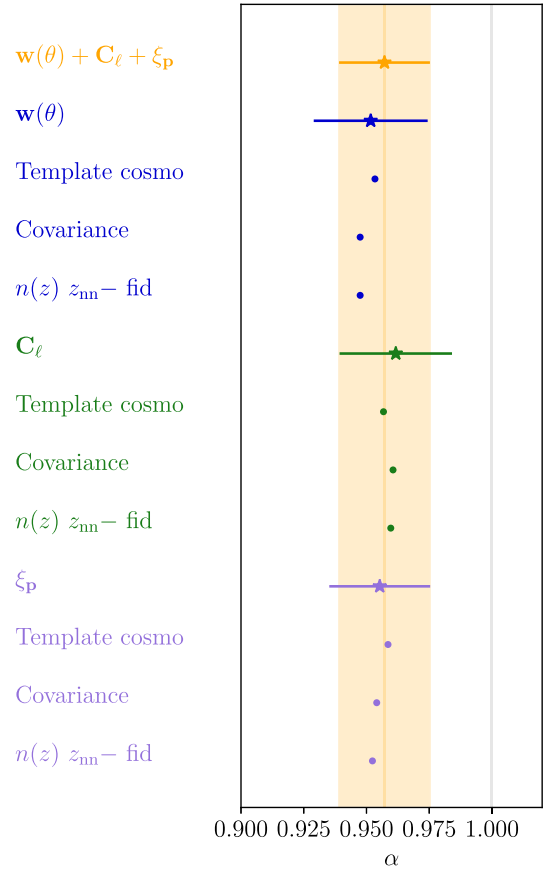

FIG. 5. Unblinded representation of some pre-unblinding tests regarding robustness. Main combined BAO measurement [AVG or $w(\theta) + C_\ell + \xi_p$] from Sec. VII shown with an orange star and a shaded area. For each of the individual estimators, ACF ($w(\theta)$), APS (C_ℓ), and PCF (ξ_p), we show the fiducial result (with a star) and how much the best fit α changes when we change the assumed cosmology in the template, the covariance, or the $n(z)$ estimation. We also show a vertical gray line for the PLANCK BAO prediction ($\alpha = 1$). The tests presented here are part of a series of pre-unblinding tests tabulated in Appendix E and discussed in Sec. VI.

significance of the shifts in α by comparing to the distribution in the mocks. While Figs. 4 and 5 show the results of this test on the data after unblinding (using the *datalike* setup), the information we used pre-unblinding tests is shown is Tables XII–XIV. There, we show for each test the limits of the $\Delta\alpha$ intervals containing 90%, 95%, 97%, and 99% of the mocks. We consider an individual test failure if the $\Delta\alpha$ falls outside one of these intervals.

Given that we are performing a large number of tests, we expect that some of them could fail individually, without posing a global challenge. We quantify this with the same guiding criteria we stated at the beginning of the section: mild

revision if 5–10% of the mocks show similar levels of failure, major revision if only $\sim < 1\%$ do.

(a) *Impact of removing one tomographic bin.* In Fig. 4, we show the change in best fit α and σ_α when removing one tomographic bin at a time. These shifts are compared to the equivalent distribution in the COLA mocks in Appendix E. The quantity being measured on both the mocks and data is $\Delta\alpha = \alpha_{5\text{-bins}} - \alpha_{6\text{-bins}}$. While we do not set strict pre-unblinding criteria on the σ_α values, we regard any significant changes as informative.

(b) *High-z vs low-z.* In Fig. 4, we also check the consistency of the results when only keeping the high-redshift half of the data (bins 456), only keeping the low-redshift half (bins 123) or removing the last two bins (bins 1234). The aim of this redshift split is to assess the consistency between different parts of the data, in particular, by checking if the high-z data, for which the control of the observational systematics and the redshift validation is more challenging, could be dragging the results in one particular direction.

(c) *Impact of template cosmology.* Here, we test whether the results vary as expected when changing the assumed cosmology in the template. For the mocks, we compute a new α based on the datalike PLANCK cosmology template and compare it to the default mocklike setup. For the data, we change the template from datalike to data-like-mice setup, while we keep the covariance unchanged. Then, our test is given by the variable $\Delta\alpha = \alpha_{\text{Planck}} - \alpha_{\text{MICE}} + 0.0384$, taking into account the 0.0384 difference expected by the change of cosmology. The best fit α values on the data are shown in Fig. 5 for each estimator, while the results for the mocks are tabulated in Appendix E.

   We note that taking into account the biases ($\langle\alpha\rangle - 1$) found in Tables II–IV, which differ from PLANCK and MICE cosmologies, we do not expect $\Delta\alpha$ to be centered at 0, but at -0.0007, -0.0009, -0.0003, respectively.

(d) *Impact of changing covariance.* We check the difference when changing from our datalike covariance (PLANCK cosmology and fiducial datasetup) to the mocklike covariance (MICE cosmology and properties from the mocks; see Sec. IV A) or vice versa. We define this test with $\Delta\alpha = \alpha_{\text{mock,cov}} - \alpha_{\text{data,cov}}$, noticing that, for the mocks, the fiducial choice is $\alpha_{\text{mock,cov}}$, whereas for the data, the fiducial choice is $\alpha_{\text{data,cov}}$. We show the corresponding α values for the data in Fig. 5, while the results for the mocks are tabulated in Appendix E.

(e) *Impact of n(z) estimation.* Similarly, we now assess the impact of changing the assumed redshift distribution in the template from the data fiducial choice to $n(z)$ estimated from DNF z_{nn}: $\Delta\alpha = \alpha_{\text{znn}} - \alpha_{\text{fid}}$. Again, the fiducial choice of the mocks appears on the left (α_{znn}), whereas the fiducial choice on the data is on the right side of the difference. In this test, the covariance is left unchanged. We show the best fit α values for the data in Fig. 5, while the results for the mocks are tabulated in Appendix E.

   Results:

(a) For ACF, the data does not fail any tests. This happens in 47% of the mocks. Hence, we consider the robustness tests to be passed.

(b) For APS, the data fails 1 test (removing bin 2) at the 90% level (see Table XIII). 50% of the mocks fail at least one of the tests at the 90% level, and 21% of the mocks fail exactly one test. Thus, we consider the robustness tests passed.

(c) For the PCF, the data does not fail any tests. On the mock catalogs, we find that 45% of the mocks do not fail any of these tests. Thus, we consider the tests passed.

   We find another particular feature when looking at the impact of removing bin 6 on the error. The error becomes smaller when removing this bin for the ACF (failing this test at the 97% level, see Table XII) and APS (failing at 90%, see Table XIII), whereas for PCF, the error does not become smaller. This led us to investigate this a bit further. First, we checked that 17% of the mocks fail one or more $\Delta\sigma$ tests at the 97% level for ACF. Second, typically $\sim 10\%$ of the mocks show a smaller error when one particular redshift bin is removed. This is investigated further in Appendix C, where we check how the estimated error σ_α behaves in those particular cases. We find that the σ_α from the full set of six bins is a better representation of the best fit α scatter compared to when using the σ_α estimated from the first five bins. Said otherwise, the σ_α from the first five bins becomes smaller, but just because it underestimates the underlying scatter, not because α is better determined.

   In light of those results, we decided to continue with the full six-bin case. Nevertheless, we will also report the results from bins 1–5, bearing in mind that the last bin might be more prone to observational systematics.

Incidentally, although not listed in the tables from Appendix E, at some later stage but prior to unblinding, we realized that the difference between the α values preferred by 123 and by 456 is somewhat large compared to the error bars (see Fig. 4). This difference is highly correlated with the high- and low-redshift split tests discussed above [123 vs 456 in Fig. 4, corresponding to entries 7 (456) and 8 (123) in Tables XII–XIV]. Nevertheless, we measured $|\alpha_{123} - \alpha_{456}|$ on the mocks, finding that 18%, 19%, and 27% of the mocks have a more extreme value than what is found in the data for ACF, APS, and PCF, respectively.

At that stage, we also compared the (blinded) α preferred by individual bins (blinded version of Fig. 11 below), finding for ACF and APS a somewhat large difference between bin 6 and bin 2. However, we checked that the difference between the largest and lowest individual α found in mocks is compatible with what we see in the data for bin 2 and 6: For the case of ACF, 24% of the mocks show a more extreme case, whereas for APS, this rises to 43%.

(3) *Is it a likely draw?* Here, we consider whether the ensemble of the 12 tests discussed above, each with a $\Delta\alpha$ (and shown in the top half of Tables XII–XIV), is within expectations. For that, we measure the covariance of the 12 $\Delta\alpha$ on the mocks. We then compute the χ^2 from this covariance and the $\Delta\alpha$ array in the data and compare it to the χ^2 distribution seen in the 1952 mocks.

Results:

(a) ACF: The maximum values of the $\Delta\alpha$-based χ^2 that contain 90% and 95% of the mocks are 26.16 and 37.78, respectively. For the PLANCK data, we get a χ^2 value of 18.01, which is well below these limits.

(b) APS: On mocks 90% and 95%, have $\chi^2 < 28.42$, $\chi^2 < 42.22$. We find on the data that the $\Delta\alpha$-based χ^2 is 11.22, well within those limits.

(c) PCF: The maximum $\Delta\alpha$-based χ^2 that contains 90% and 95% of the mocks are 22.99 and 31.31, respectively. For the data, we get a χ^2 value of 6.50, which is well within the interval.

Finally, we also check the goodness of fit for the clustering statistics, although we do not put any specific criterion on it. The reason is that the χ^2 could not be validated against the ICE-COLA mocks, due to their spurious covariance, as discussed in Sec. V B. We still expect the χ^2/d.o.f. to be of order unity.

For the case of ACF, we find χ^2/d.o.f. $= 84.5/107$ (datalike setup), similar to what we find in the mocks (76.3/107 for mocklike setup). For reference, 22.64% of the mocks have a larger χ^2 than that of the data. For APS,

we find χ^2/d.o.f. $= 163.3/156 = 1.05$, well within the $\chi^2 < 229.16$ limit found for 95% of the mocks. For PCF, the χ^2/d.o.f. $= 39.8/95 = 0.42$, similar to the mean values found in the mocks (37.1/95 for MICE, 35.9/95 for PLANCK). As explained before, the χ^2 is not considered an unblinding criterion as it could not be validated on the ICE-COLA mocks. Additionally, for PCF, we have the added difficulty that the covariance matrix needs some *ad hoc* treatment discussed in [73], where the χ^2/d.o.f. does not reach unity.

At this point, we also remark that even though, in the mocks, the χ^2/d.o.f. does not approach unity, the errors derived from it are very consistent with the scatter found in the best fit α (see, e.g., Table V). Hence, we find that the σ_α reported are robust. We also note that if we considered the χ^2 correct for ACF and PCF, this would hint at an overestimation of the uncertainties, hence, if anything, lying on the conservative side. On the other hand, APS has χ^2/d.o.f. very close to unity.

B. Pre-unblinding tests for combination

Once we have validated the individual measurements by ACF, APS, and PCF, we need to check the compatibility among those measurements before proceeding to their combination. For that, first, we check the difference between different estimators and compare it with the mocks. This is performed in the first part of Table VII. For example, the first entry shows the difference in the best fit between the ACF and APS, $\alpha_{ACF} - \alpha_{APS}$, together with the limits expected from the mocks 90% interquantile regions. In this case, we would look a bit more carefully at the combinations if the data falls outside the 90% bulk of the mocks (and would have pursued strong scrutiny if they fall outside the 99% range).

Once that test is concluded, we can look at the difference between one individual estimator and the combination of

TABLE VII. Pre-unblinding tests for the combination of the three estimators: ACF, APS, PCF. We take two different estimators (labeled in the first column) of the BAO shift, α, and measure their difference ($\Delta\alpha$) on the data (second column). We then compare with the symmetric interquantile region that contains 90% of the mocks (third column).

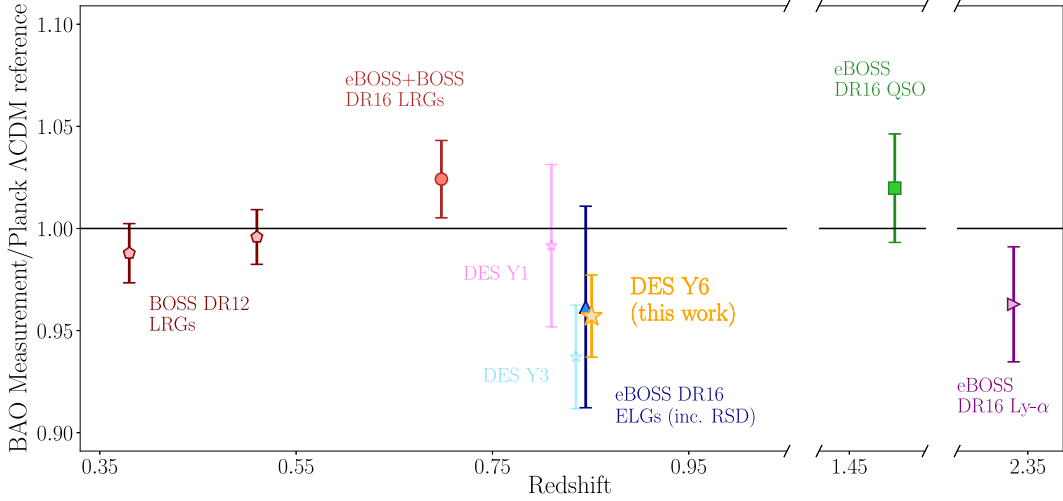| $\Delta\alpha \times 100$	Data	90%-mocks
ACF-APS	−1.00	[−1.36, 1.12]
ACF-PCF	−0.36	[−0.58, 1.51]
APS-PCF	0.64	[−1.04, 2.15]
ACF-{APS + PCF}	−0.48	[−0.52, 1.24]
APS-{ACF + PCF}	0.68	[−1.02, 2.02]
PCF-{ACF + APS}	0.10	[−1.58, 0.61]
AVG-ACF	0.54	[−1.34, 0.58]
AVG-APS	−0.45	[−1.78, 0.81]
AVG-PCF	0.19	[−0.23, 0.39]

FIG. 6. Ratio between the $D_M(z)/r_d$ measured using the BAO feature at different redshifts for several galaxy surveys and the prediction from the cosmological parameters determined by PLANCK, assuming ΛCDM. We include a series of measurements by SDSS, and also the DES Y1 and Y3 results. The DES Y6 measurement is shown with an orange star. This represents the most updated angular BAO distance ladder at the closure of stage III.

the other two (part two of Table VII) or the difference between the combination of the three (AVG) and an individual measurement (third part of Table VII). The details on how these combinations are performed are in Secs. IV F and V C. Again, by running such a large number of tests, we are likely to statistically fail some of the tests. In that case, we would consider the ensemble of the tests.

One feature of the intervals reported in Table VII is that they are not always symmetric around zero. This is already expected, since the different estimators give slightly different $\langle \alpha \rangle$ (Table V).

Results:

We find compatibility among APS, ACF, and APS, and among all the combinations tested: All the data points shown in Table VII fall well within the 90% intervals measured in the ICE-COLA mocks. Hence, not only the individual (ACF, APS, PCF) measurements are ready for unblinding, but also our consensus combined BAO measurement (AVG).

VII. RESULTS

Once the pre-unblinded tests presented in the previous section were passed, we entered a gradual unblinding phase. The checklist to unblind is described in Appendix A and highlights the level of scrutiny that we put into this analysis before we allowed ourselves to know the consequences for cosmology. This is likely the strongest blinding policy to date imposed on a BAO analysis.

At the end of this phase, we obtained our unblinded fiducial results, described below (Sec. VII A) and also their corresponding different variations when some choices in our analysis are changed. These are referred to as robustness tests and are described in Sec. VII C.

A. Main results

After unblinding, we find $\alpha = 0.9517 \pm 0.0227$, $\alpha = 0.9617 \pm 0.0224$, and $\alpha = 0.9553 \pm 0.0201$, for ACF, APS, and PCF, respectively. Then, applying Eqs. (27) and (31), our consensus combined measurement (AVG) is

$$\alpha = 0.9571 \pm 0.0196[\text{stat}],$$
$$\pm 0.0041[\text{sys}],$$
$$\alpha = 0.9571 \pm 0.0201[\text{tot}]. \qquad (34)$$

We report first the purely statistical error ([computing the $\Delta\chi^2 = 1$ criterion in ACF, APS, and PCF and then combining them to AVG with Eq. (31)], then the systematic error [adding in quadrature the AVG systematics from Eqs. (32) and (33)], and finally the total error by adding in quadrature the former two. When reporting only two significant figures on the error (as done in the abstract), the total uncertainty is indistinguishable from the statistical one.

We remind the reader that, for our default analysis, we assume the PLANCK cosmology as fiducial (see datalike in Sec. IV A). This implies that

$$D_M(z = 0.85)/r_d = 19.51 \pm 0.41[\text{tot}]. \qquad (35)$$

This result represents a 2.1% precision measurement at $z_{\text{eff}} \sim 0.85$ of the angular BAO. In Fig. 6, we show the value of D_M/r_d divided by PLANCK's prediction for our Y6 measurement compared to the series of SDSS BAO measurements and also including the ones from the DES Y1 [75] and Y3 BAO [76] analyses. For SDSS, we include the combined BOSS LOWz + CMASS galaxy samples (at $0.2 < z < 0.5$ and $0.4 < z < 0.6$) [38], the eBOSS luminous red galaxies (LRG, $0.6 < z < 1.0$) [85,86] and

emission line galaxies (ELG, $0.6 < z < 1.1$) [87,88], as well as the eBOSS quasars ($0.8 < z < 2.2$) [71,89] and the Lyman-α combination of autocorrelation and cross-correlation with quasars ($z > 2.1$) [90].

Figure 6 represents the state-of-the-art at the closure of stage-III galaxy surveys for angular BAO measurements. It shows that our measurement is competitive with spectroscopic surveys that were designed for BAO science, with the caveat that those surveys also report competitive results from radial BAO and redshift space distortions from anisotropic galaxy clustering. In terms of relative uncertainty, our measurement is the most precise angular BAO measurement from a photometric survey at any redshift and also the most precise one from any type of galaxy survey at $z_{\text{eff}} > 0.75$. Our 2.1% measurement of D_M/r_d at $z_{\text{eff}} = 0.85$ more than doubles the precision of the constraint from eBOSS ELGs at a similar redshift (5.1% at $z_{\text{eff}} = 0.85$). It also exceeds the relative precision of higher redshift measurement from quasar clustering (2.6% at $z_{\text{eff}} = 1.48$) and Lyman-α forests (2.9% at $z_{\text{eff}} = 2.33$). The eBOSS LRG measurement gives a more precise measurement, $\alpha = 1.024 \pm 0.019$ ($\sim$1.9%), at a lower redshift, $z_{\text{eff}} = 0.70$, whereas the BOSS measurements are the most precise ones: 1.5% at $z_{\text{eff}} = 0.38$ and 1.3% at $z_{\text{eff}} = 0.51$. Next generation spectroscopic surveys such as DESI and Euclid are expected to improve upon these constraints.

All of those measurements report angular distance constraints from post-reconstruction BAO-only fits except for eBOSS ELGs. This case only reports the isotropic BAO (D_V) from post-reconstruction, which combines information from the angular (D_M) and Hubble distances [$D_H = c/H(z)$] together: $D_V = (zD_M^2 D_H)^{1/3}$. In order to compare the purely angular constraints, we chose to show in Fig. 6 the constraints on D_M coming from a combination of BAO and redshift space distortions [71,89], $\alpha = 0.962 \pm 0.049$. Alternatively, one could pick the isotropic measurement, $\alpha_{\text{iso}} = 0.986 \pm 0.032$ at $z_{\text{eff}} = 0.85$ (3.3% precision) [70,71] and increase the error bar by $\times 1.5$ (4.9%), taking into account that 2/3 of the isotropic information comes from the angular BAO. The ELG measurement including RSD agrees in central value with our measurements, as shown in Fig. 6. The isotropic constraint prefers a slightly higher value, but that shift is below half of the sigma reported by eBOSS ELGs. Other measurements of the BAO in $0.70 < z_{\text{eff}} < 1.0$ tend to agree with the PLANCK predictions, but with larger uncertainties, a summary of these can be found in Fig. 17 of [70].

B. The BAO signal

In Fig. 7, we report the $\Delta\chi^2$ as a function of the BAO shift α for each of the three individual measurements (ACF, APS, and PCF). Although not shown, we compared these χ^2 distribution to the assumptions of a Gaussian likelihood, finding good agreement to $\sim$2–3σ. As hinted in the mock tests, the APS likelihood is found to be less Gaussian than
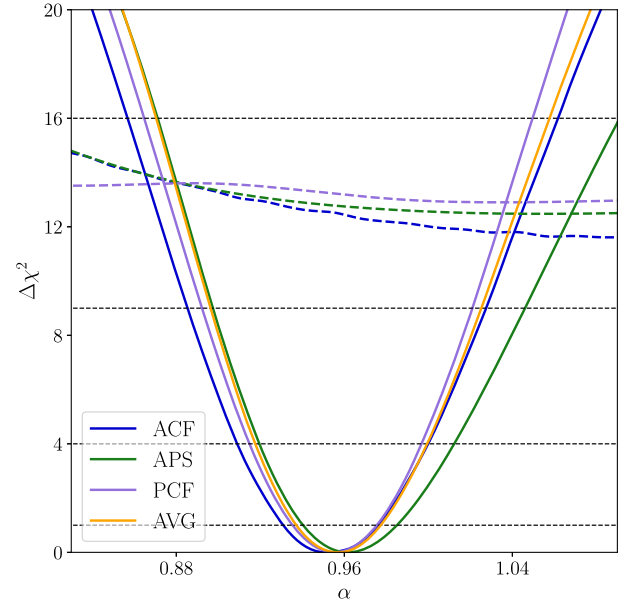

FIG. 7. $\Delta\chi^2$ profile for the different estimators (ACF in blue, APS in green, and PCF in purple). In colored dashed lines, we show the $\Delta\chi^2$ obtained when trying to fit the data with a template without BAO. The combined $\Delta\chi^2$ profile (AVG, in orange) is the mean of the three $\Delta\chi^2(\alpha)$ curves but shifted and tightened so that its best fit and its width match our consensus measurement reported in Eq. (34) (for the total error). The 1, 2, 3, and 4σ limits are shown as horizontal black dashed black lines.

the ones for ACF or PCF. For our consensus AVG error, we need to assume a Gaussian likelihood (implicitly assumed throughout Sec. IV F). As an alternative, we compute the mean of the three $\Delta\chi^2$. This curve is then shifted and tightened to match the best fit α value and 1-σ error reported in Eq. (34), as shown by the orange curve. The four versions of the likelihood will be publicly released; see URL in Sec. VIII. In colored dashed lines, we also show the $\Delta\chi^2$ obtained when trying to fit the data with a template without BAO. By comparing the curves with and without BAO, we can see a difference in χ^2 of $\sim$12, which implies a detection of the BAO signal at the $\sim$3.5σ level.

The best fit models are compared to the clustering measurements in Figs. 8–10 for ACF, APS, and PCF, respectively. In order to highlight the BAO feature, we subtract the no-BAO template. In the case of PCF, we also show the $N_z = 1$ case in which all the BAO signal is concentrated into a single redshift bin, in order to visualize better the BAO feature. This is only possible for this statistic, where the BAO signal is expected to align in the $s_\perp$ coordinate. Nevertheless, $N_z = 1$ is not used for our fiducial results of PCF, which rely on using six redshift bins ($N_z = 6$) like the ACF and APS cases. The raw clustering statistics can be found in the companion paper ([50], Fig. 7).

We note again that the fiducial fit is performed over all six redshift bins simultaneously with one single BAO shift α. Hence, not all the tomographic bins are necessarily fitted
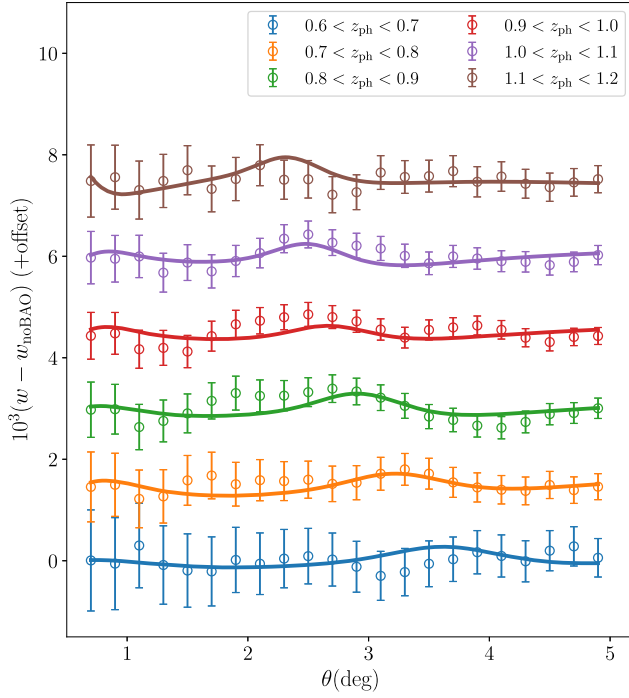
FIG. 8. The isolated BAO feature, measured in configuration space using the angular correlation function, or $w(\theta)$. The curves have been rescaled by a factor of 10^3 and vertical offsets of $+1.5$ have been sequentially added to each tomographic bin, having our bin 1 (lowest redshift) at the bottom, and bin 6 at the top. Measurements are shown as markers with error bars (derived following Sec. IV D and PLANCK cosmology), while the best fit model (with a single BAO shift α for the six z bins) is shown in solid lines. The BAO feature moves to lower angular scales as the redshift increases, reflecting its constant comoving size. Raw clustering measurements (without BAO template subtraction) of ACF, APS, and PCF can be found in the companion paper [50].
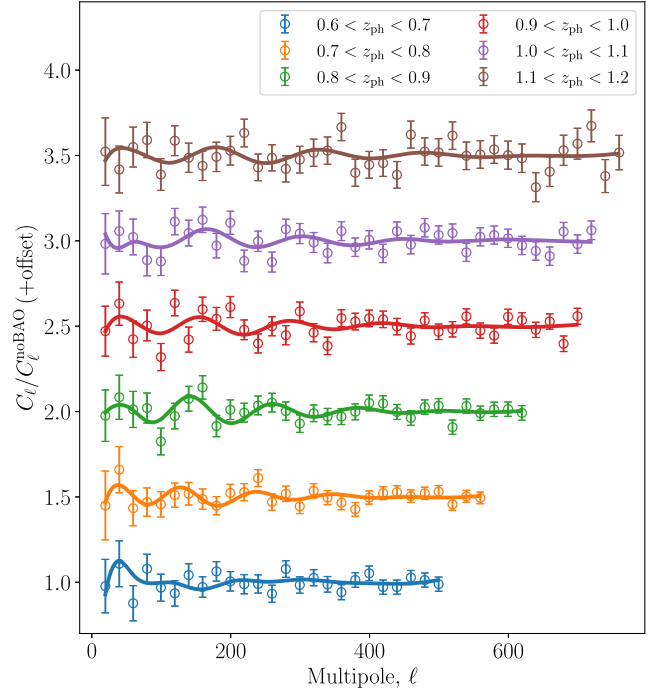
FIG. 9. The isolated BAO feature in harmonic space. Same as Figs. 8 and 10 but using the angular power spectrum (APS). Each tomographic bin has been sequentially offset vertically by $+0.5$. The BAO feature, with its constant comoving scale, expands to larger ℓ values (smaller scales) as redshift increases. The error bars are derived from the PLANCK fiducial covariance, and the solid lines represent the best fit.

equally well. In order to understand better the contribution from each tomographic bin, in Fig. 11, we show the results from fitting each bin individually. As previously noted, we do not have a detection in bin 1, but this is compatible with the results in the mock catalogs (Sec. VI). The consensus orange band representing the AVG fit from the six bins altogether tends to agree more with bins 3, 4, and 5, whereas bin 2 lies on the lower end (except for PCF), and bin 6 sits at the higher end. Overall, bearing in mind the error bars, we find an agreement between the consensus measurement (orange band, showing the combination of the six bins and the three methods) and the individual (bin and method) measurements (see more quantitative discussions in Sec. VI). We note that the preferred value by each individual bin is somewhat different from the individual bin information reported in Y3 [[76]] Fig. 8], whereas the global measurement is very consistent. Nevertheless, only about $\sim30\%$ of the galaxies in each Y6 bin were present in the same bin in Y3. Therefore, we expect substantial scatter in the clustering and best-fit BAO per individual bin, where the signal is not so strong. The fainter symbols of Fig. 11

show the results when not applying the weights that account for observational systematics, and we find negligible impact in all redshift bins and for all three estimators.

C. Robustness tests

In this subsection, we evaluate how our main results vary when we change assumptions or choices made during our analysis. The variations considered are shown in Table VIII, where the main D_M/r_d constraints are at the top with the total error included. The rest of the constraints are given in terms of $\alpha = (D_M/r_d)/(D_M/r_d)_{\text{Planck}}$, reporting their best fit values and statistical errors. We first show it for our main result (AVG or "$w(\theta) + C_\ell + \xi_p$") and report below the systematic error contribution from the redshift calibration (Sec. V A) and from the modeling (Sec. V C). The α values presented in this table with their statistical errors are also shown in Fig. 12. We note again that all these tests were studied first blinded and unblinded *a posteriori*.

The remainder of the table reports variations from the individual estimators considering only statistical errors. We split this into three parts, one per method: ACF or $w(\theta)$, APS or C_ℓ, and PCF or ξ_p. We start by reporting the individual fiducial measurement for each of those methods (in **bold**). First, we remark on the good agreement between
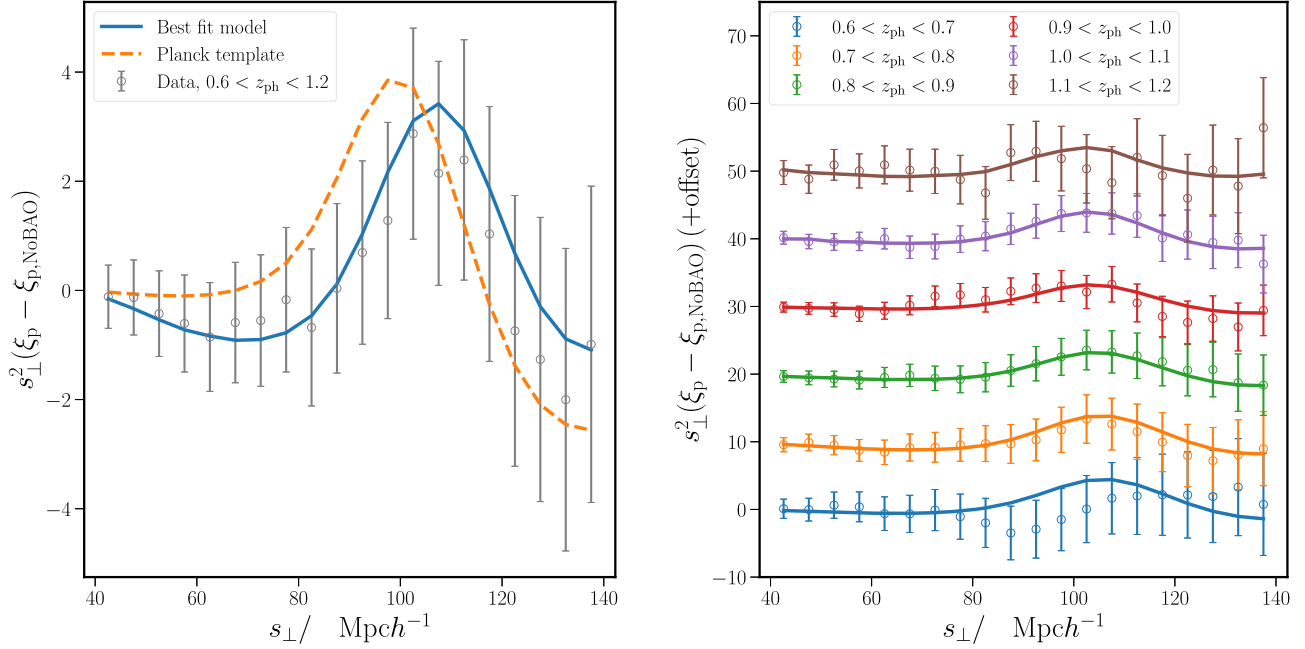
FIG. 10.   The BAO feature measured using the projected correlation function (PCF) in configuration space. The markers are the data measurements, and their error bars are derived from the fiducial PLANCK covariance. The solid lines show the best fit model. Left: the PCF clustering is measured in a single bin ($N_z = 1$) in order to concentrate all the BAO signal, for visualization purposes. Note that this is not the fiducial setup for the analysis. In addition to the best fit (solid, blue), the original PLANCK template (dashed, orange) is also overplotted. Right: the PCF measured in $N_z = 6$ bins used for the fiducial analysis. Each tomographic bin has been sequentially offset vertically by +10. Unlike the angular statistics, the BAO feature in ξ_p does not change with redshift.
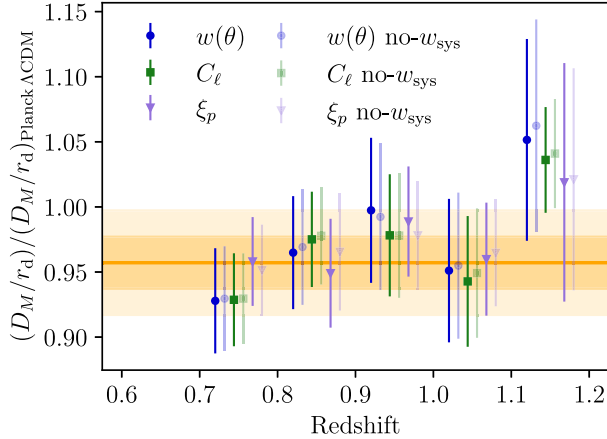

FIG. 11.   Constraints on D_M/r_d from BAO measurements of individual tomographic bins by ACF, APS, and PCF, in blue circles, green squares, and purple triangles, respectively. The D_M/r_d values are normalized by the prediction from PLANCK, assuming ΛCDM. The orange bands depict the 1 and $2-\sigma$ regions from the consensus measurement (AVG, fitting six z_{ph}-bins simultaneously). We remind the reader that we do not find a detection on the first bin (lowest z bin), and this is attributed to sample variance (see Table VI). The vivid symbols show the measurements accounting for observational systematics (by default in our analysis), whereas the faded symbols show the measurements without those corrections.

the three methods, with the largest α value preferred by C_ℓ. This tendency is somewhat different from what we find in the mocks, where the pairing between ACF and APS is more common, and the PCF tends to be lower. However, we already checked in Sec. VI that these results are statistically compatible with the mocks. The combination AVG indeed represents a good consensus measurement, being closer to ACF and PCF than to APS.

The first robustness test consists in removing the systematic weights (no-w_{sys}), where we see this has a very small effect (0.09σ, 0.02σ, and 0.16σ for ACF, APS, PCF, respectively). This highlights again the robustness of BAO against observational systematics. We then look at changing the $n(z)$ assumed in the template to that calibrated from DNF z_{nn} and VIPERS (see discussion in Sec. II E), finding differences below 0.2σ. We note that these differences are similar to those found in Sec. V A and are also accounted for by the systematic error.

We also test changes in some analysis choices such as assuming a MICE template (in this case, we multiply the resulting α by 0.9616 so that we can do a direct comparison with the rest of α values reported) or changing the scale cuts or binning. For the PCF, we also include a test changing the number of redshift bins N_z in which we split the sample, which is six for the fiducial case.

All these tests were performed while blinded. At that stage, we paid more attention to the cases in which the shift

TABLE VIII. Main results and robustness tests, discussed in detail in Sec. VII and also represented in Fig. 12. *Italic* fonts are used for tests that are found to imprint substantial deviation in either the central value or the uncertainty and are further discussed in the text. Overall, our measurement is very robust.

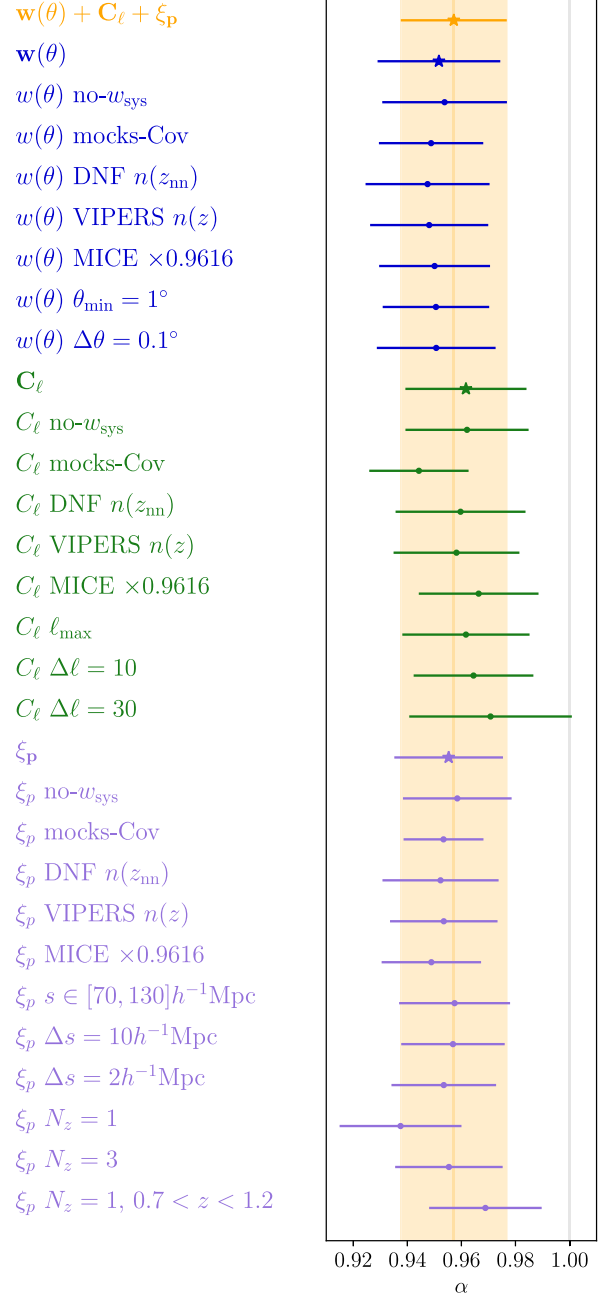| Y6 measurement	D_M/r_d
$z_{\text{eff}} = 0.85$	19.51 ± 0.41
Case	α
$\boldsymbol{w(\theta) + C_\ell + \xi_p}$ [Fid.]	0.9571 ± 0.0196
Redshift sys. err.	± 0.0035
Modelling sys. err.	± 0.0023
$\boldsymbol{w(\theta)}$	0.9517 ± 0.0227
$w(\theta)$ no-w_{sys}	0.9538 ± 0.0231
$w(\theta)$ DNF $n(z_{\text{nn}})$	0.9475 ± 0.0230
$w(\theta)$ VIPERS $n(z)$	0.9481 ± 0.0219
$w(\theta)$ MICE $\times 0.9616$	0.9501 ± 0.0197
$w(\theta)$ $\theta_{\text{min}} = 1°$	0.9506 ± 0.0226
$w(\theta)$ $\Delta\theta = 0.1°$	0.9507 ± 0.0220
$\boldsymbol{C_\ell}$	0.9617 ± 0.0224
C_ℓ no-w_{sys}	0.9621 ± 0.0228
C_ℓ DNF $n(z_{\text{nn}})$	0.9597 ± 0.0239
C_ℓ VIPERS $n(z)$	0.9582 ± 0.0232
C_ℓ MICE $\times 0.9616$	0.9664 ± 0.0220
C_ℓ $\ell_{\text{max}} = 500$	0.9617 ± 0.0235
C_ℓ $\Delta\ell = 10$	0.9645 ± 0.0221
C_ℓ $\Delta\ell = 30$	*0.9708 ± 0.0300*
$\boldsymbol{\xi_p}$	0.9553 ± 0.0201
ξ_p no-w_{sys}	0.9585 ± 0.0201
ξ_p DNF $n(z_{\text{nn}})$	0.9523 ± 0.0215
ξ_p VIPERS $n(z)$	0.9535 ± 0.0199
ξ_p MICE $\times 0.9616$	*0.9489 ± 0.0184*
ξ_p $s \in [70, 130]h^{-1}$ Mpc	0.9575 ± 0.0205
ξ_p $\Delta s_\perp = 10h^{-1}$ Mpc	0.9569 ± 0.0191
ξ_p $\Delta s_\perp = 2h^{-1}$ Mpc	0.9535 ± 0.0193
ξ_p $N_z = 3$	0.9554 ± 0.0199
ξ_p $N_z = 1$	*0.9375 ± 0.0225*
ξ_p $N_z = 1, 0.7 < z < 1.2$	*0.9689 ± 0.0203*

FIG. 12. Main BAO measurement shown with an orange star and a shaded area together with several variations of the analysis. Variations of the ACF, APS, and PCF analyses are presented in blue, green, and purple, respectively. These results are also shown in Table VIII and discussed in Sec. VII C.

in α was larger than $\Delta\alpha = 0.06$, which is approximately $1/3$ of the forecasted error. The corresponding results are marked in *italic* in Table VIII and discussed in the following:

(i) APS $\Delta\ell = 30$. 14.8% of the mocks present such an extreme change in α. We also understand that increasing the binning of ℓ can lead to an increment in the errors and a possible shift in the mean value since the wider binning makes it more challenging to resolve the wiggles.

(ii) PCF MICE. We find a shift of $\alpha_{\text{fid}} - \alpha_{\text{MICE}} \times 0.9616 = 0.0064$ (raw $\Delta\alpha = 0.0332$), but 16% of the mocks have an equivalent or larger negative shift. We also note that this shift is just below the $\sigma/3$ limit.

(iii) PCF $N_z = 1$. Although only 3.5% of the mocks present such a big negative shift between $N_z = 6$

and $N_z = 1$, this fraction rises to 10% if we consider changes in absolute value and to 12% if we only consider those mocks with one nondetection.

To understand the origin of this difference, we look at the results from individually fitting each redshift bin (Fig. 11). We identify the particularities of bin 6, which prefers a high value of α, and of bin 1, which does not have a detection but whose

likelihood peaks at low α. We already argued in [74] that combining data at the clustering statistic level [i.e., a single $\xi_p(s_\perp)$ measurement, $N_z = 1$], can give unstable results when the preferred value of α varies significantly from bin to bin.

Hence, we checked the results for $N_z = 1$ when removing bin 1, bin 6, and both. We see that, in these cases, α moves to 1.0178 ± 0.0203 (bins 2–6, last entry in Table VIII and Fig. 12), 0.9984 ± 0.00226 (bins 1–5), and 0.09983 ± 0.0226 (bins 2-5), respectively. Thus, we conclude that the results for $N_z = 1$ are unstable and less reliable than the fiducial analysis (based on $N_z = 6$), for which we already studied in Sec. VI the stability of the results.

Regarding the errors, we investigate the cases in which the error changes by more than 0.003, which is approximately 15% of our fiducial uncertainty. Such a difference only happens for APS $\Delta\ell = 30$. We again checked that it is compatible with the shifts in the mocks.

Additionally, we confirmed that, when assuming the mock covariance, the results do not change in a qualitatively big way. We find some differences in the best fit and error, but these changes are compatible with what we see in the mocks. Since we do not trust the covariance from the mocks due to the spurious correlations discussed in Sec. III, we do not include this test in Table VIII, but it is shown in Fig. 12 to understand that the changes are not dramatically different.

When assuming the MICE cosmology for the template, the results shown in Table VIII can be combined (AVG) to $\alpha \times 0.9616 = 0.9529 \pm 0.0184$ [stat.], which translates to $D_M/r_s = 19.43 \pm 0.38$ [stat.]. This shows that, even though the α value depends on the assumed cosmology, the recovered physical constraints remain practically unchanged (in this case within 0.2σ).

Finally, we report the results when considering only the first five bins ($0.6 < z_{ph} < 1.1$), as discussed in Sec. VI and Appendix C, and we discussed the possibility of removing bin 6 as this seemed to reduce the uncertainty. We concluded that it would not be removed for our fiducial analysis, but that it would also be reported. When considering only the first five bins, ($0.6 < z_{ph} < 1.1$) In this case, we obtain $\alpha_{\rm ACF} = 0.9441 \pm 0.0220$, $\alpha_{\rm APS} = 0.9478 \pm 0.0206$ and $\alpha_{\rm PCF} = 0.9521 \pm 0.0203$, leading to $\alpha_{\rm AVG} = 0.9519 \pm 0.0195$ [stat.] and

$$(D_M(z = 0.85)/r_d)_{z_{ph}<1.1} = 19.41 \pm 0.40 [\text{stat}], \quad (36)$$

which is compatible with our fiducial result, $D_M(z=0.85)/r_d = 19.51 \pm 0.41$.

With all the tests performed in this section, we conclude that our fiducial result is robust and that it represents well the consensus of the different variations in the analysis and data calibration.

VIII. CONCLUSIONS

A. Summary

We have measured the BAO angular position using galaxy clustering from the final data (Year 6 or Y6) of the Dark Energy Survey with a significance of 3.5σ. This measurement translates to a constraint on the ratio of the angular diameter distance to the acoustic scale of $D_M(z_{\rm eff})/r_d = 19.51 \pm 0.41$ at an effective redshift of $z_{\rm eff} \sim 0.85$. When comparing to the prediction from PLANCK ΛCDM cosmology ($D_M(z=0.85)/r_d = 20.39$[9]), we obtain $\alpha = (D_M/r_d)/(D_M/r_d)_{\rm Planck} = 0.957 \pm 0.020$.

The DES Y6 BAO measurement

(i) Represents a 2.1% precision measurement and it is 2.1σ below PLANCK's prediction.

(ii) Is the tightest BAO measurement from a photometric survey.

(iii) Is the most precise angular BAO measurement at $z_{\rm eff} > 0.75$ from any survey to date.

(iv) Represents a competitive constraint on D_M/r_s even when compared with current results from spectroscopic surveys with BAO as their main science driver. This is clearly well depicted by Fig. 6, which represents the state-of-the-art for angular BAO distance ladder and its snapshot at the closure of the stage-III dark energy experiments. The second tightest angular BAO constraint at similar redshift comes from eBOSS ELG [71,89] with $\alpha = 0.962 \pm 0.049$ at $z_{\rm eff} = 0.85$, in agreement in central value but with a $\sim \times 2.5$ larger uncertainty.

(v) Agrees with previous DES analyses, improving the uncertainties by $\sim 25\%$ with respect to Y3 [76] and by a factor of 2 compared to Y1 [75]. A comparison between Y6 and Y3 data and analysis is detailed in Appendix B.

For this work, we made use of the final dataset from DES, consisting of six years (Y6) of observations of the southern galactic sky over $\sim 5,000$ deg^2 in the optical bands g, r, i, z, and Y. From that data, we have constructed a galaxy sample optimized for BAO science: the Y6 BAO sample, described in our companion paper, [50]. To select this sample, we impose a color selection targeting red galaxies at $z > 0.6$ [Eq. (1)] and a redshift-dependent magnitude cut [Eq. (4)] that is tuned to maximize the BAO precision based on Fisher forecasts. This sample is then corrected from observational systematics using the iterative systematic decontamination (ISD) method [8].

We split the sample in six tomographic redshift bins (using the z_{ph} estimates from DNF), and we calibrate the redshift distributions ($n(z)$) using three independent methods. These include the directional neighboring fitting (DNF) machine learning photo-z code [91], clustering redshifts by angular cross-correlating our sample with

---

[9] We do not report the uncertainty associated to PLANCK ΛCDM as it is much smaller than the uncertainties obtained by BAO. This is a standard practice in BAO analyses.

spectroscopic surveys (WZ, following the method from [99]), and direct calibration with the VIPERS survey [137], which is complete for our sample and overlaps in 16 deg^2. By studying the impact of the different redshift calibrations on the BAO analysis in Sec. V A, we estimate a systematic error on α of $\sigma_{z,\mathrm{sys}} = 0.0035$.

We use a template-fitting method to constrain the BAO position using three different clustering estimators: the angular correlation function [ACF, $w(\theta)$], the angular power spectrum (APS, C_ℓ), and the projected correlation function (PCF, ξ_p). We then combine the three BAO measurements into our consensus (AVG) constraints by taking into account their correlation. In Secs. V B and V C, the model is optimized and validated against 1952 ICE-COLA mock catalogs described in Sec. III and following the method from [63]. As a result of this validation, we estimate a systematic error from modeling of $\sigma_{\mathrm{th,sys}} = 0.0023$.

After validating the method, we run a large set of robustness tests on the data while keeping the results blinded (Sec. VI and Table VIII). Eventually, the results were unveiled, obtaining $\alpha_{\mathrm{ACF}} = 0.952 \pm 0.023$, $\alpha_{\mathrm{APS}} = 0.963 \pm 0.022$, and $\alpha_{\mathrm{PCF}} = 0.955 \pm 0.020$ for each of the three estimators, finding them very consistent with each other. The consensus result is $\alpha_{\mathrm{AVG}} = 0.957 \pm 0.020$, which translates to $D_M(z = 0.85)/r_d = 19.51 \pm 0.41$, already including systematic error contributions. We find these results robust to removing parts of the data (individual redshift bins, high-z data, and low-z data) and variations in scale cuts, analysis choices, redshift calibration, and treatment of observational systematics.

All the cosmological information obtained in this work is contained in the reported data point, $D_M(z = 0.85)/r_d = 19.51 \pm 0.41$ or, more precisely, in the consensus likelihood that will be released in CosmoSIS[10] once the paper is accepted. A study of the consequences of this measurement on different cosmological parameters and models will follow up in a separate paper.

B. Outlook

This work does not only report a measurement on the angular BAO position that is among the most precise measurements at *high* redshift but also shows the success of the Dark Energy Survey Collaboration to use galaxy clustering (GC) from photometric surveys as a robust and competitive probe. Some of the techniques and ideas developed and lessons learned within the DES BAO project were or have the potential to be transferred to other GC analyses and vice versa. For example, the construction of an optimal sample based on forecasts was done first for BAO [49] and served as an inspiration to later create the MagLim sample [138] for the combination of GC and WL in the so-called 3 × 2pt analysis [11,100]. The use of APS (C_ℓ) in DES was first developed for the BAO analysis [67] and is now being applied for the combination of GC with

WL (3 × 2pt) [139–142]. Other ideas, such as the PCF method, constructing the order of 2000 realistic simulations to better understand the significance of features in the data, and how to combine different statistics, could potentially also be extrapolated to 3 × 2pt analyses.

Certainly, some of the lessons learnt from the DES BAO analyses can also be transferred to other surveys, including spectroscopic ones. In particular, DES has clearly pioneered with regard to the blinding policies for BAO, with this work likely being the analysis with the most stringent blinding criteria to this date. For upcoming photometric surveys such as Vera Rubin's LSST [143] or Euclid [48], the transfer of the techniques used here is more immediate, as they will need to deal with similar challenges (e.g., the calibration of the redshift distribution and how it affects the inferred cosmology).

With increasingly precise and accurate galaxy clustering measurements from photometric surveys, one can envision other ways to extract cosmological information. One example is the study of primordial Non-Gaussianities, a probe forecasted to beat CMB and spectroscopic constraints [144] if different sources of systematic errors are kept under control. Preparations from DES in this direction are presented in [145].

The other main promising avenue for photometric galaxy clustering is the combination with other probes in order to break parameter degeneracies, check consistency across probes, and mitigate the impact of systematics. In this direction, DES is preparing its final flagship 3 × 2pt analysis combining three two-point functions: galaxy position autocorrelation, cosmic shear autocorrelation, and the cross-correlation between galaxy positions and shear. DES is also prepared to combine galaxy clustering with many probes, including CMB(-lensing) and galaxy cluster number counts. Additionally, the completed DES supernovae (SN) cosmology results were recently released [16], constraining the expansion history of the Universe in a complementary way to the BAO. In a follow-up work, we will study implications of the combined constraints on the expansion history (DES BAO + SN) for cosmological parameters sensitive to it, such us those characterizing dark energy (e.g., Ω_Λ, w), curvature (Ω_k) or the current rate of expansion of the Universe (H_0). Once all other probes finalize their analysis, DES will combine them together, completing its mission of pioneering the field of multi-probe cosmology.

The main product of this work is the likelihood of the angular BAO scale, $D_A(z_{\mathrm{eff}} = 0.85)/r_s$, which will be released soon in Cosmosis.[10] Other products will be released soon at the usual DES data release website.[11] These will include the BAO sample (RA, DEC, z_{ph}, z_{nn}, and systematic weights) with its associated healpix mask and random catalog, the different redshift distributions and the ICE-COLA mocks.

All authors contributed to this paper and/or carried out infrastructure work that made this analysis possible. Some highlighted contributions from the authors of this paper include: *Scientific management and coordination*: S. A. and A. P. (Large-Scale Structure working group conveners). *Significant contributions to project development, including paper writing and figures*: S. A., H. C., K. C. C., J. M.-F., A. P., M. R.-M., and E. S. *Data analysis and methods validation*: H. C., K. C. C., and J. M.-F. *Fitting and running simulations*: I. F. *Redshift characterisation*: R. C., G. G., J. D. V., J. M.-F., and L. T. S. C. *Correction for observational systematics*: J. E.-P., S. L., M. R.-M., I. S.-N., and N. W. *Internal reviewing of the paper*: T. M. D., W. J. P., and A. J. R. *Advising*: M. C. and C. S. *Construction and validation of the DES Gold catalog*: M. A., K. B., A. C. R., T. D., A. D.-W., R. A. G., W. G. H., A. P., E. S. R., I. S.-N., E. S., and B. Y. The remaining authors have made contributions to this paper that include, but are not limited to, the construction of DECam and other aspects of collecting the data; data processing and calibration; developing broadly used methods, codes, and simulations; running the pipelines and validation tests; and promoting the science analysis.

APPENDIX A: UNBLINDING CHECKLIST

The checklist to unblind the results goes in the following order:

(1) Finalize the sample, mask, and systematic weights. Also, finalize the decision of fiducial and alternative redshift distributions. These are presented in Sec. II.
(2) Finish the validation of the analysis pipeline. Check the robustness of the redshift calibration and of the modeling against the mock catalogs. This validation leads to an estimation of the systematic errors (see Sec. V).
(3) Perform the pre-unblinding tests described in Secs. VI A and VI B, following the order described there.
(4) Circulate an advanced draft of this paper with all the previous tests carefully explained to the DES collaboration and request feedback and unblinding approval from the internal reviewers.
(5) Use the blinded data (with a coherent random shift on α and a factor applied to the errors, as described

in Sec. VI) to fill up the robustness tests shown in Table VIII and Fig. 12 with the different obtained α. We discuss these tests in Sec. VII C.

(6) Check and compare the blinded measurements of α in individual bins to our fiducial measurement (with all six bins together). The unblinded version of this figure is Fig. 11.

(7) Unblind the errors σ_α. At this advanced stage, this allowed us to check whether the errors met our expectations and to understand better the significance of the relative changes in α we saw when performing the robustness tests. For example, we found that in general, our errors are larger than the mean error from the mocks. However, (for ACF), we checked that 12% of the mocks have an error larger than what we measure on the data. This rises to 26% if we only look at the mocks with a nondetection on bin 1.

(8) Last, present a new draft of this and the companion paper [50] to the collaboration.[12] We also show our results in a video conference and, provided no further tests are required, we proceed to unblind.

This stage-by-stage unblinding aims to test our analysis and data without knowing the implications for cosmology. For that reason, we start with the parts that are further away from this information and eventually get closer and closer to the measurement of α once we take the corresponding decisions based on the previous step. At the final unbinding phase (last point above), we hope all the tests we would like to run on the data are already run. Nevertheless, we would allow further investigation if new tests are considered necessary once the data is unblinded. The guiding philosophy for the decision-making in that case would be similar to the one presented in Sec. VI. For example, one case discussed before unblinding the errors was the possibility of AVG showing a larger error than one of the individual estimators (ACF, APS, or PCF) or the combination of two of them. We did not find an easy implementation of these tests prior to unblinding them, so we decided that this would be tested once the errors were unblinded. If we were to find that possibility, we would then use the statistics from the mocks, similarly to what we did in Appendices C and D for the cases of the z bin that enlarges the error and a single z bin with no detection. We would thus complete a table with the mocks that have that property (e.g., AVG having a larger error than ACF) and check for this case which error estimation is better behaved (compared to the scatter σ_{68} or σ_{std}) and if the bias ($\langle \alpha \rangle - 1$) is worse for one of the two options.

At the point of unblinding, the paper draft was nearly final from Secs. II to VI and parts of Sec. VII (results) were completed with blinded data/figures. The discussion of robustness tests (Sec. VII C) was also completed.

APPENDIX B: COMPARISON WITH PREVIOUS DES BAO ANALYSES

We have reduced the uncertainty by $\sim$25% with respect to our previous analysis based on the first three years of observations (Y3) [76] and by a factor of 2 with respect to the results from the first year (Y1) [75]. Here, we summarize some key differences:

(i) The most obvious change is that we include the data from the completed survey (six years), approximately doubling the cumulative exposure time with respect to Y1 and Y3, impacting mostly the maximum depth in our galaxy sample. In Y6, the depth in the r, i, and z bands increase by 0.7, 0.6, 0.5 magnitudes, respectively. The improvement in depth resulted in more precise measurement of band fluxes and, hence, better estimates of redshifts. The Y6 data also has a more uniform depth coverage, and so observational systematics affecting galaxy counts across the sky are less pronounced. On the footprint, the area considered for each analysis is $1,336 \deg^2$, $4,108.47 \deg^2$, and $4,273.42 \deg^2$ for the Y1, Y3, and Y6 samples, respectively.[13]

(ii) While in Y3, we used the sample selection criteria optimized in Y1, in Y6, we have reoptimized the selection in the i band using a Fisher forecast. This results in a sample containing nearly twice the number of galaxies: 15,937,556 galaxies in the Y6 sample vs 7,031,993 in the Y3 one. Given the increased depth, we also pushed the sample to a higher redshift, $z_{ph} = 1.2$, compared to $z_{ph} = 1.1$ in Y3 and $z_{ph} = 1.0$ in Y1.

(iii) On the mitigation of observational systematics, we have required a more restrictive threshold ($T_{1D} = 2$, see Sec. II D for details) on the correlation between survey property maps and our galaxy density maps. We have also imposed the masking of outliers using two additional maps that trace artefacts and galactic cirrus in the footprint (see Sec. II C). In addition, we have accounted for residual additive stellar contamination, although we argue its impact in the BAO analysis would be negligible (see Sec. IV B 5).

(iv) In Y6, on top of the DNF redshift characterisation (used in Y1 and Y3) and the validation with VIPERS (also used in Y3), we have incorporated a further validation with clustering redshifts Sec. II E. Unlike in our previous analyses, in Y6,

---

we have propagated the impact from different $n(z)$ calibrations down to the BAO shift parameter α, being able to quantify the systematic contribution from Sec. V A.

(v) For the first time in DES, we report our main results from the statistical combination (AVG) of three clustering estimators: ACF, APS, and PCF. In Y1, the main BAO results were reported only from the ACF method, although results from APS and PCF were shown, they were not considered sufficiently matured or robust at that stage. The Y3 main BAO results were reported by taking the log-mean likelihood of ACF and APS, whereas the PCF method was improved and reported results using Y3 data at a later stage [73,74].

(vi) Although the pre-unblinding tests of Y6 are mostly based on those defined in Y3, we have extended some of these tests by having blinded versions of Figs. 4, 11, and 12 (see also the discussion in Sec. VI and Appendix A).

(vii) When comparing the results, Y1, Y3, and Y6 are compatible. The results from Y3 and Y6 are both below PLANCK's prediction by just over 2σ, having slightly different best fit values and, the latter, with a 25% tighter error.

APPENDIX C: ERROR REDUCTION UPON REMOVAL OF ONE BIN

Here, we investigate the scenario when removing one tomographic bin reduces the estimated error σ_α. In this case, we want to find out what is the best course of action to take. Potentially, we picture two solutions: taking the error and best fit from the full dataset (the six bins) or the reduced dataset with one bin eliminated (five bins).

In Table IX, we select the mocks for which $(\sigma - \sigma_{\text{All Bins}})/\sigma_{\text{All Bins}} < 0$ when removing one redshift bin. For these mocks, we perform the ACF fit with and without the bin causing $\Delta\sigma < 0$ and compare the different summary statistics. We find that even though the estimated error $\langle\sigma_\sigma\rangle$ reduces when removing those bins, the actual scatter of the best fit (σ_{68} or σ_{std}) increases. Hence, we conclude that this reduction is due to an underestimation of the error on the five-bin cases, not to an actual gain in information and that we should use the results from the combined six-bins (All). We also see in the last column that, for each of the six bins, typically $\sim 10\%$ of the mocks have a $\Delta\sigma < 0$.

If we try to pin down the cases that are more similar to our result on the data ACF (Table II), we can select the mocks for which $100(\sigma - \sigma_{\text{All Bins}})/\sigma_{\text{All Bins}} \leq -3$. This is the case shown in Table X, where we find the exact same effect as in the previous paragraph, but now with augmented differences.

TABLE IX. $\Delta\sigma < 0$ test. We select the ICE-COLA mocks for which the error on the ACF α decreases when we remove one redshift bin $[(\sigma - \sigma_{\text{All Bins}})/\sigma_{\text{All Bins}} < 0]$. This table has six sections, one corresponding to each of the 6 redshift bins meeting the condition above. Each section contains two entries: one where we have removed the bin with $(\sigma - \sigma_{\text{All Bins}})/\sigma_{\text{All Bins}} < 0$ and one where we consider all the dataset. See Table II for the definition of the summary statistics. In the last column, we report the fraction of mocks selected in each case over the entire 1952 mocks.

Bins	$\langle\alpha\rangle$	σ_{std}	σ_{68}	$\langle\sigma_\alpha\rangle$	Fraction of cases (%)
23456	1.0048	0.0237	0.0236	0.0203	12.35
All	1.0058	0.0217	0.0211	0.0210	12.35
13456	1.0045	0.0277	0.0252	0.0209	9.12
All	1.0050	0.0237	0.0239	0.0216	9.12
12456	1.0047	0.0283	0.0267	0.0205	9.68
All	1.0059	0.0235	0.0237	0.0212	9.68
12356	1.0011	0.0238	0.0253	0.0205	8.91
All	1.0041	0.0230	0.0240	0.0213	8.91
12346	1.0020	0.0254	0.0254	0.0206	9.53
All	1.0034	0.0234	0.0229	0.0211	9.53
12345	1.0057	0.0228	0.0237	0.0197	10.04
All	1.0060	0.0219	0.0211	0.0200	10.04

TABLE X. Same as Table IX except for $\Delta\sigma < -0.03$ test.

Bins	$\langle\alpha\rangle$	σ_{std}	σ_{68}	$\langle\sigma_\alpha\rangle$	Fraction of cases (%)
23456	1.0050	0.0248	0.0244	0.0218	4.30
All	1.0046	0.0220	0.0185	0.0233	4.30
13456	1.0004	0.0314	0.0297	0.0225	2.82
All	1.0033	0.0264	0.0244	0.0242	2.82
12456	1.0057	0.0320	0.0280	0.0215	3.84
All	1.0061	0.0260	0.0243	0.0230	3.84
12356	0.9946	0.0229	0.0249	0.0217	3.89
All	0.9983	0.0233	0.0242	0.0232	3.89
12346	0.9986	0.0312	0.0299	0.0230	2.31
All	1.0007	0.0259	0.0224	0.0246	2.31
12345	1.0037	0.0315	0.0312	0.0238	0.77
All	1.0040	0.0267	0.0272	0.0252	0.77

APPENDIX D: NONDETECTIONS: INCLUDING THEM IN THE FIT

A case that requires our attention is when one of the bins does not show a detection. In this case, we wonder if it is better to estimate α and its error from the whole dataset (6 bins) or to eliminate the nondetection bin (five bins).

The results are presented in Table XI for ACF, where we compare the summary statistics of the best fits for the results without the nondetection bin (e.g. "23456") and with it ("All"). In this case, the results for the comparison of the estimated error ($\langle\sigma_\alpha\rangle$) and the scatter measures (σ_{68} or

TABLE XI. Nondetection test. We select the ICE-COLA mocks for which there is a nondetection in bins 1 to 6 and analyze them in the six sections of this table. Each section contains two entries: one where we have removed the bin with nondetection and one where we consider all the dataset. See Table II for the definition of the summary statistics. in the last column, we report the fraction of mocks selected in each case over the entire 1952 mocks.

Bins	$\langle\alpha\rangle$	σ_{std}	σ_{68}	$\langle\sigma_\alpha\rangle$	Fraction of cases (%)
23456	1.0084	0.0213	0.0196	0.0208	9.63
All	1.0078	0.0222	0.0222	0.0207	9.63
13456	1.0054	0.0229	0.0222	0.0217	4.97
All	1.0053	0.0230	0.0233	0.0217	4.97
12456	1.0062	0.0258	0.0277	0.0217	2.61
All	1.0060	0.0245	0.0259	0.0216	2.61
12356	1.0085	0.0248	0.0236	0.0225	2.41
All	1.0092	0.0232	0.0232	0.0221	2.41
12346	1.0031	0.0241	0.0245	0.0221	3.33
All	1.0044	0.0242	0.0248	0.0220	3.33
12345	1.0040	0.0202	0.0196	0.0202	8.76
All	1.0064	0.0206	0.0206	0.0201	8.76

σ_{std}) are somewhat heterogeneous, and it is hard to draw strong conclusions. Regarding the mean $\langle\alpha\rangle$ for the 23456 case, we seem to find a larger bias ($\langle\alpha\rangle - 1$) than when considering the whole dataset, although this situation changes when the bin under consideration is another one. In the absence of strong preference shown by this test, we move forward with our standard analysis, which includes the six bins altogether.

APPENDIX E: ADDITIONAL TABLES FOR PRE-UNBLINDING TESTS ON DATA

This appendix includes the tables used for the set of pre-unblinding tests performed to assess the robustness of our measurements, discussed in Sec. VI. These sets of tests are summarized in Tables XII–XIV for ACF, APS and PCF, respectively. We test how much the best fit α changes ($\Delta\alpha$, in %) when we modify some choice in the analysis and compare it with the mocks. For each test, we print the minimum and maximum value $\Delta\alpha$ that contains 90%, 95%, 97%, and 99% of the mocks, with an equal number of mocks left outside each of the two extremes. We analyze the mocks with the *mocklike* setup, and the data by default

TABLE XII. Table of pre-unblinding tests for the angular correlation function from Sec. VI, showing the impact of removing individual/several tomographic bins, changing the assumed cosmology for the BAO template, changing the covariance and considering a different estimate of the true redshift distributions. We report variations in α with respect to our fiducial analysis, to keep results blind. The middle four (double) columns show the range of $\Delta\alpha$ values measured on the ICE-COLA mocks that enclose the fraction of mocks shown at the top of each column. The mocks are analysed with the mocklike setup [MICE cosmology, $\sim n(z_{\mathrm{nn}})$, b_{mocks}]. The last column shows the $\Delta\alpha$ value measured on the data, by default for the mocklike setup [PLANCK, $n(z_{\mathrm{fid}})$, $b_{\mathrm{pl,data}}$, main results], but for some tests also with the data-like-mice setup [MICE, $n(z_{\mathrm{fid}})$, $b_{\mathrm{pl,data}}$, secondary results in *italics*]. We mark in **bold** the tests that fail on the data column and on the boundary that has been surpassed. The bottom rows show the impact on the error in α of removing one/several tomographic bins of the data (although we do not impose specific criteria in these tests).

Threshold (Fraction of mocks)	90% Min	90% Max	95% Min	95% Max	97% Min	97% Max	99% Min	99% Max	Data MICE	Data PLANCK
				$10^2(\alpha - \alpha_{\mathrm{fiducial}})$						
Bins 23456	−1.33	1.43	−1.79	1.86	−2.10	2.17	−2.44	2.76	*0.75*	1.15
Bins 13456	−1.39	1.63	−1.83	1.99	−2.03	2.30	−2.80	3.13	*1.03*	1.47
Bins 12456	−1.37	1.51	−1.71	2.00	−2.03	2.35	−2.52	3.23	*−0.21*	−0.39
Bins 12356	−1.45	1.27	−1.81	1.57	−2.19	1.88	−2.80	2.76	*−0.66*	−0.27
Bins 12346	−1.21	1.11	−1.51	1.41	−1.79	1.72	−2.48	2.02	*0.37*	0.30
Bins 12345	−0.86	0.76	−1.07	0.96	−1.30	1.15	−1.63	1.65	*−0.68*	−0.76
Bins 456	−2.85	3.73	−3.42	4.85	−3.86	5.54	−5.00	7.90	*3.26*	3.41
Bins 123	−3.30	2.65	−4.27	3.45	−5.04	4.26	−6.80	5.56	*−1.55*	−1.58
Bins 1234	−1.83	1.67	−2.25	2.13	−2.55	2.35	−3.67	3.22	*−0.39*	−0.70
Template Cosmo	−0.33	0.48	−0.40	0.60	−0.44	0.68	−0.55	0.89	*X*	0.17
Covariance	−0.46	0.42	−0.58	0.54	−0.68	0.64	−0.83	0.82	*X*	−0.42
$n(z)z_{\mathrm{nn}}$− fid	−0.56	0.08	−0.60	0.14	−0.64	0.20	−0.72	0.31	*X*	−0.42
				$100\,(\sigma - \sigma_{\mathrm{All\ Bins}})/\sigma_{\mathrm{All\ Bins}}$						
Bins 23456	−2.47	25.15	−4.33	30.34	−6.09	35.42	−9.08	41.50	*5.37*	3.96
Bins 13456	−1.60	26.16	−3.55	31.21	−5.18	35.18	−8.95	45.61	*18.05*	14.54
Bins 12456	−2.00	26.22	−4.53	31.44	−5.84	36.80	−8.93	45.86	*18.05*	14.98

(Table continued)

TABLE XII. *(Continued)*

Threshold (Fraction of mocks)	90% Min	90% Max	95% Min	95% Max	97% Min	97% Max	99% Min	99% Max	Data MICE	Data PLANCK
Bins 12356	−2.29	25.17	−4.09	30.79	−5.51	35.11	−9.35	41.35	*8.29*	4.41
Bins 12346	−1.39	19.89	−2.84	24.51	−4.07	27.92	−6.22	34.80	*7.32*	7.93
Bins 12345	−0.66	11.94	−1.45	14.87	**−1.97**	17.79	−3.56	22.50	*0.49*	**−3.08**
Bins 456	12.08	94.25	8.20	114.76	5.13	128.50	−1.76	166.46	*66.34*	57.71
Bins 123	10.14	80.86	5.92	95.62	3.02	109.42	−2.36	144.43	*21.95*	18.50
Bins 1234	1.37	35.50	−0.99	42.58	−1.84	45.70	−4.23	55.74	*7.80*	3.96

TABLE XIII. Table of pre-unblinding tests for the angular power spectrum (APS) from Sec. VI. See description in Table XII and text.

Threshold (Fraction of mocks)	0.9 Min	0.9 Max	0.95 Min	0.95 Max	0.97 Min	0.97 Max	0.99 Min	0.99 Max	Data MICE	Data PLANCK
				$10^2(\alpha - \alpha_{\mathrm{fiducial}})$						
Bins 23456	−1.18	1.45	−1.59	1.85	−2.01	2.12	−2.99	3.19	*0.24*	0.54
Bins 13456	−1.46	**1.55**	−1.88	2.26	−2.24	2.76	−3.54	3.60	*1.37*	**1.66**
Bins 12456	−1.32	1.48	−1.82	2.07	−2.14	2.71	−2.75	4.22	*−0.18*	−0.25
Bins 12356	−1.55	1.28	−2.05	1.79	−2.63	2.10	−4.36	3.08	*−0.20*	−0.21
Bins 12346	−1.48	1.43	−2.01	1.91	−2.67	2.49	−3.96	3.31	*1.22*	0.64
Bins 12345	−1.59	1.45	−2.10	2.00	−2.67	2.42	−3.95	3.60	*−1.52*	−1.39
Bins 456	−2.68	3.75	−3.25	4.91	−4.08	5.56	−5.96	8.06	*2.35*	3.28
Bins 123	−4.58	3.44	−6.16	4.46	−7.80	5.49	−14.48	7.00	*−1.33*	−1.82
Bins 1234	−2.78	2.47	−3.87	3.37	−4.58	4.29	−6.38	6.17	*−0.81*	−1.13
Template Cosmo	−0.59	0.62	−0.72	0.83	−0.89	0.99	−1.20	1.60	*X*	−0.49
Covariance	−0.57	0.62	−0.75	0.79	−0.91	0.91	−1.30	1.38	*X*	−0.11
$n(z)z_{\mathrm{nn}}$ − fid	−0.35	0.61	−0.47	0.69	−0.55	0.75	−0.78	0.89	*X*	−0.20
				$100\,(\sigma - \sigma_{\mathrm{All\ Bins}})/\sigma_{\mathrm{All\ Bins}}$						
Bins 23456	−5.53	28.15	−7.91	34.95	−10.77	44.11	−16.41	61.14	*−1.46*	0.69
Bins 13456	−5.06	33.65	−8.46	40.63	−11.21	47.60	−18.61	78.34	*12.64*	16.85
Bins 12456	−5.09	29.11	−8.63	37.93	−10.67	45.63	−15.98	54.38	*26.19*	23.16
Bins 12356	−6.17	33.22	−9.39	45.05	−12.03	49.74	−22.23	62.51	*8.43*	10.56
Bins 12346	−5.67	31.74	−9.73	41.92	−12.71	47.79	−19.20	73.87	*13.69*	12.18
Bins 12345	**−4.89**	30.92	−7.90	42.62	−10.77	52.16	−18.77	75.55	*−6.37*	**−7.72**
Bins 456	−0.98	97.42	−7.16	130.80	−12.08	155.71	−18.40	203.90	*46.07*	53.65
Bins 123	1.81	126.95	−3.37	160.80	−7.36	189.98	−17.54	257.44	*24.08*	16.14
Bins 1234	−3.89	70.89	−7.83	86.84	−12.27	104.47	−22.21	156.87	*7.57*	1.34

TABLE XIV. Table of pre-unblinding tests for the projected correlation function from Sec. VI. See description in Table XII and text.

Threshold (Fraction of mocks)	0.9 Min	0.9 Max	0.95 Min	0.95 Max	0.97 Min	0.97 Max	0.99 Min	0.99 Max	Data MICE	Data PLANCK
				$10^2(\alpha - \alpha_{\mathrm{fiducial}})$						
Bins 23456	−1.72	1.48	−2.12	1.92	−2.32	2.12	−2.96	2.77	*0.95*	0.95
Bins 13456	−1.48	1.32	−1.86	1.72	−2.12	1.92	−2.65	2.63	*−0.33*	−0.36
Bins 12456	−1.28	1.28	−1.64	1.70	−2.00	2.04	−2.53	2.89	*0.12*	0.33
Bins 12356	−1.16	1.16	−1.46	1.60	−1.68	1.92	−2.57	2.37	*−0.48*	−0.59
Bins 12346	−0.76	0.96	−1.00	1.20	−1.16	1.52	−1.60	2.00	*0.17*	0.24
Bins 12345	−0.44	0.52	−0.60	0.64	−0.68	0.72	−0.85	0.88	*−0.21*	−0.32
Bins 456	−3.76	3.24	−4.85	4.28	−5.40	4.88	−6.59	6.47	*2.37*	2.29
Bins 123	−1.92	2.44	−2.48	3.12	−2.96	3.52	−4.35	4.36	*−1.00*	−1.48
Bins 1234	−1.00	1.32	−1.28	1.66	−1.52	1.88	−1.94	2.48	*−0.08*	−0.16

(Table continued)

TABLE XIV. *(Continued)*

Threshold (Fraction of mocks)	0.9 Min	0.9 Max	0.95 Min	0.95 Max	0.97 Min	0.97 Max	0.99 Min	0.99 Max	Data MICE	Data PLANCK
Template Cosmo	−0.80	0.92	−1.01	1.12	−1.13	1.20	−1.49	1.49	*X*	0.33
Covariance	−0.40	0.48	−0.48	0.60	−0.56	0.68	−0.73	0.84	*X*	−0.12
$n(z)z_{nn}-$ fid	−0.40	−0.08	−0.44	−0.04	−0.44	0.00	−0.49	0.04	*X*	−0.29
$100\ (\sigma - \sigma_{\text{All Bins}})/\sigma_{\text{All Bins}}$										
Bins 23456	−1.12	32.11	−3.30	40.01	−4.62	45.33	−6.56	55.20	*4.55*	4.65
Bins 13456	−1.12	27.14	−2.80	32.06	−3.99	37.51	−6.23	47.73	*22.38*	18.27
Bins 12456	−1.97	23.91	−3.41	28.78	−4.54	33.69	−6.91	40.64	*8.39*	5.98
Bins 12356	−1.02	22.99	−2.61	27.89	−3.21	33.89	−5.85	40.96	*6.29*	7.97
Bins 12346	0.00	15.35	−1.49	18.40	−2.20	20.89	−3.80	26.56	*7.34*	9.30
Bins 12345	0.00	7.00	−1.14	8.93	−1.34	10.48	−2.12	12.19	*1.75*	1.00
Bins 456	18.11	124.49	14.14	150.21	10.89	169.93	5.18	222.60	*69.23*	50.83
Bins 123	6.09	58.36	4.35	69.50	2.92	75.66	−1.03	94.05	*21.33*	27.91
Bins 1234	8.46	19.08	0.00	26.12	−0.97	29.96	−2.36	37.06	*9.44*	10.96

with the *datalike* setup (labeled as PLANCK). For the tests that consist in removing part of the data, we also repeat them on the data assuming MICE cosmology (*data-like-mice*), but this is considered a secondary test. In the main text (Sec. VI), we only show the results for the (PLANCK) data in Figs. 4 and 5, but the quantitative decision for the fail/pass criteria comes from the tables shown in this appendix.

Specifically, we assess the impact of removing one tomographic bin at a time, removing the high- or low-redshift parts of the data, of changing the template cosmology, the covariance and the $n(z)$ estimation. For each test, we report variations in the best-fit α with respect to our fiducial analysis. For all cases except for the template cosmology, the covariance, and the $n(z)$ estimation, we also test the impact on the estimated uncertainty σ_α, which is displayed in the bottom part of each table. While we do not impose strict pre-unblinding criteria for the changes in σ_α, we regard them as informative.

[1] A. Albrecht, G. Bernstein, R. Cahn *et al.*, arXiv:astro-ph/0609591.

[2] The Dark Energy Survey Collaboration, arXiv:astro-ph/0510346.

[3] B. Flaugher, H. T. Diehl, K. Honscheid *et al.* (DES Collaboration), Astrophys. J. **150,** 150 (2015).

[4] Dark Energy Survey Collaboration, Phys. Rev. Lett. **122,** 171301 (2019).

[5] M. Gatti, E. Sheldon *et al.* (DES Collaboration), Mon. Not. R. Astron. Soc. **504,** 4312 (2021).

[6] A. Amon *et al.* (DES Collaboration), Phys. Rev. D **105,** 023514 (2022).

[7] L. F. Secco, S. Samuroff *et al.* (DES Collaboration), Phys. Rev. D **105,** 023515 (2022).

[8] M. Rodríguez-Monroy *et al.*, Mon. Not. R. Astron. Soc. **511,** 2665 (2022).

[9] A. Porredon *et al.* (DES Collaboration), Phys. Rev. D **106,** 103530 (2022).

[10] S. Pandey *et al.* (DES Collaboration), Phys. Rev. D **106,** 043520 (2022).

[11] Dark Energy Survey Collaboration, Phys. Rev. D **105,** 023520 (2022).

[12] M. Costanzi *et al.* (DES and SPT Collaborations), Phys. Rev. D **103,** 043522 (2021).

[13] C. To *et al.* (DES Collaboration), Phys. Rev. Lett. **126,** 141301 (2021).

[14] DES and SPT Collaborations, Phys. Rev. D **100,** 023541 (2019).

[15] DES and SPT Collaborations, Phys. Rev. D **107,** 023531 (2023).

[16] Dark Energy Survey Collaboration, arXiv:2401.02929.

[17] M. Vincenzi, D. Brout *et al.* (DES Collaboration), arXiv:2401.02929.

[18] Dark Energy Survey Collaboration, Mon. Not. R. Astron. Soc. **460,** 1270 (2016).

[19] Dark Energy Survey Collaboration, Astrophys. J. Suppl. Ser. **239,** 18 (2018).

[20] Dark Energy Survey Collaboration, Astrophys. J. Suppl. Ser. **255,** 20 (2021).

[21] I. Sevilla-Noarbe *et al.* (DES Collaboration), Astrophys. J. Suppl. Ser. **254,** 24 (2021).

[22] K. Bechtol *et al.* (to be published).

[23] P. J. E. Peebles and J. T. Yu, Astrophys. J. **162,** 815 (1970).

[24] R. A. Sunyaev and Y. B. Zeldovich, Astrophys. Space Sci. **7**, 3 (1970).

[25] J. R. Bond and G. Efstathiou, Astrophys. J. Lett. **285**, L45 (1984).

[26] J. R. Bond and G. Efstathiou, Mon. Not. R. Astron. Soc. **226**, 655 (1987).

[27] P. D. Mauskopf *et al.*, Astrophys. J. Lett. **536**, L59 (2000).

[28] S. Hanany *et al.*, Astrophys. J. Lett. **545**, L5 (2000).

[29] D. J. Eisenstein *et al.*, Astrophys. J. **633**, 560 (2005).

[30] W. J. Percival *et al.*, Mon. Not. R. Astron. Soc. **327**, 1297 (2001).

[31] S. Cole *et al.*, Mon. Not. R. Astron. Soc. **362**, 505 (2005).

[32] F. Beutler, C. Blake, M. Colless, D. Heath Jones, L. Staveley-Smith, L. Campbell, Q. Parker, W. Saunders, and F. Watson, Mon. Not. R. Astron. Soc. **416**, 3017 (2011).

[33] C. Blake *et al.*, Mon. Not. R. Astron. Soc. **415**, 2892 (2011).

[34] C. Blake *et al.*, Mon. Not. R. Astron. Soc. **418**, 1707 (2011).

[35] E. A. Kazin *et al.*, Mon. Not. R. Astron. Soc. **441**, 3524 (2014).

[36] S. R. Hinton *et al.*, Mon. Not. R. Astron. Soc. **464**, 4807 (2017).

[37] A. J. Ross, L. Samushia, C. Howlett, W. J. Percival, A. Burden, and M. Manera, Mon. Not. R. Astron. Soc. **449**, 835 (2015).

[38] BOSS Collaboration, Mon. Not. R. Astron. Soc. **470**, 2617 (2017).

[39] eBOSS Collaboration, Mon. Not. R. Astron. Soc. **473**, 4773 (2018).

[40] N. G. Busca *et al.*, Astron. Astrophys. **552**, A96 (2013).

[41] A. Slosar *et al.*, J. Cosmol. Astropart. Phys. 04 (2013) 026.

[42] A. Font-Ribera *et al.*, J. Cosmol. Astropart. Phys. 05 (2014) 027.

[43] T. Delubac *et al.*, Astron. Astrophys. **574**, A59 (2015).

[44] J. E. Bautista *et al.*, Astron. Astrophys. **603**, A12 (2017).

[45] H. du Mas des Bourboux *et al.*, Astrophys. J. **901**, 153 (2020).

[46] eBOSS Collaboration, Phys. Rev. D **103**, 083533 (2021).

[47] DES Collaboration, arXiv:1611.00036.

[48] R. Laureijs *et al.*, arXiv:1110.3193.

[49] M. Crocce *et al.* (DES Collaboration), Mon. Not. R. Astron. Soc. **482**, 2807 (2019).

[50] J. Mena-Fernández *et al.* (DES Collaboration), preceding paper, Phys. Rev. D **110**, 063514 (2024).

[51] B. Reid *et al.*, Mon. Not. R. Astron. Soc. **455**, 1553 (2016).

[52] K. S. Dawson *et al.*, Astrophys. J. **151**, 44 (2016).

[53] M. Crocce *et al.* (DES Collaboration), Mon. Not. R. Astron. Soc. **455**, 4301 (2016).

[54] J. Elvin-Poole *et al.* (DES Collaboration), Phys. Rev. D **98**, 042006 (2018).

[55] A. Carnero Rosell *et al.* (DES Collaboration), Mon. Not. R. Astron. Soc. **509**, 778 (2022).

[56] A. J. Ross *et al.*, Mon. Not. R. Astron. Soc. **417**, 1350 (2011).

[57] S. Ho *et al.*, Astrophys. J. **761**, 14 (2012).

[58] B. Leistedt, H. V. Peiris, D. J. Mortlock, A. Benoit-Lévy, and A. Pontzen, Mon. Not. R. Astron. Soc. **435**, 1857 (2013).

[59] N. Weaverdyck and D. Huterer, Mon. Not. R. Astron. Soc. **503**, 5061 (2021).

[60] S. Avila, S. G. Murray, A. Knebe, C. Power, A. S. G. Robotham, and J. Garcia-Bellido, Mon. Not. R. Astron. Soc. **450**, 1856 (2015).

[61] S. Avila *et al.* (DES Collaboration), Mon. Not. R. Astron. Soc. **479**, 94 (2018).

[62] A. Izard, M. Crocce, and P. Fosalba, Mon. Not. R. Astron. Soc. **459**, 2327 (2016).

[63] I. Ferrero *et al.* (DES Collaboration), Astron. Astrophys. **656**, A106 (2021).

[64] M. Manera *et al.*, Mon. Not. R. Astron. Soc. **428**, 1036 (2013).

[65] C. Zhao *et al.*, Mon. Not. R. Astron. Soc. **503**, 1149 (2021).

[66] K. C. Chan *et al.* (DES Collaboration), Mon. Not. R. Astron. Soc. **480**, 3031 (2018).

[67] H. Camacho *et al.* (DES Collaboration), Mon. Not. R. Astron. Soc. **487**, 3870 (2019).

[68] J. E. Bautista, R. Paviot, M. Vargas Magaña, S. de la Torre, S. Fromenteau, H. Gil-Marín, A. J. Ross *et al.* (eBOSS Collaboration), Mon. Not. R. Astron. Soc. **500**, 736 (2021).

[69] H. Gil-Marín *et al.*, Mon. Not. R. Astron. Soc. **498**, 2492 (2020).

[70] A. Raichoor *et al.*, Mon. Not. R. Astron. Soc. **500**, 3254 (2021).

[71] J. Hou *et al.*, Mon. Not. R. Astron. Soc. **500**, 1201 (2021).

[72] A. J. Ross *et al.*, Mon. Not. R. Astron. Soc. **464**, 1168 (2017).

[73] K. C. Chan, I. Ferrero, S. Avila, A. J. Ross, M. Crocce, and E. Gaztañaga, Mon. Not. R. Astron. Soc. **511**, 3965 (2022).

[74] K. C. Chan, S. Avila, A. Carnero Rosell, I. Ferrero, J. Elvin-Poole, E. Sanchez, H. Camacho, A. Porredon, M. Crocce *et al.* (DES Collaboration), Phys. Rev. D **106**, 123502 (2022).

[75] Dark Energy Survey Collaboration, Mon. Not. R. Astron. Soc. **483**, 4866 (2019).

[76] T. M. C. Abbott *et al.* (Dark Energy Survey Collaboration), Phys. Rev. D **105**, 043512 (2022).

[77] S. Sridhar, Y.-S. Song, A. J. Ross, R. Zhou, J. A. Newman, C.-H. Chuang, R. Blum, E. Gaztañaga, M. Landriau, and F. Prada, Astrophys. J. **904**, 69 (2020).

[78] N. Padmanabhan *et al.*, Mon. Not. R. Astron. Soc. **378**, 852 (2007).

[79] J. Estrada, E. Sefusatti, and J. A. Frieman, Astrophys. J. **692**, 265 (2009).

[80] G. Hütsi, Mon. Not. R. Astron. Soc. **401**, 2477 (2010).

[81] E. Sánchez, A. Carnero, J. García-Bellido, E. Gaztañaga, F. de Simoni, M. Crocce, A. Cabré, P. Fosalba, and D. Alonso, Mon. Not. R. Astron. Soc. **411**, 277 (2011).

[82] M. Crocce, E. Gaztañaga, A. Cabré, A. Carnero, and E. Sánchez, Mon. Not. R. Astron. Soc. **417**, 2577 (2011).

[83] H.-J. Seo *et al.*, Astrophys. J. **761**, 13 (2012).

[84] A. Carnero, E. Sánchez, M. Crocce, A. Cabré, and E. Gaztañaga, Mon. Not. R. Astron. Soc. **419**, 1689 (2012).

[85] J. E. Bautista *et al.*, Mon. Not. R. Astron. Soc. **500**, 736 (2020).

[86] H. Gil-Marín *et al.*, Mon. Not. R. Astron. Soc. **498**, 2492 (2020).

[87] A. Tamone *et al.*, Mon. Not. R. Astron. Soc. **499**, 5527 (2020).

[88] A. de Mattia *et al.*, Mon. Not. R. Astron. Soc. **501**, 5616 (2021).

[89] R. Neveux *et al.*, Mon. Not. R. Astron. Soc. **499**, 210 (2020).

[90] H. du Mas des Bourboux *et al.*, Astrophys. J. **901**, 153 (2020).

[91] J. De Vicente, E. Sánchez, and I. Sevilla-Noarbe, Mon. Not. R. Astron. Soc. **459**, 3078 (2016).

[92] L. Guzzo *et al.*, Astron. Astrophys. **566**, A108 (2014).

[93] A. M. Meisner, D. Lang, and D. J. Schlegel, Astrophys. J. **154**, 161 (2017).

[94] N. Weaverdyck, M. Rodriguez-Monroy *et al.* (DES Collaboration) (to be published).

[95] M. Rodriguez-Monroy, N. Weaverdyick *et al.* (DES Collaboration) (to be published).

[96] N. Weaverdyck and D. Huterer, Mon. Not. R. Astron. Soc. **503**, 5061 (2021).

[97] B. Reid *et al.*, Mon. Not. R. Astron. Soc. **455**, 1553 (2016).

[98] A. J. Ross *et al.*, Mon. Not. R. Astron. Soc. **498**, 2354 (2020).

[99] R. Cawthon *et al.*, Mon. Not. R. Astron. Soc. **513**, 5517 (2022).

[100] A. Porredon *et al.* (DES Collaboration), Phys. Rev. D **106**, 103530 (2022).

[101] J. Koda, C. Blake, F. Beutler, E. Kazin, and F. Marin, Mon. Not. R. Astron. Soc. **459**, 2118 (2016).

[102] P. Fosalba, M. Crocce, E. Gaztañaga, and F. J. Castander, Mon. Not. R. Astron. Soc. **448**, 2987 (2015).

[103] M. Crocce, F. J. Castander, E. Gaztañaga, P. Fosalba, and J. Carretero, Mon. Not. R. Astron. Soc. **453**, 1513 (2015).

[104] Planck Collaboration, Astron. Astrophys. **641**, A6 (2020).

[105] S. D. Landy and A. S. Szalay, Astrophys. J. **412**, 64 (1993).

[106] M. Jarvis, G. Bernstein, and B. Jain, Mon. Not. R. Astron. Soc. **352**, 338 (2004).

[107] D. Alonso, arXiv:1210.1833.

[108] E. Hivon, K. M. Górski, C. B. Netterfield, B. P. Crill, S. Prunet, and F. Hansen, Astrophys. J. **567**, 2 (2002),

[109] D. Alonso, J. Sanchez, A. Slosar (LSST Dark Energy Science Collaboration), Mon. Not. R. Astron. Soc. **484**, 4127 (2019).

[110] A. Nicola *et al.*, J. Cosmol. Astropart. Phys. 03 (2020) 044.

[111] C. García-García, J. Ruiz-Zapatero, D. Alonso, E. Bellini, P. G. Ferreira, E.-M. Mueller, A. Nicola, and P. Ruiz-Lapuente, J. Cosmol. Astropart. Phys. 10 (2021) 030.

[112] A. Krolewski, S. Ferraro, E. F. Schlafly, and M. White, J. Cosmol. Astropart. Phys. 05 (2020) 047.

[113] A. Nicola, D. Alonso, J. Sánchez, A. Slosar, H. Awan, A. Broussard, J. Dunkley, E. Gawiser, Z. Gomes, R. Mandelbaum *et al.*, J. Cosmol. Astropart. Phys. 03 (2020) 044.

[114] A. Lewis, A. Challinor, and A. Lasenby, Astrophys. J. **538**, 473 (2000).

[115] M. Crocce and R. Scoccimarro, Phys. Rev. D **77**, 023533 (2008).

[116] N. Padmanabhan and M. White, Phys. Rev. D **80**, 063508 (2009).

[117] N. Kaiser, Mon. Not. R. Astron. Soc. **227**, 1 (1987).

[118] Z. Vlah, U. Seljak, M. Yat Chu, and Y. Feng, J. Cosmol. Astropart. Phys. 03 (2016) 057.

[119] L. Senatore and M. Zaldarriaga, J. Cosmol. Astropart. Phys. 02 (2015) 013.

[120] D. Blas, M. Garny, M. M. Ivanov, and S. Sibiryakov, J. Cosmol. Astropart. Phys. 07 (2016) 028.

[121] M. M. Ivanov, M. Simonović, and M. Zaldarriaga, J. Cosmol. Astropart. Phys. 05 (2020) 042.

[122] M. M. Ivanov and S. Sibiryakov, J. Cosmol. Astropart. Phys. 07 (2018) 053.

[123] E. Krause and T. Eifler, Mon. Not. R. Astron. Soc. **470**, 2100 (2017).

[124] X. Fang, T. Eifler, and E. Krause, Mon. Not. R. Astron. Soc. **497**, 2699 (2020).

[125] X. Fang, E. Krause, T. Eifler, and N. MacCrann, J. Cosmol. Astropart. Phys. 05 (2020) 010.

[126] M. Crocce, A. Cabré, and E. Gaztañaga, Mon. Not. R. Astron. Soc. **414**, 329 (2011).

[127] M. A. Troxel, E. Krause, C. Chang, T. F. Eifler, O. Friedrich, D. Gruen, N. MacCrann *et al.*, Mon. Not. R. Astron. Soc. **479**, 4998 (2018).

[128] O. Friedrich *et al.*, Mon. Not. R. Astron. Soc. **508**, 3125 (2021).

[129] G. Efstathiou, Mon. Not. R. Astron. Soc. **349**, 603 (2004).

[130] C. García-García, D. Alonso, and E. Bellini, J. Cosmol. Astropart. Phys. 11 (2019) 043.

[131] H. S. Xavier, F. B. Abdalla, and B. Joachimi, Mon. Not. R. Astron. Soc. **459**, 3693 (2016).

[132] K. C. Chan, I. Ferrero, S. Avila, A. J. Ross, M. Crocce, and E. Gaztanaga, Mon. Not. R. Astron. Soc. **511**, 3965 (2022).

[133] P. Avery, CLEO note CBX, 95 (1996), https://www.phys.ufl.edu/~avery/fitting/error_correl.pdf.

[134] J. Erler, Eur. Phys. J. C **75**, 1 (2015).

[135] B. Wallisch, *Cosmological Probes of Light Relics* (Springer Nature, New York, 2019).

[136] T. Dumerchat and J. E. Bautista, Astron. Astrophys. **667**, A80 (2022).

[137] M. Scodeggio *et al.*, Astron. Astrophys. **609**, A84 (2018).

[138] A. Porredon *et al.* (DES Collaboration), Phys. Rev. D **103**, 043503 (2021).

[139] F. Andrade-Oliveira, H. Camacho, L. Faga *et al.* (DES Collaboration), Mon. Not. R. Astron. Soc. **505**, 5714 (2021).

[140] H. Camacho, F. Andrade-Oliveira, A. Troja *et al.* (DES Collaboration), Mon. Not. R. Astron. Soc. **516**, 5799 (2022).

[141] C. Doux, B. Jain *et al.* (DES Collaboration), Mon. Not. R. Astron. Soc. **515**, 1942 (2022).

[142] L. Faga *et al.* (DES Collaboration), arXiv:2406.12675.

[143] LSST Science Collaboration, arXiv:0912.0201.

[144] R. de Putter and O. Doré, Phys. Rev. D **95**, 123513 (2017).

[145] W. Riquelme *et al.* (DES Collaboration), Mon. Not. R. Astron. Soc. **523**, 603 (2023).